

**DEVELOPMENT OF TIME-RESOLVED
DIFFUSE OPTICAL SYSTEMS USING
SPAD DETECTORS AND AN EFFICIENT
IMAGE RECONSTRUCTION
ALGORITHM**

**DEVELOPMENT OF TIME-RESOLVED DIFFUSE
OPTICAL SYSTEMS USING SPAD DETECTORS
AND AN EFFICIENT IMAGE
RECONSTRUCTION ALGORITHM**

By

Mrwan Alayed

B.Sc. Umm Alqura University, 2006

M.S. King Abdulaziz University, 2010

A Thesis

Submitted to the School of Graduate
Studies in Partial Fulfillment of the
Requirements for the Degree of
Doctor of Philosophy

McMaster University

Hamilton, Ontario, Canada

© Copyright by Mrwan Alayed, Feb. 2019

Doctor of Philosophy (2019)
(Biomedical Engineering)

McMaster University
Hamilton, Ontario

TITLE: Development of Time-Resolved Diffuse Optical
Systems Using SPAD Detectors and an Efficient Image
Reconstruction Algorithm

AUTHOR: Mrwan Alayed,
BSc. Umm Alqura University, Makkah, Saudi Arabia
MSc. King Abdulaziz University, Jeddah, Saudi Arabia

SUPERVISOR: Prof. M. Jamal Deen

NUMBER OF PAGES: xv, 145.

Abstract

Time-Resolved diffuse optics is a powerful and safe technique to quantify the **optical properties (OP)** for highly scattering media such as biological tissues. The OP values are correlated with the compositions of the measured objects, especially for the tissue chromophores such as hemoglobin. The OP are mainly the absorption and the reduced scattering coefficients that can be quantified for highly scattering media using Time-Resolved Diffuse Optical Spectroscopy (TR-DOS) systems. The OP can be retrieved using Time-Resolved Diffuse Optical Imaging (TR-DOI) systems to reconstruct the distribution of the OP in measured media. Therefore, TR-DOS and TR-DOI can be used for functional monitoring of brain and muscles, and to diagnose some diseases such as detection and localization for breast cancer and blood clot. In general, TR-DOI systems are non-invasive, reliable, and have a high temporal resolution.

TR-DOI systems have been known for their complexity, bulkiness, and costly equipment such as light sources (picosecond pulsed laser) and detectors (single photon counters). Also, TR-DOI systems acquire a large amount of data and suffer from the computational cost of the image reconstruction process. These limitations hinder the usage of TR-DOI for widespread potential applications such as clinical measurements.

The goals of this research project are to investigate approaches to eliminate two main limitations of TR-DOI systems. First, building TR-DOS systems using custom-designed **free-running (FR)** and **time-gated (TG)** SPAD detectors that are fabricated in low-cost standard CMOS technology instead of the costly photon counting and timing detectors. The FR-TR-DOS prototype has demonstrated comparable performance (for homogeneous objects measurements) with the reported TR-DOS prototypes that use commercial and expensive detectors. The TG-TR-DOS prototype has acquired raw data with a low level of noise and high dynamic range that enable this prototype to measure multilayered objects such as human heads. Second, building and evaluating TR-DOI prototype that uses a computationally efficient algorithm to reconstruct high quality 3D tomographic images by analyzing a small part of the acquired data.

This work indicates the possibility to exploit the recent advances in the technologies of silicon detectors, and computation to build low-cost, compact, portable TR-DOI

systems. These systems can expand the applications of TR-DOI and TR-DOS into several fields such as oncology, and neurology.

Acknowledgments

I would like to thank my supervisor, Prof. M. Jamal Deen for the support and guidance during my PhD study. I have learned many skills from you during these years, which will help me in my prospective work as a researcher. These skills of research include critical thinking, planning of experiments, problem-solving, data analysis and writing of scientific articles. Also, I would like to thank Prof. Deen for the training he provided to me in all aspects and presentation to people with different education levels and backgrounds. It was a great honor for me to work under the supervision of such an outstanding professor.

I would like to thank the members of my supervisory committee Prof. Shiva Kumar, Dr. Troy Farncombe and Dr. Hao Peng for their constructive advice. I would also like to thank our group members Dr. Darek Palubiak, Dr. Zhiyun Li, Dr. Tianyi Guo, Dr. Zeng Cheng, Dr. Xiaoqing Zheng, Dr. Yiheng Qin, Dr. Si Pan, Dr. Mohamed Naser, Arif Alam, Sumit Majumdar, Wei Jiang, Yamn Chalich and Abu Ilius Faisal who all engaged me in constructive discussions during this work. I would also like to thank Dr. Thomas Farrell for allowing me to use his lab equipment to calibrate my samples. I would also like to thank Tyler Ackland for his technical services.

I would like to express my deep appreciation and thanks to my employer KACST who sponsored my PhD study. I extend my deepest thanks to my director Dr. Munir Eldesouki who supported me to complete my PhD study. Finally, I would like to thank all members of my family who have always supported me in all the aspects of my life.

List of Abbreviations

BIP	Basic Instrumental Performance
BSI	Back-Side Illuminated
CMOS	Complementary Metal-Oxide-Semiconductor
CPS	Counts Per Second
CT	Computed Tomography
CW	Continuous Wave
DCR	Dark Count Rate
DE	Diffusion Equation
DNL	Differential Non-Linearity
DOI	Diffuse Optical Imaging
DOS	Diffuse Optical Spectroscopy
DOT	Diffuse Optical Tomography
DR	Dynamic Range
DToF	Distribution Time of Flight
FD	Frequency Domain
FEM	Finite Element Method
FF	Fill-Factor
FLIM	Fluorescence Lifetime Imaging
fMRI	Functional Magnetic Resonance Imaging
fNIRS	Functional Near-Infrared Spectroscopy
FoMs	Figures-of-Merit
FoM _C	Figure-of-Merit for photon counting
FoM _T	Figure-of-Merit for photon timing
FR	Free-Running
FSI	Front-Side Illumination
FWHM	Full-Width Half Maximum
GPU	Graphics Processing Unit
HHb	Deoxyhemoglobin
HbO ₂	Oxyhemoglobin
ICCD	Intensified Charge Coupled Device
IRF	Instrument Response Function
IRF _{Total}	Total Instrument Response Function
MC	Monte Carlo
MCP-PMT	Micro-Channel Plate Photomultiplier Tubes
MPE	Maximum Permissible Exposure
MRI	Magnetic Resonance Imaging
ND	Neutral Density
NIR	Near Infrared
NIRF	Near Infrared Fluorescence
NIRS	Near Infrared Spectroscopy
OCT	Optical Coherence Tomography
OP	Optical Properties
OT	Optical Topography
PDE	Photon Detection Efficiency

PET	Positron-Emission Tomography
PMT	Photomultiplier Tube
PTA	Photon Time of Arrival
QE	Quantum Efficiency
QTH	Quartz Tungsten Halogen
ROI	Region Of Interest
RR	Repetition Rate
RTE	Radiative Transfer Equation
SDD	Source Detector Distance
SiPMs	Silicon Photomultipliers
SNR	Signal-to-Noise Ratio
SPADs	Single-Photon Avalanche Diodes
StO ₂	Tissue Oxygen Saturation
TCSPC	Time-Correlated Single-Photon Counting
TDCs	Time-to-Digital Converters
TD-DE	Time-Dependent Diffusion Equation
T _{DEAD}	Dead-Time
TD-RTE	Time-Dependent Radiative Transfer Equation
TG	Time-Gated
tHb	Total-Hemoglobin
TiO ₂	Titanium Dioxide
TPSF	Temporal Point Spread Function
TR	Time-Resolved
TR-DOI	Time-Resolved Diffuse Optical Imaging
TR-DOS	Time-Resolved Diffuse Optical Spectroscopy
TR-DOT	Time-Resolved Diffuse Optical Tomography
VCSEL	Vertical-Cavity Surface-Emitting Laser

Table of Contents

Chapter 1 Introduction.....	1
1.1. Diffuse Optical Spectroscopy Approaches.....	3
1.2. Thesis Motivation.....	6
1.3. Research Contributions.....	7
1.4. Thesis Overview.....	9
Chapter 2 Background and Review.....	11
2.1. Fundamentals of Diffuse Optics.....	11
2.2. Theory of Time-Resolved Diffuse Optics.....	14
2.3. Components of TR-DOI Systems.....	15
2.3.1. Light Sources.....	16
2.3.2. Turbid Media.....	18
2.3.3. Photons Counting and Timing.....	20
2.3.4. Data Analysis Tools.....	23
2.4. Performance Parameters of TR-DOS Systems.....	27
2.4.1. Light Illumination Properties.....	27
2.4.2. Detection Features.....	28
2.4.3. Photon Timing Histogram.....	29
2.4.4. TR-DOS Systems.....	30
2.4.5. TR-DOI Systems.....	31
2.5. TR-DOS using SPAD and SiPM.....	32
2.5.1. SPADs.....	33
2.5.2. SiPMs.....	35
2.5.3. SPADs Operation modes.....	35
2.5.4. Features of the Detectors.....	37
2.5.5. FR vs. TG TR-DOS.....	37
2.6. Discussions and Research Challenges.....	38
2.7. Conclusions.....	42
Chapter 3 Integration and Evaluation for A Computationally Efficient Time-Resolved Diffuse Optical Tomography System.....	44
3.1. Introduction.....	44

3.2. Prototype Architecture.....	47
3.2.1. TR-DOS setup.....	47
3.2.2. Image Reconstruction Process.....	48
3.3. Measurements.....	50
3.3.1. Phantoms and Inclusions.....	51
3.3.2. Instrument Response Function.....	52
3.3.3. Data Acquisition.....	53
3.3.4. Quantification Accuracy of the OP.....	55
3.4. Results and Discussions.....	56
3.4.1. Image Reconstruction on Phantoms.....	57
3.4.2. Impact of Number of Sources.....	59
3.4.3. Impact of Number of Detectors.....	61
3.4.4. Influence of Prior Knowledge.....	63
3.4.5. Influence of ROI Size.....	65
3.5. Conclusions.....	66

Chapter 4 Development of a Time-Resolved Diffuse Optical Spectroscopy Prototype Using Low-cost and Compact SPAD Detectors

.....	69
4.1. Introduction.....	70
4.2. TR-DOS Prototype.....	72
4.2.1. Light Sources.....	73
4.2.2. Photon Counting and Timing Subsystem.....	74
4.2.3. Data Analysis Tool.....	74
4.3. Characterization Methods.....	76
4.3.1. Basic Instrumental Performance Protocol.....	76
4.3.2. Optical Properties Quantification of Homogeneous Phantoms.....	78
4.4. Results and Discussions.....	83
4.4.1. Differential Non-Linearity.....	83
4.4.2. Total Instrument Response Function.....	84
4.4.3. The Accuracy of the OP Quantification.....	86
4.4.4. The Linearity of the OP Quantification.....	86
4.4.5. Evaluation of this Prototype and the Potential Applications.....	87
4.4.6. Potential Developments of SPAD Detectors for Tissue Optics Applications.....	89

4.5. Conclusions.....	91
Chapter 5 Time-Gated Time-Resolved Diffuse Optical Spectroscopy	
Prototype for Multilayered Turbid Media	92
5.1. Introduction.....	93
5.2. TG-TR-DOS Prototype.....	93
5.2.1. TG-TR-DOS Setup.....	94
5.2.2. Phantoms	95
5.2.3. Data Acquisition and Preprocessing.....	96
5.2.4. Preliminary Measurements.....	97
5.3. Simulation.....	100
5.3.1. Light Propagation in Two-Layered Phantoms	102
5.3.2. FR-DToF vs. TR-DToF.....	103
5.3.3. OP Quantification using TR-DToF Curves.....	105
5.4. Measurements	106
5.4.1. Measurements Conditions	107
5.4.2. Results and Discussion.....	108
5.5. Conclusions.....	109
Chapter 6 Conclusions and Recommendations	111
6.1. Conclusions.....	111
6.2. Recommendations for Future Work	113
Appendix I: Matlab Codes.....	116
Appendix II: Copyright Permissions	125
References.....	134

List of Figures

Figure 1-1: Examples of the medical imaging modalities over the electromagnetic spectrum, and the information obtained for each. Reprinted with Creative Commons Attribution License from [4].	2
Figure 1-2: Approaches for DOS: (a) CW, (b) FD, and (c) TR. The arrow shows a trend of increasing the cost, the complexity of instrumentation and the acquired information about the measured object.....	5
Figure 1-3: Evolution of single-photon counters according to their size and cost.	7
Figure 2-1: (a) Optical Window and (b) Extinction coefficients of hemoglobin components HbO ₂ (red) and HHb (green). Reprinted from [27] with permission granted.....	12
Figure 2-2: Forward problem solver versus inverse problem solver in diffuse optics.	13
Figure 2-3: Main components of a typical TR-DOI prototype and the role of each one. From left to right: light illumination, a turbid medium, photon timing, and image reconstruction tool.	16
Figure 2-4: Shapes of DToF curves for a homogeneous turbid medium according to different OP and SDD = 3 cm. (a) Variable reduced scattering coefficients; (b) Variable absorption coefficients; and (c) Variable reduced scattering and absorption coefficients.	19
Figure 2-5: Photons reached areas within the turbid medium for each time gate window with different delays. (a) An illustration of increasing the reachable depths for photons detected at late gates. (b) The positions of gates on the DToF histogram and the possible reachable depth of detected photons during each gate.....	21
Figure 2-6: DToF histogram obtained by measuring the delay between the laser pulse and PTA. Top-left (in red and green borders) show two methods to synchronize the laser pulse with the detected photons. Top-right (blue border) illustrates how the counted photons are stored in the DToF histogram according to the differences in delay for each one of them. ...	23
Figure 2-7: Recovering the optical properties of time-resolved DOS reflectance measurement for a homogeneous turbid medium.....	24
Figure 2-8: Flow diagram of a TR-DOT prototype, the left, and right side represent the measurement setup (DOS) and the flowchart of the inverse modeling, respectively.	26
Figure 2-9: Broadening of measured DToF. Main contributions of the broadening are the time of flight of photons in a turbid medium, the noise of the setup and the IRF of laser source, detector, and TDC/TCSPC.....	30
Figure 2-10: Comparison of the Absorption coefficients for some semiconductor materials over the wavelengths range of visible and NIR light [132].	32

Figure 2-11: Compromise of SPAD: blue and green curves represent the IRF_{SPAD} and the PDE changes with increasing thickness of depletion layer and the size of the active area respectively, whereas the black line indicates the maximum acceptable IRF_{SPAD}	34
Figure 2-12: Photon counting process for identical incident photons using (a) FR detector, (b) TG detector. Reasons for missing photons are indicated on the right for each operation mode.....	36
Figure 2-13: Components of TR-DOS prototypes using (a) FR Detector, (b) TG Detector.....	38
Figure 3-1: Diagram of the time-resolved diffuse optical tomography (TR-DOT) prototype.	48
Figure 3-2: Diagram of steady-state spatially resolved diffuse reflectance system used to determine the optical properties (OP) accurately for the phantoms and the inclusion materials.	52
Figure 3-3: The FWHM of the IRF_{Total} of our TR-DOS setup (~ 0.3 ns) and the acquired DToF at 180°	53
Figure 3-4: Flowchart of the integrated TR-DOT prototype.	54
Figure 3-5: Cross-correlation of the actual OP of the inclusion versus the recovered OP for inclusion and background of the first phantom (one inclusion). (a) Recovered μ_s' against actual μ_s' ; (b) Recovered μ_a against actual μ_a ; (c) Recovered μ_a against actual μ_s' ; and (d) Recovered μ_s' against actual μ_a	56
Figure 3-6: Cross-sectional and sagittal views of images for actual μ_s' (left) and μ_a (right) coefficients for two phantoms: (row one) the first phantom, and (row two) the second phantom.	57
Figure 3-7: Left column: cross sectional and sagittal views of images. Right column: the recovered μ_s' and μ_a for: the first phantom (rows one and two), and the second phantom (rows three and four).	58
Figure 3-8: Left column: Cross-sectional and sagittal views of images. Right column: the recovered μ_s' and μ_a for the second phantom: 12 sources and 84 detectors (rows one and two), and 6 sources and 42 detectors (rows three and four).....	60
Figure 3-9: Left column: Cross-sectional and sagittal views of images. Right column: the recovered μ_s' and μ_a for the second phantom: 12 sources and 84 detectors (rows one and two), 12 sources and 60 detectors (rows three and four), and 12 sources and 48 detectors (rows five and six).	62
Figure 3-10: Left column: cross sectional and sagittal views of images. Right column: the recovered μ_s' and μ_a for the first phantom: with hard prior (rows one and two), and without prior knowledge (rows three and four).	64

Figure 3-11: Left column: cross sectional and sagittal views of images. Right column: the recovered μ_s' and μ_a for the second phantom without prior knowledge: 1.5 cm ROI (rows one and two), and 1.8 cm ROI (rows three and four).	66
Figure 4-1: (a) Diagram of main components of the TR-DOS prototype; (b) light source and detector arrangement (28 mm source-detector distance) that are attached to the surface of phantoms; and (c) a sample of the homogeneous phantoms.....	73
Figure 4-2: Flowchart of the data analysis process to recover the OP of the phantoms using the TR-DOS prototype.	75
Figure 4-3: DNL measurement setup to acquire histograms of the PTA for all detected photons.....	78
Figure 4-4: The IRF_{Total} versus the measured DToF histograms for the phantoms: (a) high scattering phantoms with variable μ_a at 685 nm; (b) high scattering phantoms with variable μ_a at 830 nm; (c) high absorption phantoms with variable μ_s' at 685 nm; and (d) high absorption phantoms with variable μ_s' at 830 nm.	82
Figure 4-5: DToF _{Measured} curves and DToF _{Fitted} curves for B2 phantom with SDD = 2.8 cm: (a) at 685 nm; and (b) at 830 nm.	83
Figure 4-6: Histogram of PTA distributions for 10^7 counted photons in all time bins (1000 bins for 20 ns range).	84
Figure 4-7: FWHM of IRF_{Total} of the TR-DOS prototype at two different wavelengths used in this Chapter: (a) 685 nm at low optical power (0.05 mW); (b) 830 nm at low optical power (0.06 mW); (c) 685 nm at the used optical power (2.2 mW) to illuminate the phantoms; and (d) 830 nm at the used optical power (3.6 mW) to illuminate the phantoms.	85
Figure 4-8: The linearity of the retrieved OP versus the actual OP for nine phantoms at two different wavelengths: (a) and (b) represent the retrieved μ_s' against the actual μ_s' at 685 and 830 nm, respectively; (c) and (d) represent the retrieved μ_a against the actual μ_a at 685 and 830 nm, respectively; (e) and (f) represent the retrieved μ_a against the actual μ_s' at 685 and 830 nm, respectively; and (g) and (h) represent the retrieved μ_s' against the actual μ_a at 685 nm and 830 nm, respectively.....	88
Figure 5-1: The architecture of the TG-TR-DOS prototype and the equipment used and software.....	95
Figure 5-2: (a) Extracting the useful portion from DToF curves for each gate; and (b) example of reconstituting full TG-DToF from rescaled DToF for 6 gates; reprinted with permission from [197].	96
Figure 5-3: (a) Flowchart of data acquisition and preprocessing from the TG-TR-DOS setup; (b) example of rescaling and reconstitution processes; reprinted with permission from [197].	97

Figure 5-4: Nominal delays of the delay unit versus the measured delays using the oscilloscope.....	98
Figure 5-5: IRF_{Total} of TG-TR-DOS setup using an optical power of 3 mW to illuminate the phantoms.....	99
Figure 5-6: Reconstitution process for the measured DToF curves of four gates for two-layered phantoms (thickness of upper layer = 10 mm and lower layer = 27 mm); (a) the measured DToF curves; (b) the scaled measured DToF curves and the full-TG-DToF; and (c) the IRF_{Total} of the TG-TR-DOS setup versus the full-TG-DToF.	101
Figure 5-7: Light propagation in two bi-layered phantoms (thickness of upper layer = 10 mm and lower layer = 27 mm) during four gates. Left column: the first phantom; and right column: the second phantom.....	102
Figure 5-8: Outcomes of the reconstitution algorithm in the simulation for two bi-layered phantoms (thicknesses of upper layer = 10 mm and lower layer = 27 mm), with SDD = 2.5 cm. Left column: The first phantom. Right column: The second phantom. (a) and (b) acquiring normalized DToF curves using four gates; (c) and (d) scaling the DToF curves and reconstituting full TG-DToF curve; (e) and (f) comparing the full-TG-DToF curve versus the FR-DToF curve.	104
Figure 5-9: Retrieving the OP using two TG-DToF curves with SDD = 2.5 cm and 3.5 cm; for (a) the first phantom; and (b) the second phantom.	105
Figure 5-10: Positions of the source and detector attached to the sheep head.....	107
Figure 5-11: Measured raw data for Ex vivo sheep head using FR and TG detectors with SDD = 2.5 cm; (a) acquired DToF curves for four gates; (b) Scaled DToF curves for four gates and the full-TG-DToF curve; (c) Comparison of TG-DToF curve versus FR-DToF curve and the TG- IRF_{Total} versus FR- IRF_{Total}	108
Figure 5-12: Comparison of the smoothed measured DToF curves for ex vivo sheep head using FR and TG detectors and their corresponding TG- IRF_{Total} and FR- IRF_{Total}	109
Figure 6-1: Proposed TG CMOS-SPAD detector to harvest the re-emitted photons using up to ten gates with a fixed synchronization delay.	115

List of Tables

Table 1.1: Main Differences between the three DOS approaches.	4
Table 2.1: Main features of SPADs and SiPM detectors used in TR-DOS prototypes.	37
Table 4.1: The nominal OP of the measured phantoms.....	80
Table 4.2. Relative errors in the accuracy assessment of the retrieved μ_s' and μ_a versus the actual μ_s' and μ_a for nine phantoms at two different wavelengths.....	86
Table 5.1: Main performance features of SPAD Detectors.	94
Table 5.2: Deviations between the nominal and the actual delays.	99

Chapter 1

INTRODUCTION

Spectroscopy and imaging technologies have emerged in the recent decades due to the developments for several types of detectors that are capable of measuring waves and particles that are not noticeable by the human senses [1] [2]. Nowadays, it is possible to detect several kinds of signals over a wide range of wavelengths in the electromagnetic spectrum [2]. Therefore, many spectroscopic and imaging technologies have been invented to measure a wide range of wavelengths, mainly from very short wavelengths (ionizing radiation such as gamma ray and x-ray), short wavelengths (non-ionizing radiation such as visible and infrared light), and very long wavelengths (radio waves) [1] [2] [3]. These spectroscopic and imaging technologies have many applications in several fields such as military, industry, and medicine. Figure 1-1 shows examples for the medical imaging modalities and the obtained information over several ranges of wavelengths in the electromagnetic spectrum [4]. Also, Figure 1-1 displays an example of a medical imaging modality (ultrasound) which use sound waves instead of electromagnetic waves.

Ionizing radiations have been widely used to build medical imaging systems due to their high penetration capabilities through objects such as human body and tissues [2]. Therefore, there are safety restrictions to protect patients from the overdose of ionizing radiation exposure [5]. These safety restrictions hinder the over usage for some medical imaging systems such as **positron-emission tomography (PET)** and **computed tomography (CT)** for patients, particularly when continuous monitoring is needed [6]. However, using non-ionizing radiation for spectroscopy and imaging systems for medical applications is an attractive approach due to their limited hazards for human tissues relative to the ionization radiation [6]. In recent decades, significant efforts have

been achieved in the biophotonics field to develop several technologies of spectroscopy and imaging using low power non-ionizing radiations such as visible and infrared light [7].


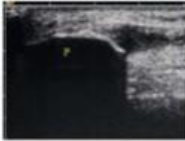
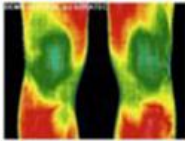



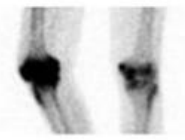
	Radiation / Wavelength	Modality	Medical information
<p>Low Energy</p> <p>High Energy</p>	Radio Wave 10^{-3}	 MRI image	<i>Anatomy</i> Edema, flow Chemical composition
	Microwave 10^{-2}	 Ultrasound	<i>Anatomy</i> Tissue structure characteristics, flow
	Infrared 10^{-5}	 Infrared Imaging	<i>Anatomy and Physiology</i> Surface temperature
	Visible Light 10^{-6}	 Arthroscopy	<i>Anatomy</i> Intraarticular structure, inflammation
	Ultraviolet 10^{-8}	 UV-radiation	<i>Healing/Therapy</i> Skin, chronic Inflammation
	X-Ray 10^{-10}	 X-Ray	<i>Anatomy</i> Bone injuries
	Gamma ray 10^{-12}	 Scintigraphy	<i>Physiology</i> Inflammation, metabolism of the bone

Figure 1-1: Examples of the medical imaging modalities over the electromagnetic spectrum, and the information obtained for each. Reprinted with Creative Commons Attribution License from [4].

Near-infrared (NIR) and red light have become an attractive source of light to be used for several spectroscopic and imaging applications due to the low absorption of red and NIR light by water [8]. Thus, red and NIR light can penetrate translucent objects such as human tissues up to a few centimeters [8] [9]. This ability of the red and NIR light to penetrate biological tissues allow detecting transmitted light through thin organs and tissues, and detecting reflected light from thin and thick organs and tissues, respectively [8] [9].

Red and NIR light lose the wave-like nature when traveling through most biological tissues for more than a few mm (1 mm – 3 mm) due to the domination of the scattering interactions [8] [10]. Therefore, propagated and re-emitted light are dealt with as particles (photons), and these photons are described as diffused photons [8]. Thus, the field of optical spectroscopy using diffuse red and NIR light is usually called **diffuse optical spectroscopy (DOS)** and **near-infrared spectroscopy (NIRS)** [8]. Unlike ionizing radiation-based medical imaging, it is not possible to acquire straightforward cross-sectional images from the measured signals of DOS [11]. For instance, the inverse problems are well posed and linear for x-ray and CT systems because they depend on measuring the transmitted ray, since the scattered ray from the measured objects is negligible and ignored in the image reconstruction process [12]. However, the inverse problems are non-linear and ill-posed for **diffuse optical imaging (DOI)** systems because they depend on measuring light that is highly scattering [12]. Therefore, sophisticated mathematical algorithms are required to reconstruct images of the measured objects from the measured signals of DOS systems [11]. So, a DOS system should be integrated with an inverse problem solver to perform a **diffuse optical imaging (DOI)** system [9]. There are two approaches of DOI — **optical topography (OT)** and **diffuse optical tomography (DOT)** [9]. In practice, useful information about the measured objects can be obtained by analyzing the DOS signals, OT or DOT images [9].

1.1. Diffuse Optical Spectroscopy Approaches

DOS measurements approaches are classified into three categories: **continuous wave (CW)**, **frequency domain (FD)**, and **time-resolved (TR)** [8] [13] [14]. CW usually

has dozens of sources and detectors that restrict the scalability of the DOI systems and increase the amount of data that must be analyzed to reconstruct the images [15]. Moreover, CW-DOS can only monitor the variation of the optical properties (OP) without estimating the values of optical properties, so its capabilities for structural imaging are limited [16]. FD and TR-DOS can be used to quantify the absolute value of the optical properties. However, with FD-DOS, it is challenging to discriminate depths in reflectance geometry measurements [17]. On the other hand, TR-DOS systems are proven to be the most powerful approach among the three techniques with respect to depth sensitivity, depth selectivity and recovery of the absolute value of the OP of the measured biological objects. Table 1.1 summarizes the main differences between DOS approaches, and Figure 1-2 illustrates the main differences between these three approaches for DOS.

Table 1.1: Main Differences between the three DOS approaches.

Method	Source	Measured Parameters	Highlight Features
Continuous Wave (CW)	CW Laser	<ul style="list-style-type: none"> Light Intensity 	<ul style="list-style-type: none"> Good monitoring of the optical properties changes Not accurate in quantifying of the values of the optical properties Increasing the depth sensitivity requires larger source-detector distance
Frequency Domain (FD)	Modulated Laser Light	<ul style="list-style-type: none"> Light Intensity Phase Shift 	<ul style="list-style-type: none"> Good monitoring of the optical properties changes Good quantification of the values of the optical properties
Time-Resolved (TR)	Ultra-Short Pulsed Laser	<ul style="list-style-type: none"> Histogram of the Photons Counts Time of Flight for Photons 	<ul style="list-style-type: none"> Accurate monitoring of the optical properties changes Accurate quantification of the values of the optical properties More depth sensitivity for deep regions in the turbid media Capable of depth selectivity for multilayered turbid media Increasing the depth sensitivity does not depend on the source-detector distance

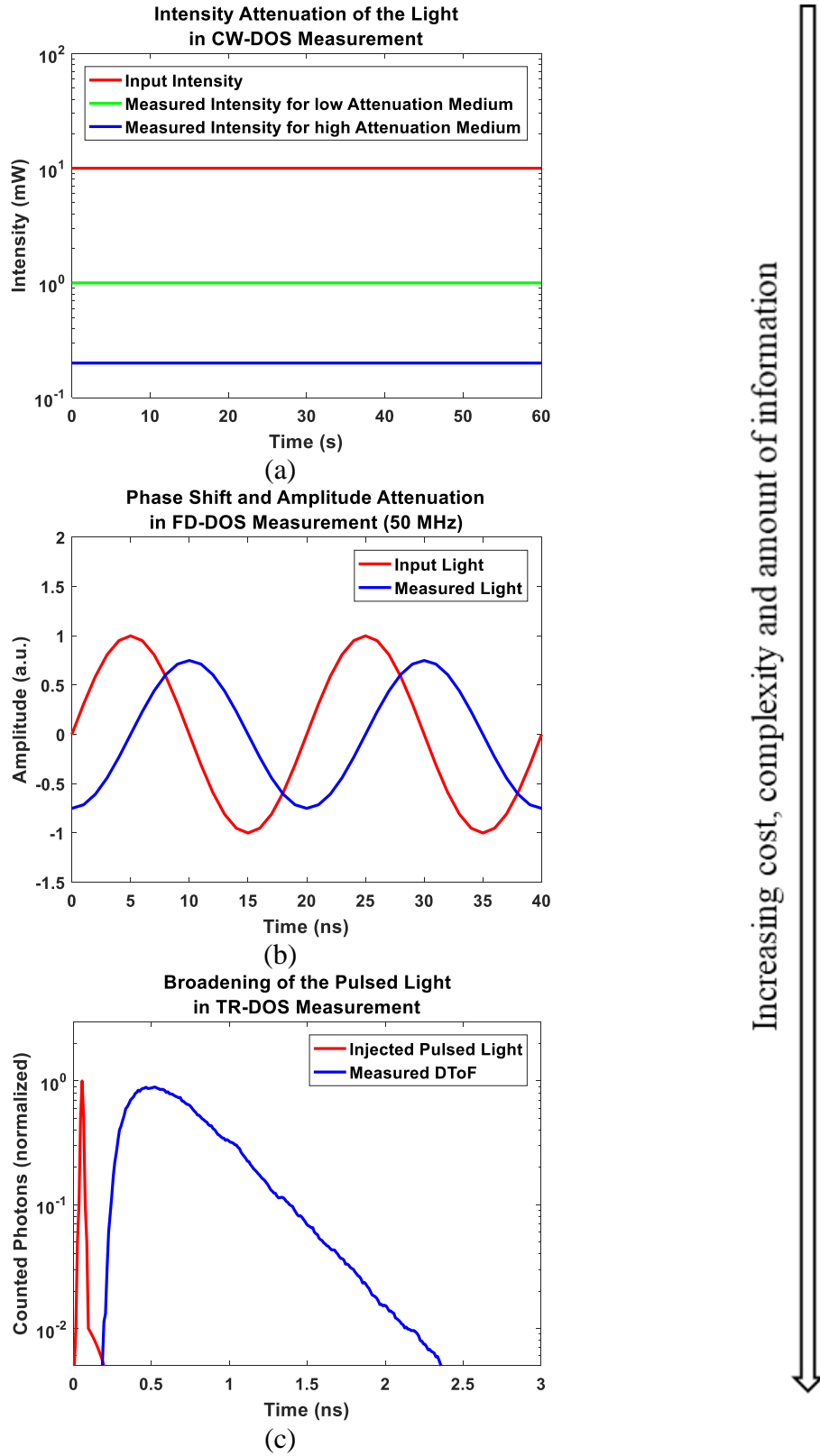


Figure 1-2: Approaches for DOS: (a) CW, (b) FD, and (c) TR. The arrow shows a trend of increasing the cost, the complexity of instrumentation and the acquired information about the measured object.

1.2. Thesis Motivation

DOS and DOI are growing non-invasive tools to analyze the chemical composition for translucent objects using red and NIR light [18]. The chemical compositions for objects, such as the concentrations for each chromophore in biological tissues, can be distinguished according to their optical properties at specific wavelengths [18]. Fortunately, most biological tissues are translucent at red and NIR wavelengths, which allows emerging for several medical applications such as **NIR fluorescence (NIRF)** and **optical coherence tomography (OCT)** [8]. Therefore, significant efforts have been made in the recent three decades to study the optical properties of translucent materials and chromophores, particularly in biological tissues [19]. Also, several DOS and DOI have been built and evaluated for some medical applications such as functional monitoring of brains and muscles, and optical imaging for breasts [20]. Since the 1990s, it was shown that TR is the best approach to build DOS and DOI systems to obtain the richest information about the measured objects [9]. However, wider use of TR-DOS and TR-DOI systems are hindered by the high cost, complexity and large-size for the required sophisticated instruments [21].

In recent years, significant hardware and software developments have made it possible for new-generation of low-cost and compact TR-DOS and TR-DOI systems [22]. First, the computation technologies that allow for solving iterative inverse problems to reconstruct 3D tomographic images for the measured objects in a short computation time [23] [24]. Second, silicon photodetector technologies are being used to reduce the cost and size for single-photon counting and timing systems. Figure 1-3 illustrate the evolution of single-photon counters in recent decades that has led to significant reductions for the cost and the size of the detection instruments. Size and cost have reduced by more than three orders of magnitude during the last three decades [21].

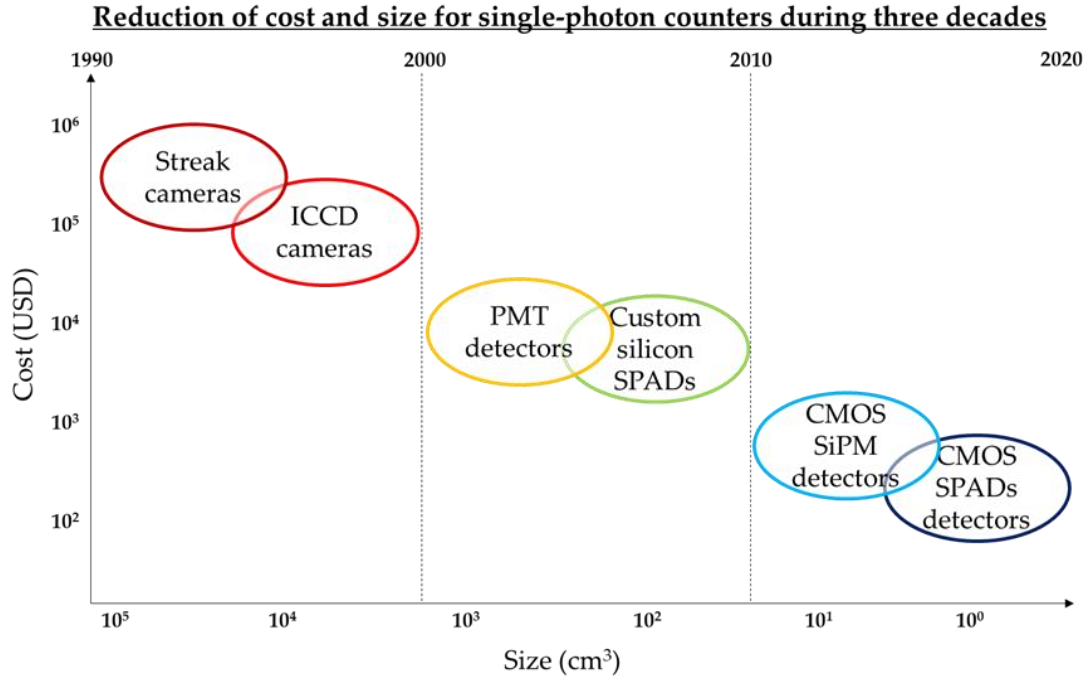


Figure 1-3: Evolution of single-photon counters according to their size and cost.

In silicon technologies, it is also possible to integrate the photodetectors with **time-to-digital converters (TDCs)** to build low-cost and compact photon counting and timing multichannel systems [21]. These recent advances have led to a significant reduction of cost, size, and complexity of the detection instruments in TR-DOS and TR-DOI systems [21]. Therefore, these potential developments require investigations towards building computationally efficient, low-cost, compact, and portable new-generation TR-DOI systems [21] [25]. These optical imaging systems can be used to continuously monitor patients without the necessity for ionizing radiation exposure from traditional medical imaging technologies such as CT or PET [6]. Also, these optical imaging systems can be a good alternative for high-cost medical imaging systems such as **functional magnetic resonance imaging (fMRI)** [6].

1.3. Research Contributions

This research work has resulted in contributions to four main issues towards simplifying TR diffuse optics systems:

1. Review the cutting-edge technologies of the equipment that are required to build TR diffuse optics systems. Thus, the limitations and potential improvements were determined for each category of equipment. Based on the

detailed review, three prototypes have been built to investigate the following important issues.

2. A **time-resolved diffuse optical tomography (TR-DOT)** prototype was built to reconstruct high quality 3D images for turbid media in a short time. This prototype has been evaluated according to several conditions such as different arrangements of sources and detectors, and the presence and absence of the prior knowledge of the anatomy of the measured object.
3. An integrated **free-running (FR) TR-DOS** system using a low-cost and compact custom-designed FR CMOS SPADs detector was constructed. The performance of this system was evaluated by accurately recovering the OP of homogeneous turbid media. Several possible improvements for the custom designed SPAD detectors based on CMOS technology are proposed towards realizing high-efficiency FR CMOS SPAD detectors for multichannel FR-TR-DOS systems.
4. A **time-gated (TG) TR-DOS** system has been built using a custom designed TG CMOS SPADs detector. Fast time-gating detection has enhanced the dynamic range of the measured data with a lower level of noise relative to the free running TR-DOS system. An algorithm has been developed to preprocess the measured data for each used gate and reconstitute the full TG-DToF curves. This algorithm has demonstrated good agreement for simulated data and measured data.

Peer Reviewed Publications:

1. Alayed, M. and Deen, M.J., 2017. Time-resolved diffuse optical spectroscopy and imaging using solid-state detectors: characteristics, present status, and research challenges. *Sensors*, 17(9), p.2115, pp. 1-36.
2. Alayed, M., Naser, M.A., Aden-Ali, I. and Deen, M.J., 2018. Time-resolved diffuse optical tomography system using an accelerated inverse problem solver. *Optics Express*, 26(2), pp.963-979.
3. Alayed, M., Palubiak, D. and Deen, M., 2018. Characterization of a Time-Resolved Diffuse Optical Spectroscopy Prototype Using Low-Cost, Compact

Single Photon Avalanche Detectors for Tissue Optics Applications. *Sensors*, 18(11), p.3680, pp. 1-18.

Conference/Symposium participation:

1. Mrwan Alayed, Darek Palubiak, and M. Jamal Deen, “Time-Resolved Near-Infrared Spectroscopy Using Custom-Made SPADs and Time-Digital-Converter” Poster in 5th Annual McMaster Biomedical Engineering Symposium, January 2016.

1.4. Thesis Overview

The contents of this thesis are organized as follows. In Chapter 1, a brief background of DOS and DOI is introduced, and the motivations of this work are presented. Then, the contributions of this research are given.

In Chapter 2, theoretical and practical concepts of diffuse optics field are explained. The main components of DOI are described. The evaluation parameters for TR-DOS and TR-DOI systems and the detectors are defined. Lastly, the potential developments for each component in TR-DOS and TR-DOI systems are discussed.

In Chapter 3, a computationally efficient TR-DOT prototype was built and evaluated according to several measurements conditions. With this prototype, we can reconstruct high quality 3D tomographic images within a short time if the prior knowledge of the anatomy of the measured object is used. Such a system can be suitable for follow-up treatments for some diseases such as breast cancer tumor and hemorrhages in a newborn’s brain.

In Chapter 4, a free-running TR-DOS prototype using a low-cost and compact CMOS SPAD detector was built and evaluated. The potential developments for custom-designed CMOS SPAD detectors are discussed, and the importance of each performance specification is provided. The proposed SPAD detectors in a multichannel format can be used to build low-cost and compact topographic and tomographic imaging systems for functional monitoring of brain and muscles, and for optical mammography. However, the main limitation of this prototype is the limited dynamic range of the detection system for the measured data. Significant improvement of the

dynamic range can be achieved by building a time-gated TR-DOS system or designing free-running CMOS SPAD detectors with lower noise.

In Chapter 5, a time-gated TR-DOS prototype using a custom designed fast gating CMOS SPAD detector was built. This prototype demonstrated a much higher dynamic range for the measured data relative to the free-running TR-DOS prototype described in Chapter 4. This time-gated TR-DOS prototype has been tested for an ex-vivo sample (animal head) and demonstrated that it could be used for some medical applications that require a TR-DOS prototype with a high dynamic range such as in functional brain monitoring. The fast gating CMOS SPAD detector can be used to build a low-cost multichannel time-gated TR-DOS prototype using several source-detector pairs for optical topography and optical tomography in reflectance geometry.

In Chapter 6, the conclusions of the main results are presented. Recommendations for future work are briefly discussed with the main focus on the potential developments based on silicon technology towards realizing a new generation of low-cost, compact and portable TR-DOI prototypes.

Chapter 2

BACKGROUND AND REVIEW¹

In this Chapter, relevant fundamentals of diffuse optics and the theory of time-resolved diffuse optics are explained. Then, time-resolved diffuse optical spectroscopy (TR-DOS) and imaging (TR-DOI) systems using solid-state detectors are described with a particular focus on single-photon avalanche diodes (SPADs) and silicon photomultipliers (SiPMs). These systems can be categorized into two types based on the operation mode of the detector – free-running (FR) or time-gated (TG). For the TR-DOI prototypes, the physical concepts, main components, figures-of-merit of detectors and the evaluation parameters are described. Also, the potential features of SPADs and SiPMs to improve TR-DOS and TR-DOI systems to expand their future applications are discussed. Then, research challenges and possible developments for time-resolved diffuse optical systems are discussed separately for each component in a TR-DOI system and also for the entire system.

2.1. Fundamentals of Diffuse Optics

Diffuse optical spectroscopy (DOS), also known as near-infrared spectroscopy (NIRS), is an optical spectroscopic technique to investigate the interactions between light and matter within the optical window from 600 to 950 nm (Figure 2-1 (a)). In this wavelength range of red and near-infrared light, the absorption of water is very low, and scattering is the dominant light-matter interaction [26] [13]. Also, the main components of the hemoglobin – Oxyhemoglobin (HbO₂) and Deoxyhemoglobin

¹ Most of this chapter was published as: Alayed, M. and Deen, M.J., 2017. Time-resolved diffuse optical spectroscopy and imaging using solid-state detectors: characteristics, present status, and research challenges. *Sensors*, 17(9), p.2115, pp. 1-36.

(HHb) are the most important absorbers in tissues within the biological window (Figure 2-1 (b)).

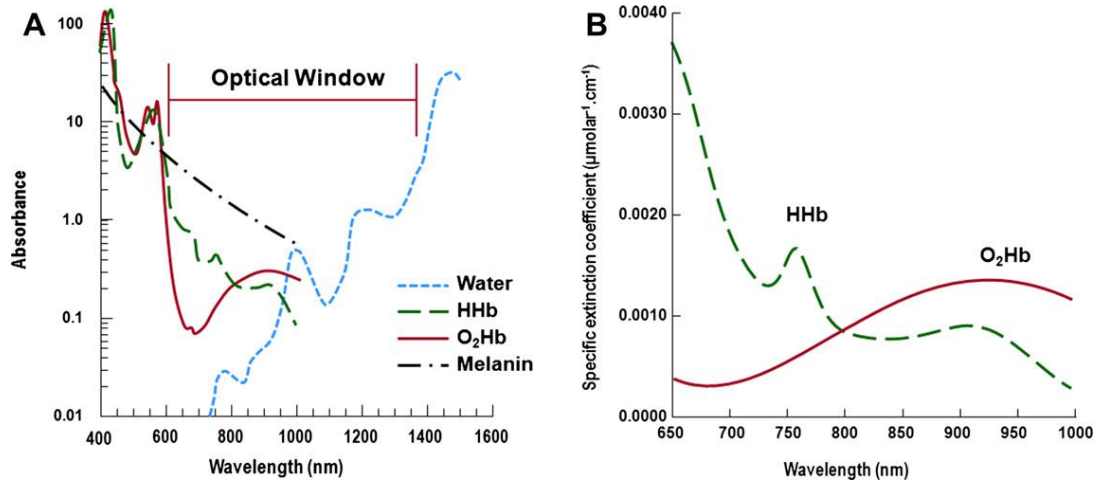


Figure 2-1: (a) Optical Window and (b) Extinction coefficients of hemoglobin components HbO₂ (red) and HHb (green). Reprinted from [27] with permission granted.

The incident light in the range of the biological window can propagate inside highly scattering (turbid) media up to a few centimeters until the diffused photons are absorbed or reemitted out of the medium [20] [28]. The light propagation inside a highly scattering medium is described mathematically (by forward problem) using the **radiative transfer equation** (RTE), or its simplified version, the **diffusion equation** (DE) [12] [29]. These re-emitted photons can be collected using photodetectors in either reflectance geometry or transmittance geometry [8] [10]. The reflectance geometry can be used for both thin and thick objects such as newborn and adult heads respectively, but the reachable depth of collected photons is limited to less than 4 cm. The transmittance geometry is only applicable to thin objects (less than 8 cm of thickness) such as breasts and newborn heads [10] [16]. Different measurement geometries can be achieved using multiple channels for both sources and detectors, but this is more complex and expensive than a scanning approach that moves around one or more source-detector pairs in order to scan the object [30] [31]. After the re-emitted photons are detected, an inverse problem solver is implemented to analyze the raw data of the detected photons from a DOS setup.

In DOS, using the detected photons, three-dimensional (3D) or two-dimensional (2D) images of the **optical properties** (OP) of turbid media are reconstructed. From the reconstructed images, any inclusion or heterogeneity inside the object may be detected,

localized, and its size estimated with good spatial resolution up to a few mm [32] [33]. This combination of a DOS system and inverse modeling are what makes a **diffuse optical imaging (DOI)** prototype [34] [35]. Figure 2-2 illustrates the difference between the forward and inverse problem solvers in the field of diffuse optics.

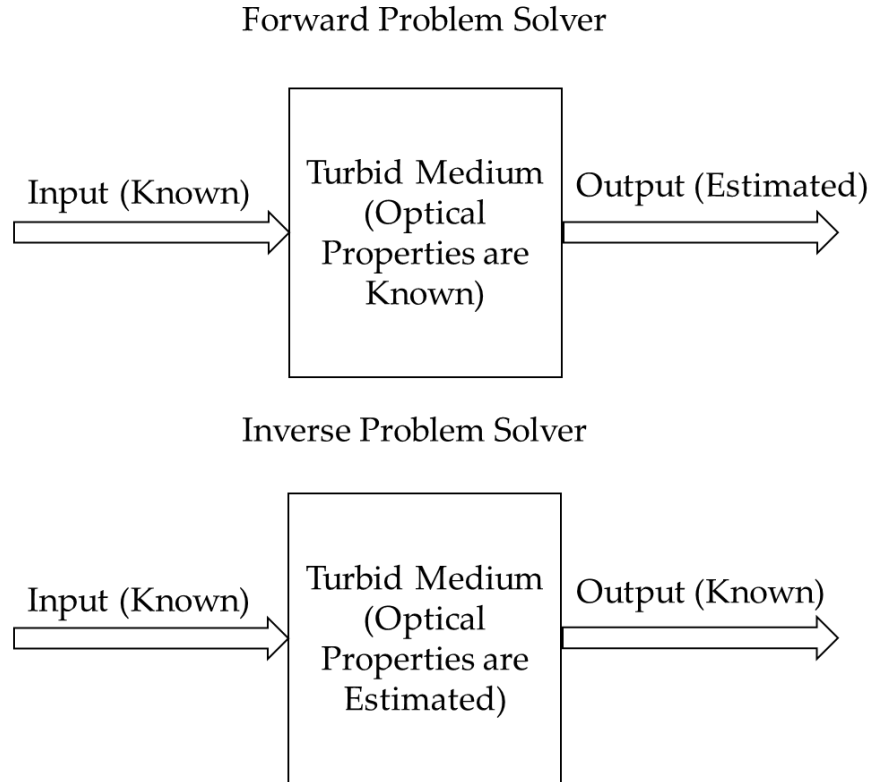


Figure 2-2: Forward problem solver versus inverse problem solver in diffuse optics.

Since the 1970s, DOS has emerged as a powerful technique to explore the OP and compositions of objects in several fields such as agriculture, food and medical imaging [18] [36] [37]. In the last few decades, the applications of DOI for non-invasive tomographic and topographic imaging of tissues and organs have expanded and are known by several names such as **diffuse optical spectroscopy (DOS)** [38], **optical topography (OT)** [39], and **diffuse optical tomography (DOT)** [40]. In this thesis, the term DOS is used to describe either the part of TR prototypes that produce raw datasets, that are histograms of the distribution time of flight for the counted photons, or the prototypes that do not reconstruct images of the objects. On the other hand, the terms DOI and DOT are used to describe any prototype that utilizes an inverse problem solver to reconstruct images from raw data obtained from a DOS system.

DOT systems can produce 2D or 3D images (slices) in transmittance geometry (detectors and sources are not on the same side) for thin objects (less than 8 cm thickness) such as muscles, breasts, and heads of newborn babies [8] [41]. The same can be done in reflectance geometry for thicker or high-absorption tissues, but the depth of the interrogated region in the tissue is shallower than in transmittance geometry [10] [42] [43]. On the other hand, topographic imaging can be applied in reflectance geometry to reconstruct only 2D images from illumination sources and detectors on the same side [10] [16]. DOI systems can be used in optical mammography for tumor detection, localization, and evaluating the response from cancer treatment [44] [45] [46]. Also, functional DOI or functional near-infrared spectroscopy (fNIRS) is used to take images and monitor the changes in OP due to the variation in tissue oxygen saturation (StO₂) and blood flow in the brain during some functional activities [8] [26] [47].

2.2. Theory of Time-Resolved Diffuse Optics

The time-dependent radiative transfer equation (TD-RTE) is the major equation in the diffuse optics field, particularly in time-resolved spectroscopy approach. It is described using the following formula [48] [49]:

$$\left\{ \frac{1}{v} \frac{\partial}{\partial t} + \hat{s} \cdot \nabla + \mu_t(r) \right\} L(r, \hat{s}, t) = \mu_s(r) \int_{4\pi} p(\hat{s}, \hat{s}') L(r, \hat{s}', t) d\Omega(\hat{s}') + Q(r, \hat{s}, t) \quad (2.1)$$

where v represents the speed of light in a turbid medium, which is estimated by dividing the speed of light in vacuum c_0 by the refractive index (n) of the medium ($v = c_0/n$) [48]. Refractive index (n) for tissues ranges from 1.3 to 1.5, which means v in tissues equals (≈ 0.22 mm/ps) [19]. In TD-RTE equation, r , \hat{s} and t represent the position in turbid medium, direction, and time, respectively. Also, $L(r, \hat{s}', t)$ is the radiance (W. sr. m⁻²) which represents the light intensity at a specific position (r) and time (t) in the direction (\hat{s}). The attenuation coefficient (μ_t) equals the sum of the scattering coefficient (μ_s) and the absorption coefficient (μ_a) at position (r) in the turbid medium ($\mu_t(r) = \mu_s(r) + \mu_a(r)$). The scattering phase function $p(\hat{s}, \hat{s}')$ describes the probability of scattering of photons from the direction (\hat{s}) to other direction (\hat{s}') within the solid angle Ω . Lastly, $Q(r, \hat{s}, t)$ represents the light source (injected light into the turbid medium) [48].

The main focus of diffuse optics is to exploit the light-matter interactions in biological tissues to retrieve the OP distribution within the tissue. The probability of each light-matter interaction such as absorption and scattering of photons within a turbid medium is directly related to the values of the OP. The OP values reflect the physiological and pathological status of the biological tissues [50]. Although the OP can be represented in turbid media by several parameters, the main ones in diffuse optics are the reduced scattering coefficient (μ_s'), the absorption coefficient (μ_a) and refractive index (n) [51] [8]. The μ_s' is estimated by removing the impact of the anisotropy factor (g) of scattering ($\mu_s' = \mu_s (1-g)$). In biological tissue, the value of g typically ranges from ~ 0.75 to ~ 0.95 , which leads to the much lower value of μ_s' of tissue relative to μ_s [52].

2.3. Components of TR-DOI Systems

TR-DOS and TR-DOI systems have emerged since the late 1980s [53] [54]. Most of the reported TR prototypes were built in research centers and academic institutions [25]. With the use of TR-DOI, many practical limitations such as large size, high cost and complexity were reduced. These improvements are primarily due to the rapid advances in photodetector technology and timing electronics that led to reducing the cost and the size of photon counting and timing devices by more than three orders of magnitude during the last three decades [21]. Therefore, in this Chapter, compact solid-state detectors such as **single-photon avalanche diodes (SPADs)** and **silicon photomultipliers (SiPMs)** are briefly described. These detectors represent cutting-edge technology in the miniaturization and cost reduction of picosecond photon timing and counting applications such as TR-DOS as shown in Figure 1-3. Therefore, by exploiting solid-state detectors, the use of TR-DOS is expected to expand, and more affordable and portable commercial devices are expected within the next few years [21]. Figure 2-3 illustrates the main components for a typical TR-DOI prototype.

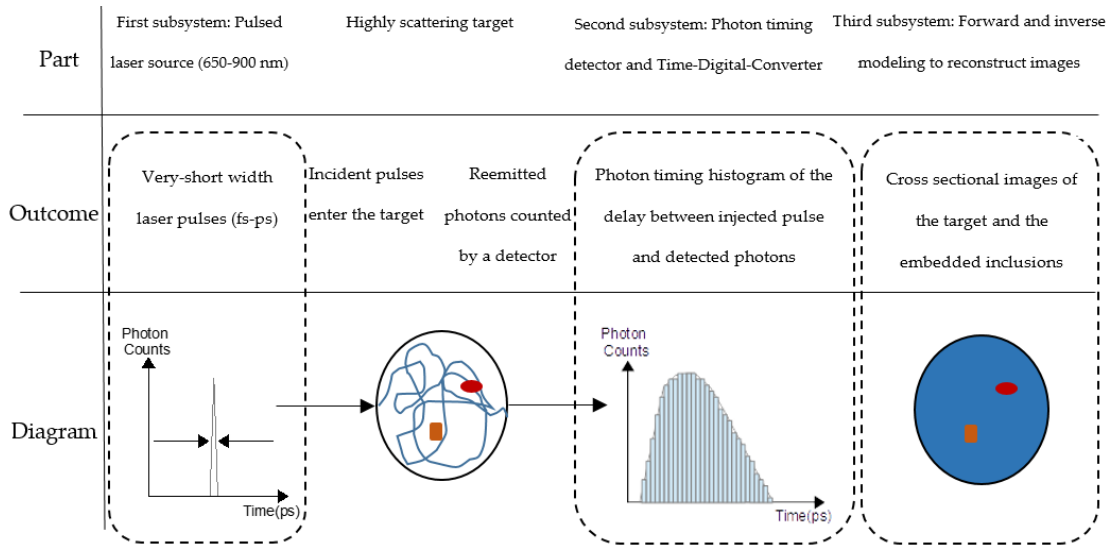


Figure 2-3: Main components of a typical TR-DOI prototype and the role of each one. From left to right: light illumination, a turbid medium, photon timing, and image reconstruction tool.

The first subsystem is one or more pulsed laser sources injecting light into a turbid medium. The second subsystem is for photon counting and timing with high temporal resolution (picosecond range). This is performed by integrating photon counting detector(s) with **time-correlated single-photon counting (TCSPC)** or **time-to-digital converters (TDCs)** to count photons and record the **photon time of arrival (PTA)** for each detected photon. TCSPC or TDC produce histograms of the **instrument response function (IRF)** and the **distribution time of flight (DToF)** that are measured from the delay between the time of the photon arrival and the injected laser pulse. A third subsystem is required to reconstruct images by using forward and inverse modeling to analyze the histograms from the photon timing subsystems and estimate the OP for each point within the turbid medium. Eventually, the size, location, shape and OP of a high-absorbent inclusion such as diseased tissue inside a turbid medium, can be investigated based on the variation of the OP versus surrounding healthy tissue [55].

2.3.1. Light Sources

The light sources should have a very short **full-width-half-maximum (FWHM)** from femtoseconds to a few hundreds of picoseconds, a center wavelength in the range of 600–950 nm, a narrow spectral wavelength ($<\pm 10$ nm), and a high repetition rate (tens of MHz). Light sources in this range of wavelengths can be used to monitor hemodynamics and estimate the concentrations of **oxyhemoglobin (HbO₂)**,

deoxyhemoglobin (HHb), total-hemoglobin (tHb), and tissue oxygen saturation (StO₂). Also, to monitor water and collagen in a turbid medium, light sources of wavelengths longer than 950 nm can be used [56]. However, the use of silicon semiconductor detectors in prototypes for water and collagen is hindered by the poor performance of the detectors at this range of longer wavelengths (see Section 2.5).

Four types of pulsed lasers are usually used in TR-DOS prototypes: pulsed diode laser [46] [57], solid-state laser [54] [58], supercontinuum fiber laser [59] [60], or the recent low-cost pulsed vertical-cavity surface-emitting laser (VCSEL) [61]. Some lab prototypes have used bulky solid-state lasers (such as Mai Tai Spectra-Physics) that have higher power and ultrashort pulse width (FWHM in the tens of fs range), whereas other recent setups were developed by using a supercontinuum fiber laser sources (FWHM in ps range) [54]. Also, pulsed diode lasers usually are used with low average power (a few mW) to maintain a short enough FWHM of the laser pulse (< 300 ps) and to avoid increasing the total IRF (IRF_{Total}) of the system. Therefore, in the literature, it is reported that the pulsed diode lasers maintain low power, which leads to a small contribution from the light source to the IRF_{Total} of the TR prototype [57] [62] [63] [64]. However, pulsed diode lasers are still widely used because of their affordable cost and availability of many models at different wavelengths from several vendors [65] [66] [67] [68]. Also, VCSELs were recently used in TR-DOS prototypes and are projected to be the most widely used pulsed laser sources for future generation of TR-DOS systems due to their compact size and low cost [36].

Although the maximum permissible exposure (MPE) was not specified for some internal tissues such as the brain, the power of the illuminated light must be kept lower than the MPE for skin (1.63 W/cm² for a 785-nm source within 1 second integration time) when the illumination source is chosen [69] [70]. According to the International Electrotechnical Commission standards (IEC 60825-1:2014), MPE values vary depending on the exposure duration and the wavelengths used for illumination, so this should be considered in measurements by DOS prototypes [69]. In addition, to estimate the MPE for skin during a typical experiment (from 10 s up to 8 h) in the NIR range (700 – 1050 nm), a simple formula can be used, where $MPE (W/cm^2) = 0.2 \times C_4$, and $C_4 = 10^{0.002 \times (\lambda - 700 \text{ nm})}$ [69]. Moreover, pulsed lasers with high repetition rates can be

approximated as CW laser by considering the average power of the pulsed laser which is represented by the energy of the pulse multiplied by the number of pulses in 1 s [71]. In this case, the MPE must be considered, especially for DOS prototypes to be used in clinical measurements.

2.3.2. Turbid Media

The most common method to classify highly scattering media is based on the similarity of the values of their OP. Most tissues such as an adult head are heterogeneous, but some tissues such as breasts and neonatal heads can be modeled as homogeneous to simplify the analysis of light propagation [62] [72] [73]. Turbid media are categorized according to their type; that is, whether it is a real turbid medium such as a tissue, or a phantom that mimics the OP of a specific organ or tissue. Phantoms are more common in first-stage experiments because of their flexibility in shape, size, the value of their OP and no permission from ethics boards is required for their use [74]. On the other hand, ethics board approval and patient consent are required for in vivo tissues in clinical experiments according to strict protocols.

In TR-DOS measurements, the shapes of the DToF curves are changed according to the OP of the turbid media. Figure 2-4 shows the simulated DToF curves for a homogeneous turbid medium (4 cm thickness, 8 cm length, and 8 cm width) for variable reduced scattering coefficients, absorption coefficients, and a fixed refractive index at 1.4. It can be observed that the μ_s' values affect the delay of the peaks and the rising edges of the DToF curves, whereas μ_a values affect the slopes of the falling edge of the DToF curves.

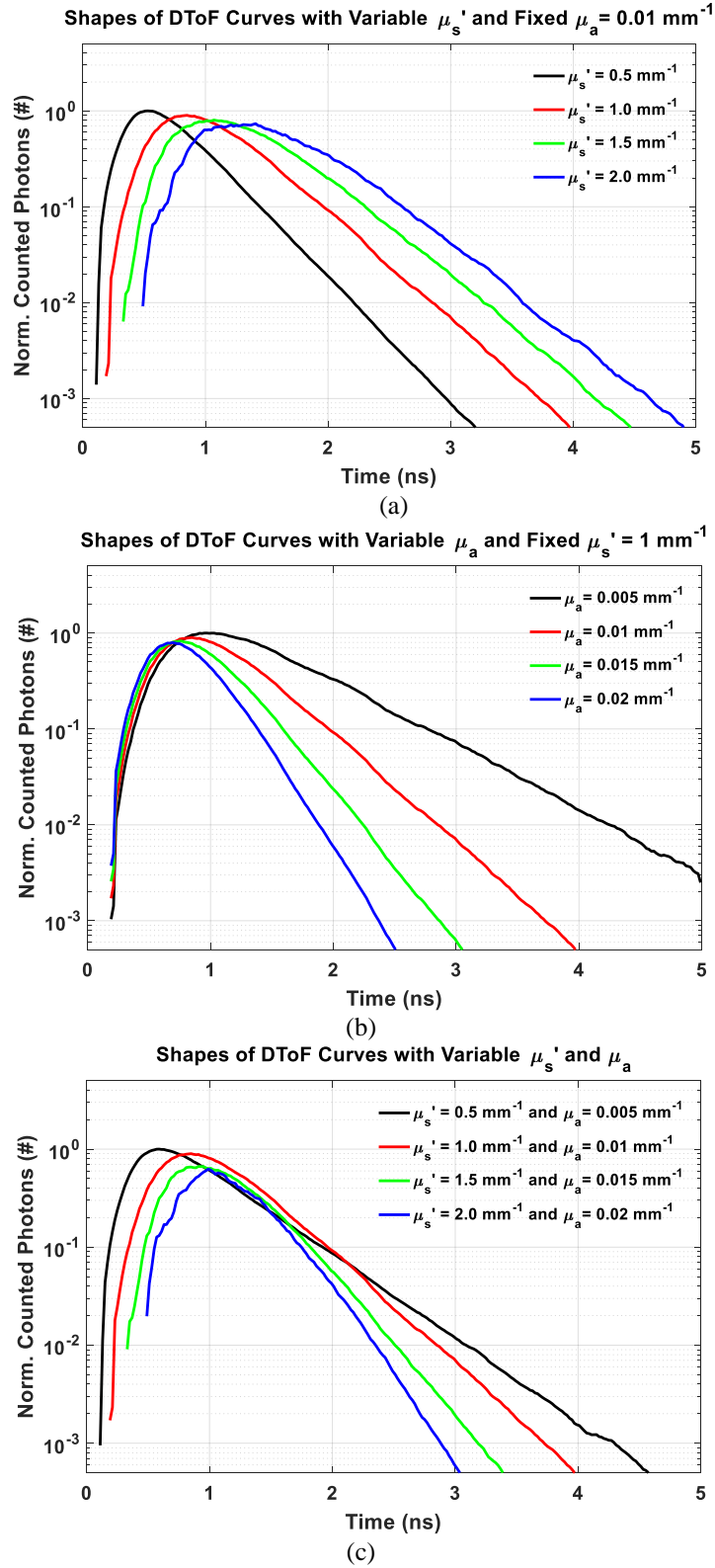


Figure 2-4: Shapes of DToF curves for a homogeneous turbid medium according to different OP and SDD = 3 cm. (a) Variable reduced scattering coefficients; (b) Variable absorption coefficients; and (c) Variable reduced scattering and absorption coefficients.

2.3.3. Photons Counting and Timing

Photon counting and timing equipment that have temporal resolution in the range of tens of picoseconds (ps) are required for TR-DOI prototypes, and two separate categories of equipment are used. The first is single photon counting detectors integrated with timing electronics such as TDCs or TCSPCs. The second category consists of standalone cameras such as streak cameras or time-gated intensified charge coupled device (ICCD) cameras [54] [62]. TR-DOI systems that use ICCD or streak cameras are very costly, complex to use and bulky in size, which restrict the wider use of TR-DOI [62]. Therefore, in this Chapter, we focus on the first category because of recent improvements that exploit the advances of semiconductor detectors based on silicon technology that are affordable and compact for TR-DOI systems.

Photon Counting

For TR-DOS measurements, it is important to have detection responses faster than one nanosecond (ns) as well as stable single electron responses for each detected event. Fast response is necessary because having faster detection time helps in better distinguishing between different arrival times for the counted photons so that the DToF can have a higher resolution. This helps in discriminating the differences in arrival times between detected photons due to the variation in path-length for each detected photon in the turbid media [16] [75]. Several detection technologies such as streak cameras [76] [77], time-gated ICCD cameras [59] [64], photomultiplier tubes (PMT) [62] [78], micro-channel plates (MCP-PMT) [31] [79], SPADs [80] [81], and very recently SiPMs [82] [83], can meet these requirements and they were already used in TR-DOI prototypes. These detectors can operate in the FR and TG modes except for traditional PMTs and SiPMs which work in the FR mode only [60] [84]. The benefits of the TG mode are noticeable when the reflectance geometry configuration of measurement, as shown in Figure 2-5, is used. Early photons in the pulse are related to photons that have passed through the superficial region of the turbid medium, whereas late photons are most likely to have reached deeper areas in the medium. These late photons provide useful information about the deep regions in turbid media [85]. Therefore, the TG-TR approach can be used to achieve short source-detector distance (SDD) up to null SDD in reflectance geometry and produce DToF histograms with

higher dynamic range [60]. In Figure 2-5, an illustration of the reachable depths versus delays of the detected photons (Figure 2-5 (a)), and a DToF histogram (Figure 2-5 (b)) were modeled using a **time-dependent diffusion equation (TD-DE)**, are shown. This simulation was done for a homogeneous turbid cube medium ($4 \times 4 \times 4 \text{ cm}^3$) that has a reduced scattering coefficient (μ_s'), absorption coefficient (μ_a) and refractive index (n) of 1 mm^{-1} , 0.01 mm^{-1} and 1.37, respectively [86].

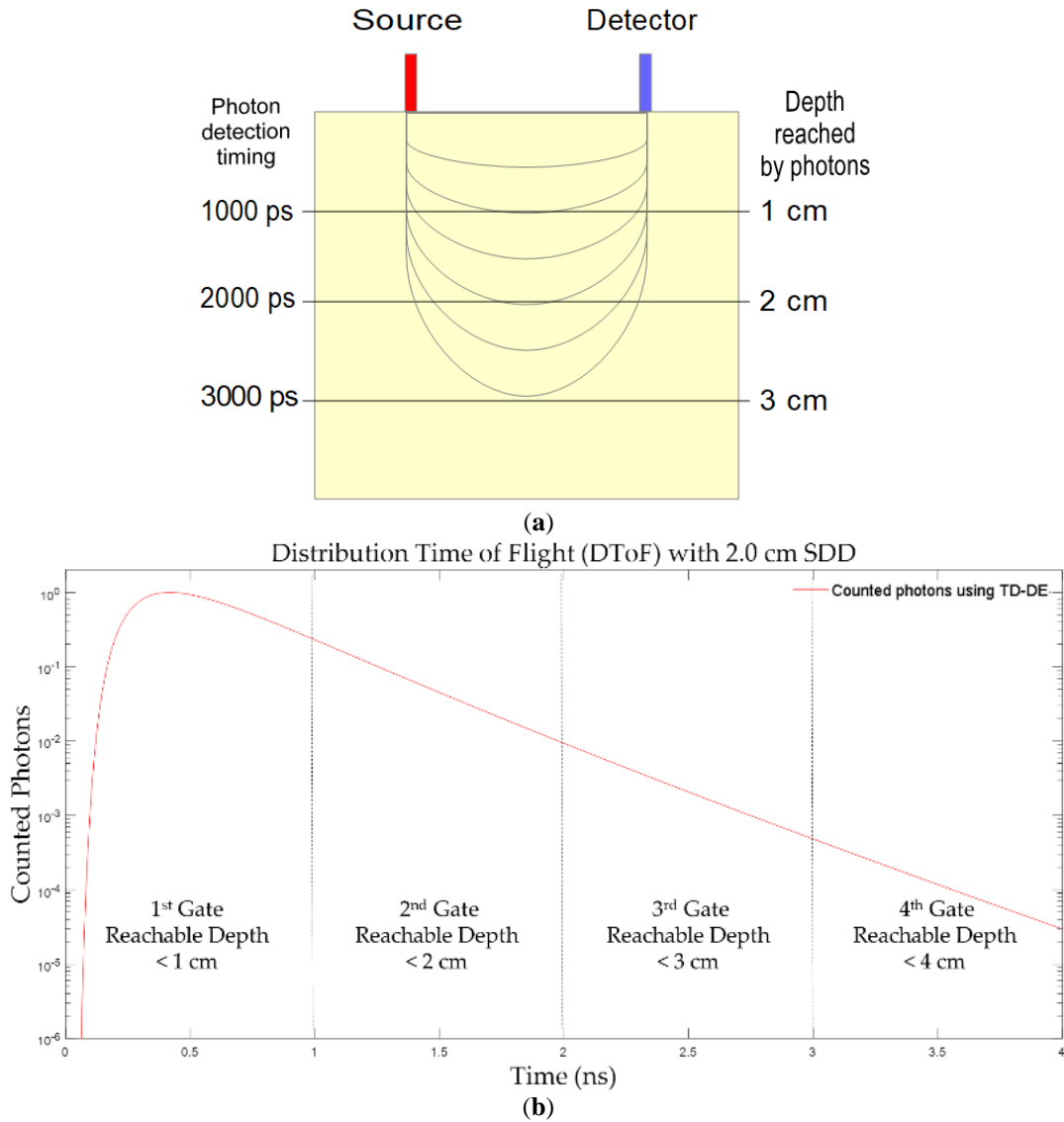


Figure 2-5: Photons reached areas within the turbid medium for each time gate window with different delays. (a) An illustration of increasing the reachable depths for photons detected at late gates. (b) The positions of gates on the DToF histogram and the possible reachable depth of detected photons during each gate.

An excellent way to distinguish between early and late photons is to use ultra-fast time gating circuits that can record the PTA for detected photons within several gates.

In recent years, several types of detectors were used for fast TG-TR-DOI prototypes, such as ICCDs [87] [30] and streak cameras [88]. However, these systems are limited by the large number of early photons, resulting in a significant increase in their noise and saturate the detectors [60] [84]. Also, ICCDs and streak cameras are not compatible with the trend of reducing cost and minimizing the size of TR-DOI systems. On the other hand, SPAD detection systems are a potential alternative when building fast TG detectors capable of rejecting early photons and detecting late photons within selected delays of picosecond resolution. The ultrafast transition time (≈ 200 ps) of turning the gate ON and OFF is one of the most useful features of TG-SPADs modules because it allows the SPADs to detect only the late photons without being saturated by the early photons [60]. This results in improved contrast and an increase in the number of detected photons within the selected gate windows. Thus, the **dynamic range (DR)** and **signal-to-noise ratio (SNR)** of the DToF will increase for TG-TR-DOS systems when compared to FR-TR-DOS [60]. The improvement of these factors will lead to significant advances in diffuse optical spectroscopy and imaging, particularly in detecting deep inclusions in turbid media such as blood clots in the brain. This will in turn lead to improved quality and contrast of reconstructed images. Also, using a close to null SDD allows the maximum level of the lateral spatial resolution to be reached in DOI for highly diffusive media such as tissues [60] [80] [89].

Photon Timing

The main output of TR-DOS measurement is a DToF histogram which is also called the **temporal point spread function (TPSF)** of detected photons that are generated using TCSPC modules or TDCs [58] [90] [91]. A DToF is a histogram of the different delay times between the time of triggering the synchronized injected laser pulse and the PTA of the detected photons belonging to the same pulse [92]. The width of time-channel should be short (<50 ps) to achieve a high temporal resolution [93]. TCSPC modules are superior to TDCs because of their reliability, high maximum count rate of photons (up to 10^7 photons s^{-1}), and short dead time (<100 ns) [94] [95]. However, integrating TDCs with SPADs or SiPM on one chip is a promising approach used in recent TR-DOI prototypes as opposed to using TCSPC modules which are costly [96] [97]. To acquire a DToF histogram, photons that have migrated through turbid media

are detected. For IRF measurements, photons directly from the source without involving a turbid medium are counted. Figure 2-6 illustrates the principle of TCSPC and TDC measurements, and how all detected photons are stored in the DToF histogram according to the differences in delay between each detected photon and the reference pulse (excitation rate of the laser’s pulses). The reference pulse can be connected to the TCSPC or TDC from the laser driver (gain switching case) or through the detected signal from a photodetector that measures the injected laser pulse. From the DToF histograms, the OP of a turbid medium can be determined.

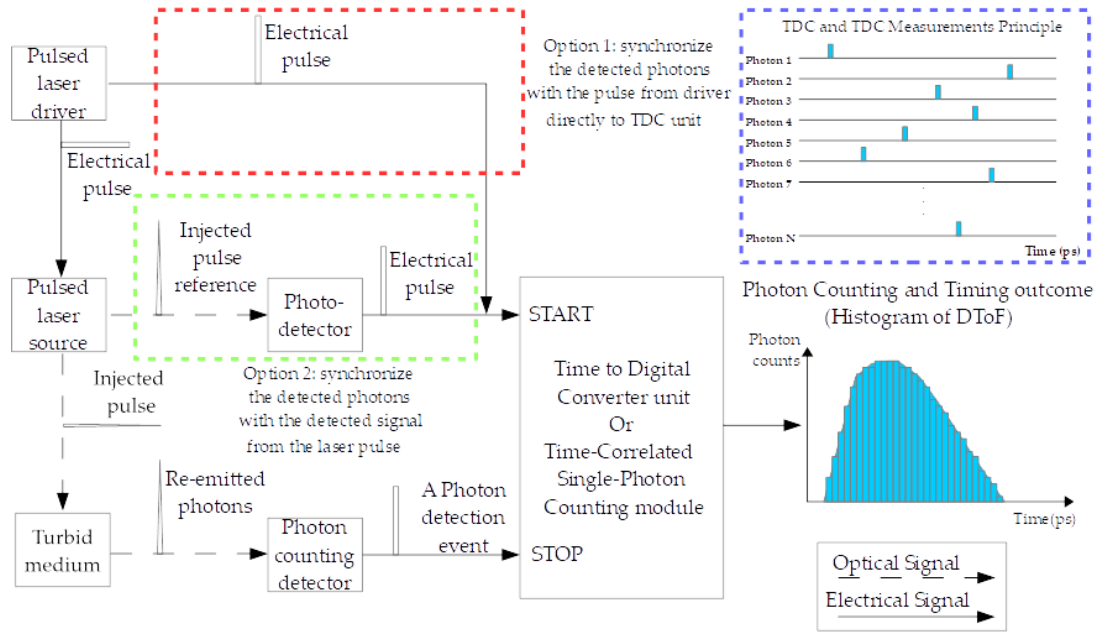


Figure 2-6: DToF histogram obtained by measuring the delay between the laser pulse and PTA. Top-left (in red and green borders) show two methods to synchronize the laser pulse with the detected photons. Top-right (blue border) illustrates how the counted photons are stored in the DToF histogram according to the differences in delay for each one of them.

2.3.4. Data Analysis Tools

The measured data from TR-DOS systems can be analyzed directly (spectroscopic approach) or analyzed using inverse problem solvers (imaging approach) to reconstruct 2D topographic images or 3D tomographic images [42]. Therefore, the OP of any turbid medium can be recovered by utilizing inverse problem models or some formulas of the analytical solution of the DE for several geometries [48] [98].

Spectroscopic Approach

The simplest method to retrieve the OP for a homogeneous object is to analyze the measured DToF [98]. For example, in the case of reflectance measurements for a semi-infinite high scattering homogeneous turbid medium, the OP of the turbid medium can be recovered by taking information from the logarithmic slope of a DToF's falling edge or tail [51] [99]. The absorption coefficient can be estimated from the linear regression of the slope of a DToF as follows (Figure 2-7) [51]. Then, the speed of the light in the medium (c'), the absorption coefficient (μ_a), time shift (t_{max}) between the peak of IRF_{Total} and DToF, and the distance between the optical fibers of source and detector (r) are substituted in the following formula to estimate the reduced scattering coefficient:

$$\mu'_s = \frac{1}{3r^2} (4\mu_a(c't_{max})^2 + 10c't_{max}) - \mu_a \quad (2.2)$$

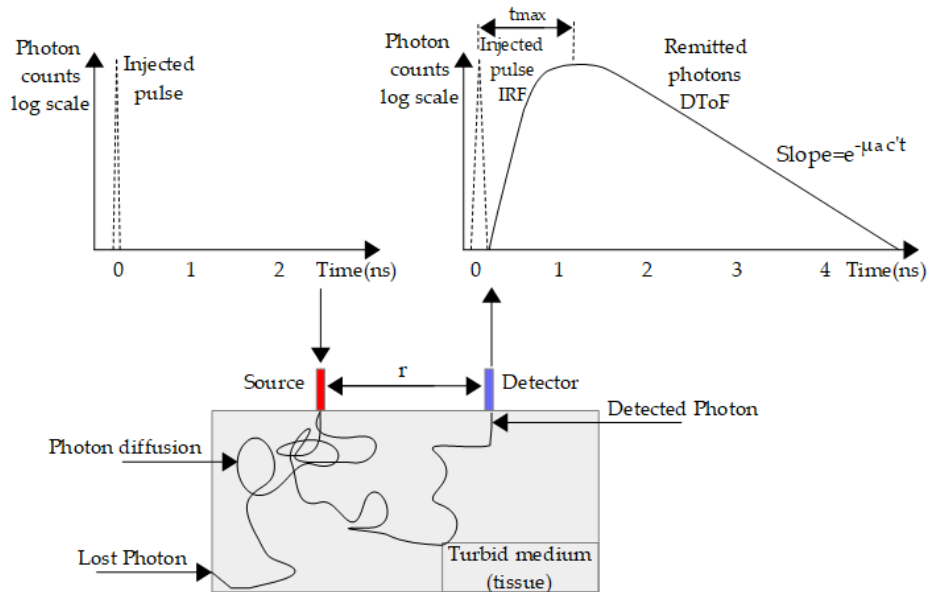


Figure 2-7: Recovering the optical properties of time-resolved DOS reflectance measurement for a homogeneous turbid medium.

This method can be applied to limited geometries of turbid media such as slab, infinite and semi-infinite [48]. Therefore, for complicated geometries and shapes of turbid media, a curve-fitting model (iterative forward modeling) can be used to analyze single point or multiple point measurements to recover the OP for homogeneous or multilayered turbid media, respectively [100]. This curve-fitting method can be applied to monitor fast changes of the OP in several applications such as functional brain or muscles monitoring.

Image Reconstruction Approaches

Images are reconstructed by estimating the OP of each point inside the turbid medium. Thus, the DOI prototypes should implement inverse modeling (in OT or DOT prototypes) to recover the OP and to detect and localize any inclusion. This is done by analyzing the measured signals from source-detector pairs on a turbid medium [31].

Optical Topography

Optical topography (OT) is a useful approach for functional brain or muscles monitoring due to its fast computation time to reconstruct 2D images for the required depths in the measured objects [39]. An OT system solves inverse problem to retrieve the OP at the region underneath each source-detector pair using the modified Beer-Lambert law [10]. Therefore, OT requires multichannel DOS systems (multiple source-detector pairs that measure the raw data simultaneously in reflectance geometry) to reconstruct a 2D image that represents the OP in many positions on the measured object [10]. This simultaneous measured data is essential to observe the changes in the OP over time due to the hemodynamic activities (happen within hundreds of millisecond to a few seconds) [101].

Diffuse Optical Tomography

In diffuse optical tomography (DOT) approach, 2D or 3D images can be reconstructed for the measured objects such as breasts and newborn heads [20]. For DOT prototypes, the measured data from a scanning or multichannel DOS system can be analyzed to obtain more information about the distribution of the OP in the object. 3D DOT is useful for some medical applications such as optical mammography, diagnosing intracranial hemorrhage and stroke in the brain, and follow up treatments for breast cancer [22]. In Figure 2-8, the iterative process of the forward modeling is shown. The iterative process continues until the deviation between measurements and the forward modeling solver for all detectors agree to within a small difference. This is done by comparing the measured data with the forward modeling solver to judge convergence, when reconstructing images for the distribution of the OP, is shown [10]. The forward modeling simulates the light propagation inside the high scattering medium by solving the RTE, or the simplified DE, using stochastic or numerical models such as Monte Carlo (MC) and the finite element method (FEM), respectively

[23] [86]. Using these iterative processes with all the data points of the DToF are computationally expensive. Therefore, some accelerated FEM approaches were recently demonstrated by analyzing a few critical points from the DToF curves for transmittance geometry measurements, instead of using all points on the DToF curves that are not needed. This approach significantly decreases the computation time for reconstructing 3D images [24] [102].

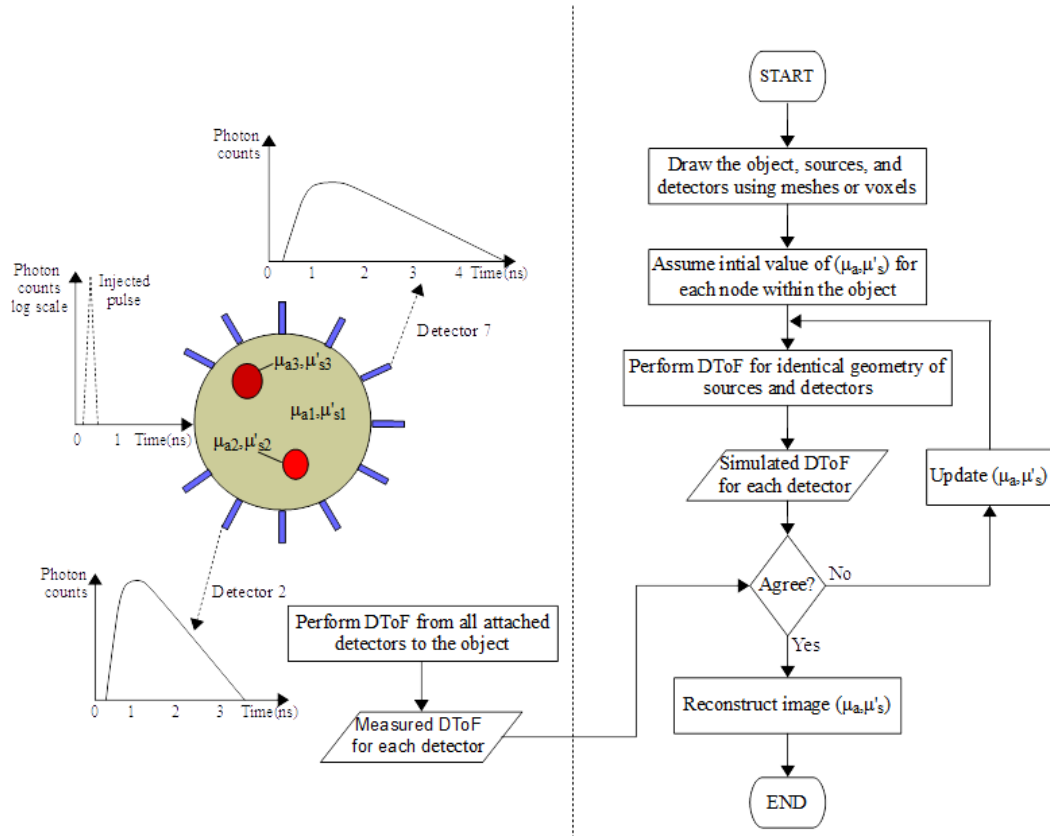


Figure 2-8: Flow diagram of a TR-DOT prototype, the left, and right side represent the measurement setup (DOS) and the flowchart of the inverse modeling, respectively.

Generally, inverse problem solving to reconstruct high-quality images requires prior knowledge of the anatomy of the tissue. However, because of the highly scattering nature of the turbid media, the solution of the inverse problem becomes ill-posed, nonlinear, and ill-conditioned [11] [43] [103]. Hence, if this anatomical information is considered in the inverse modeling, it is called a soft prior. It is called a hard prior if the anatomical information is also being considered in the forward modeling [10] [11]. Overall, many forward and inverse models were developed by several groups to study the light propagation and calculate DToF histograms using different geometries and

shapes of turbid media and to estimate the OP. Some review papers about modeling and image reconstruction for DOT and OT are recommended for more information [10] [11] [39] [104].

2.4. Performance Parameters of TR-DOS Systems

Several protocols such as “basic instrumental performance (BIP)” [105], “MEDPHOT” [106], and “nEUROpt” [107] were proposed to evaluate TR-DOS systems. BIP is a general protocol for evaluating the general features of TR-DOS prototypes without considering a turbid medium or the role of inverse modeling and the image reconstruction subsystem. BIP protocol was successfully applied to TR-DOI prototypes for functional brain imaging [57] [108]. On the other hand, “MEDPHOT” and “nEUROpt” are protocols for advanced evaluation which are mainly related to the recovery of the OP of homogeneous and heterogeneous turbid media, respectively. Parameters for MEDPHOT will be described when they are used in Chapter four. In this Chapter, the main parameters of the BIP protocol, and common figures-of-merit (FoMs) for photon counting detectors such as SPADs and SiPM will be described [105] [109]. These parameters will be described in the following subsections according to the order of the subsystems of TR-DOS prototype, shown in Figure 2-3.

2.4.1. Light Illumination Properties

Pulsed laser sources should be evaluated according to four parameters; the laser’s average power, spectral width, delivered power, and illuminated area [91]. The laser’s average power represents the generated energy per second. It can be calculated using the formula:

$$P_{AVG} = E_{cycle} * f, \quad (2.3)$$

where P_{AVG} (W) is the average power of a pulsed laser, E_{cycle} (J) is the released energy per the cycle of a pulse (e.g., length of a cycle is 100 ns at 10 MHz repetition rate), f is the repetition rate (number of pulses per second in Hz). Light of a laser source is emitted at a specific wavelength with a range of spectral width (e.g., 700 nm \pm 5 nm). Good laser sources have a narrow spectral width of a few nm from the center wavelength [105]. The delivered power (P_{Source}) is the average laser power that is delivered to the object. P_{Source} is the measured output optical power from the fiber optics that transmit

the light. P_{Source} can be measured using an optical power-meter or estimated by subtracting the attenuated power in fiber (P_{Atten}) from the average power P_{AVG} of the laser source.

$$P_{Source} = P_{AVG} - P_{Atten} \quad (2.4)$$

Lastly, the illuminated area A_{Source} represents the area of the injected light on the surface of the object. Increasing A_{Source} leads to a decrease of the spatial resolution for the reconstructed images from the measurement [91], So

$$A_{Source} \propto \frac{1}{Spatial\ Resolution} \quad (2.5)$$

2.4.2. Detection Features

Several features of photon timing in TR-DOI systems should be considered to evaluate the performance of prototype and particularly the detectors. In this Chapter, we focus on the characteristics of SPADs and SiPM detectors and consider a typical **figure-of-merit** of photon counting ($FoMC$) and **figure-of-merit** of photon timing ($FoMT$) to summarize the detectors' performance. These criteria apply to single pixel SPADs, SPADs array imagers and SiPM, and can be used to compare the detection performance in several application fields. The main parameters are the **photon detection efficiency** (PDE), noise, detection responsivity, dead-time (T_{DEAD}), timing jitter, fill-factor and total active area [109] [110]. PDE is a measure of the ratio of the number of detected photons to the number of incident photons in the active area of the SPADs or SiPM detectors [111] [112]:

$$PDE = \frac{Detected_{ph}}{Incident_{ph}} \quad (2.6)$$

The noise in SPADs represents false triggering that may or may not be correlated with time. **Dark count rate** (DCR) is the noise that is not correlated with the avalanche process for photon detection [113]. However, after-pulsing (P_{AP}) and crosstalk refer to subsequent noise pulses that appear after a detected photon is generated. P_{AP} happens within the same pixel that detected a photon, while crosstalk happens in external pixels [109] [113]. The DCR ranges between tens to thousands of counts per second for a typical SPAD pixel, whereas DCR ranges between tens of thousands to hundreds of thousands for SiPM detectors [81] [114]. The main sources of DCR in SPADs are the free-carriers because of the thermal generation that occurs in the depletion region [112]

[113]. Therefore, the total noise in SPADs and SiPM detectors increases with rising temperature [111] [112]. The real DCR is extracted from the measured DCR (DCR_M) using the following formula to eliminate the effects of T_{DEAD} of the TCSPC or TDC [113] [115] [116]:

$$DCR = \frac{DCR_M}{(1-DCR_M \times T_{DEAD})} \quad (2.7)$$

The effect of P_{AP} can be eliminated by applying an adjustable dead time T_{DEAD} which is adjusted based on an inverse relationship with P_{AP} :

$$T_{DEAD} \propto \frac{1}{P_{AP}} \quad (2.8)$$

However, long T_{DEAD} leads to a decrease of the feasible maximum count rate (Q_{MAX}) of the detector. Most of the parameters stated above affect the value of the FoM_C and the FoM_T [109] [111]:

$$FoM_C(m) = PDE \times \frac{\sqrt{Active\ Area}}{\sqrt{DCR}} \times \frac{1-P_{AP}}{T_{DEAD}} \quad (2.9)$$

$$FoM_T\left(\frac{m}{s}\right) = PDE \times \frac{\sqrt{Active\ Area}}{\sqrt{DCR}} \times \frac{1-P_{AP}}{T_{DEAD}} \times \frac{1}{FWHM} \quad (2.10)$$

Furthermore, detection responsivity (R_{Det}) is described by the ratio of detected photons that are transmitted through a slab which has a known $k_p(\lambda)$ transmittance factor [105].

$$R_{Det} = \frac{N_{Photons}}{T_{Meas} \times k_p(\lambda) \times P_{in}(\lambda)} \quad (2.11)$$

where $N_{photons}$, T_{Meas} , and $P_{in}(\lambda)$ represent the number of detected photons, the time of the measurements, and the optical power of the light delivered to the sample, respectively [91] [105].

2.4.3. Photon Timing Histogram

The time width of the channels in the histogram built using TCSPC or TDC must be stable and equal [91] [97]. To measure if the time widths of the channels are equal, the differential nonlinearity (ϵ_{DNL}) is used [105]. This nonlinearity is estimated using a continuous light source to illuminate the detector, and the TCSPC module to accumulate enough detected photons of $\geq 10^4$ photons per time-bin [105]. These photons are stored in channels (time-bins) based on the differences in the arrival time. Theoretically, the detected photons from a continuous light source should have equal counts for all time channels [91] [97] [105]. However, in practice, the width of channels

of the timing electronics suffers from instability, which leads to the difference of N_{ph} (the number of detected photons in each time-bin) [97] [105]. The ε_{DNL} can be calculated by comparing the difference between the highest $N_{ph,Max}$ and lowest $N_{ph,Min}$ photon counts and normalized by the mean counts using the following formula [91] [105]:

$$\varepsilon_{DNL} = \frac{N_{Ph,Max} - N_{Ph,Min}}{N_{Ph}} \quad (2.12)$$

Differential nonlinearity should be measured for the TR-DOS prototypes and ε_{DNL} should be maintained as low as possible [91] [105].

2.4.4. TR-DOS Systems

TR-DOS setups are evaluated based on the raw data produced by the prototype, mainly stability and FWHM of the IRF_{Total} and the DR of the DToF [16] [90]. Figure 2-9 shows how the measured DToF represents the convolution of the IRF_{Total} and the real DToF that is a histogram of the re-emitted photons from a turbid medium, plus the noise in the setup [91] [117].

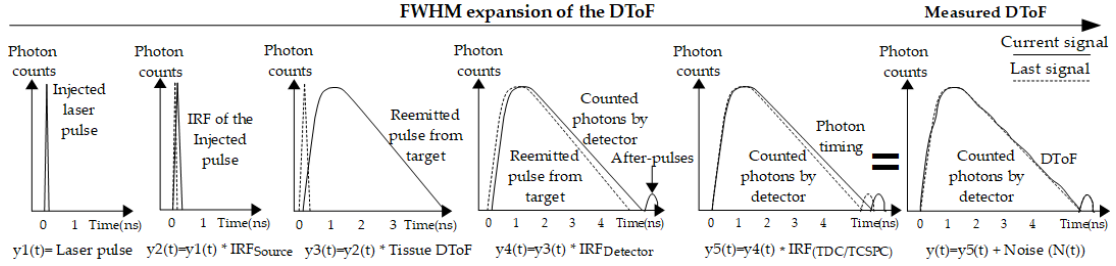


Figure 2-9: Broadening of measured DToF. Main contributions of the broadening are the time of flight of photons in a turbid medium, the noise of the setup and the IRF of laser source, detector, and TDC/TCSPC.

The Instrument Response Function (IRF_{Total})

The FWHM of IRF_{Total} is the square root of the sum of squares of the individual IRF resulting from each piece of equipment except the turbid medium of a TR-DOS prototype, and is given by [118]:

$$FWHM \text{ of } IRF_{Total} \approx \sqrt{IRF_{laser}^2 + IRF_{Detector}^2 + IRF_{OpFb}^2 + IRF_{TCSPC}^2} \quad (2.13)$$

Having a short and stable IRF_{Total} is required for TR-DOS systems [105] [119]. The IRF_{Total} of the setup is estimated by measuring the transmitted light from the laser

source to the detector when a thin, highly scattering material with small temporal dispersion, such as a white sheet of paper or a Teflon layer, is inserted between the source and detector [82] [120] [121]. Using a thin and highly scattering material between laser source and detector ensures that the detected photons are diffuse and have multiple directions when they impinge the detector. This is similar to the re-emitted photons from a turbid medium [120]. With this setup, the IRF_{Total} can be determined from the FWHM of the measured pulse. All sources of noise such as P_{AP} and DCR should be estimated separately for the setup, and they must be reduced to achieve a high dynamic range (DR) for the IRF_{Total} and DToF histograms. Also, the width of IRF_{Total} needs to be as short as possible because it may distort the accuracy of TR-DOS measurements when it exceeds one ns [75] [120].

Dynamic Range (DR)

The dynamic range (DR) represents the ratio of the maximum detectable signal Sig_{Max} to the minimum detectable signal Sig_{Min} [109]. A high DR is desirable for any TR-DOI prototype. The DR is calculated using:

$$DR = \frac{Sig_{Max}}{Sig_{Min}}. \quad (2.14)$$

Having a high DR is important for TR-DOS systems, especially when small SDDs are used in reflectance geometry. TR-DOS systems with more than three orders of magnitude (10^3) of DR are required to be appropriate for applications that require very deep detection capabilities such as functional brain monitoring for adults' heads [60].

2.4.5. TR-DOI Systems

MEDPHOT [106], and the nEUROPt [107] [122], protocols include several parameters to evaluate DOS and DOI prototypes according to their ability to recover the OP of turbid media. The MEDPHOT protocol focuses on the accuracy and linearity of the OP quantification for homogeneous turbid media. The nEUROPt protocol evaluates the depth sensitivity of the prototypes and their ability to detect inclusions in deep regions of a turbid medium and the accuracy of the OP quantification for two-layered turbid media such as a human's head. Also, the parameters of nEUROPt evaluate how good is the estimation of the size of inclusion, and the depth and lateral localization versus the actual OP distribution in a heterogeneous turbid medium [107]

[122]. In this thesis, parameters from BIP and MEDPHOT protocols will be clarified with more details later (in Chapter 4) when the performance of the integrated FR-TR-DOS prototype is evaluated.

2.5. TR-DOS using SPAD and SiPM

Single-photon counting detectors are used to generate an electrical signal for each photon that is absorbed [123] [124] [125]. PMTs were the most commonly used detectors in photon counting and timing systems for low light such as TR-DOS [126] [18] [127] [128] [31]. The use of SPAD detectors has recently increased because they possess several advantages over PMTs: low *DCR*, high quantum efficiency (QE), timing jitter less than 200 picoseconds, small size, low power dissipation, low supply voltage, high reliability, and ultrafast gating [129]. However, there are also some limitations of SPAD detectors such as small detection area (active area) and low *PDE* in the NIR range [130]. SPADs in standard complementary metal-oxide-semiconductor (CMOS) silicon technology typically have lower sensitivity to photons of wavelengths longer than the visible range (400–700 nm). This is due to the low absorption coefficient and the longer absorption depth of silicon relative to other semiconductor materials as shown in Figure 2-10 [131] [132].

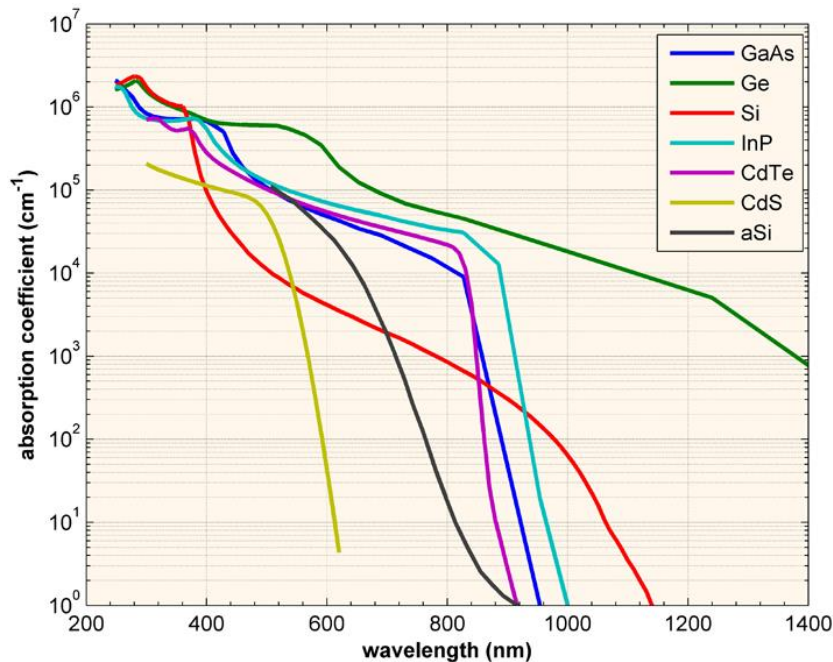


Figure 2-10: Comparison of the Absorption coefficients for some semiconductor materials over the wavelengths range of visible and NIR light [132].

Therefore, SPADs fabricated using standard silicon CMOS technologies and operating in the NIR range cannot achieve high PDE and PDE levels are usually less than 20% [112] [129] [133]. However, the PDE of SPADs is generally higher than PMTs in the NIR range [133].

2.5.1. SPADs

A SPAD detector typically consists of a pn junction that is reverse-biased with a voltage that exceeds its breakdown voltage V_{BD} [112] [134]. In Geiger-mode, a large current is created in the depletion layer from one or more free charges, for example, from “dark current” charges or photogenerated electron-hole pairs. This leads to self-sustaining avalanche multiplication events that increase the current to the milliamp range with sub-ns to few ns rise time [111] [135]. The avalanche current flows into the junction until the quenching circuit lowers the bias voltage to below the V_{BD} . Biasing of the SPADs is done by waiting for the adjusted T_{DEAD} (also known as hold-off time) after each pulse to eliminate the P_{AP} effect. Then, the SPADs is reset and ready for triggering again in the Geiger mode by a new photon. The length of T_{DEAD} varies from tens of ns to a few μ s, which is essential to be as short as possible to increase the sensitivity and to maximize the photon counts of the SPADs, particularly in the NIR range [123]. Because of the low absorption coefficient of silicon in the NIR range, a thicker depletion region is needed to increase the detection efficiency of the SPADs. However, timing jitter in the detector increases for thicker depletion regions. Therefore, there is a trade-off in this issue for TR-DOS measurements because they require very short timing jitter (< 500 ps) and an acceptable level of PDE [123]. Consequently, many of the reported schemes and designs of SPADs focus mainly on reducing the T_{DEAD} , timing jitter ($IRF_{Detector}$), and noise sources such as DCR and P_{AP} [109].

SPADs Categories

SPAD detectors can be categorized into two types based on their implementation technology: standard CMOS silicon technology and custom silicon technology [112] [113]. Several research groups implemented many custom-designed SPADs based on CMOS technology for a variety of visible wavelength applications such as fluorescence lifetime imaging (FLIM) and Raman spectroscopy [125] [136]. In general, SPAD detectors are fabricated in standard CMOS technology based on a thin depletion region

(1–2 μm). The main limitations of CMOS SPADs are modest PDEs especially in the NIR range [135] [137], worse timing resolution [138], higher DCR per unit area [139] [140] and more P_{AP} in comparison with SPADs fabricated using custom silicon technology. The timing jitter (IRF_{SPAD}) can be as short as 30 ps for CMOS and custom technology [109]. Note that the timing jitter for SPADs increases to > 100 ps when the diameter of the detection area reaches 100 μm or larger in CMOS, whereas 35 ps timing jitter was demonstrated for 200 μm diameter SPADs based on custom silicon technology [113] [141] [142].

Figure 2-11 shows that it is desirable to enhance the PDE without increasing the IRF_{SPAD} to more than a few hundred ps for picosecond photon-timing applications such as TR-DOS. For example, a popular custom silicon technology, SPADs SPCM, produced by Excelitas Technologies has high PDE ($>50\%$ in 600 to 800 nm), but it was rarely used in TR-DOS prototypes because of its large FWHM of IRF_{SPAD} (350 ps) as a result of having a thick depletion layer (20–25 μm) [143] [144]. Although custom silicon technology is a potential approach to optimizing SPADs characteristics and minimizing the limitations, standard CMOS is a superior option for TR-DOS system regarding size, cost, and compactness with having TDCs on the same SPADs chip [97] [130].

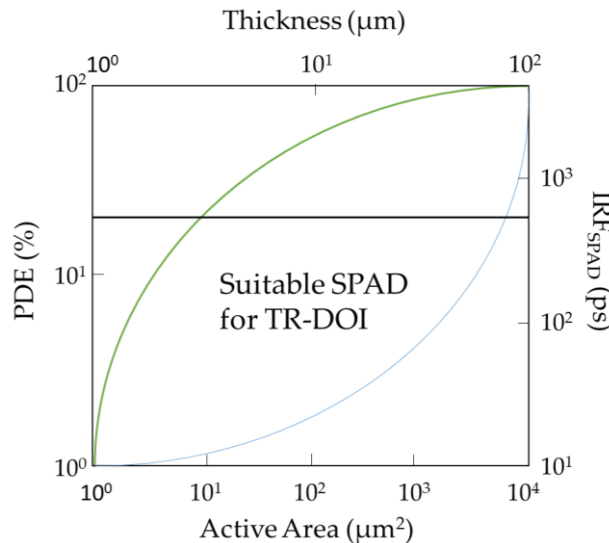


Figure 2-11: Compromise of SPAD: blue and green curves represent the IRF_{SPAD} and the PDE changes with increasing thickness of depletion layer and the size of the active area respectively, whereas the black line indicates the maximum acceptable IRF_{SPAD} .

Most reported TR-DOS prototypes were implemented with SPADs based on the front-side illumination (FSI), although a backside-illuminated (BSI) CMOS SPADs based prototype was reported [25].

2.5.2. SiPMs

A SiPM is an array of hundreds or thousands of SPADs pixels connected in parallel, and function as a single large area detector (few mm²) with two terminals (one cathode, another anode) [121] [145]. The total area of the SiPM can be estimated by multiplying the number of pixels by the fill-factor (FF) for each pixel [109]. When each SPAD pixel connects to one passive quenching circuit, it is called an analog SiPM. If an active quenching circuit is connected to each pixel, this is a digital SiPM [109] [146]. In analog SiPMs, the number of photons can be estimated from the output current that represents a summation of all photons that are absorbed [109]. However, each single SPAD pixel in digital SiPM is connected to a circuit to generate a signal for each counted photon, and a quenching circuit to turn off the SPADs when it exceeds the maximum time of activity [146] [147]. Presently, most commercially available SiPMs cannot reach high enough resolutions to perform single photon counting with high temporal resolution in 100 ps range without a custom module integrated with the SiPMs detector to extract the timing information for each photon, as demonstrated in [115]. Overall, SiPMs combine the benefits of both photocathode-based (e.g., PMTs) and solid-state detectors such as large active detection area (few mm²), affordability, simplicity, compactness, high quantum efficiency in the NIR, low bias voltage, and non-sensitivity to the magnetic field. However, SiPMs detectors suffer from a limited dynamic range of around two orders of magnitude (10^2) and a long diffusion tail because of the sequence of carriers generated inside the detector for each single photon response [82].

2.5.3. SPADs Operation modes

SPAD detectors can be classified into two categories based on their operation mode: free-running (time-invariant) or time-gated (time-variant) [148]. Free-running SPAD detectors are ready to count any incident photon on the active area, but they are kept off only during an adjustable T_{DEAD} after each photon counting process to reduce

the P_{AP} effect [149] [150]. However, TG SPADs are completely blind to photons impinging on the active area when the gate is turned OFF. Photons can only be detected if they arrive while the gate is ON [151]. That is, FR SPADs are always biased above the V_{BD} to stay ready to count impinging photons, whereas TG SPADs are periodically biased above the V_{BD} to detect impinging photons only within a very short, precise, and synchronized time gate window [150] [151]. Figure 2-12 illustrates the main differences between photon counting in FR and TG detectors (photons with blue colored symbols), reasons for losing photons (photons with green colored symbols) in FR and (photons with green and red colored symbols) in TG, and the importance of T_{DEAD} to reduce the effects of false triggering, particularly P_{AP} . Later in this Section, the major differences between FR and TG TR-DOS systems will be described.

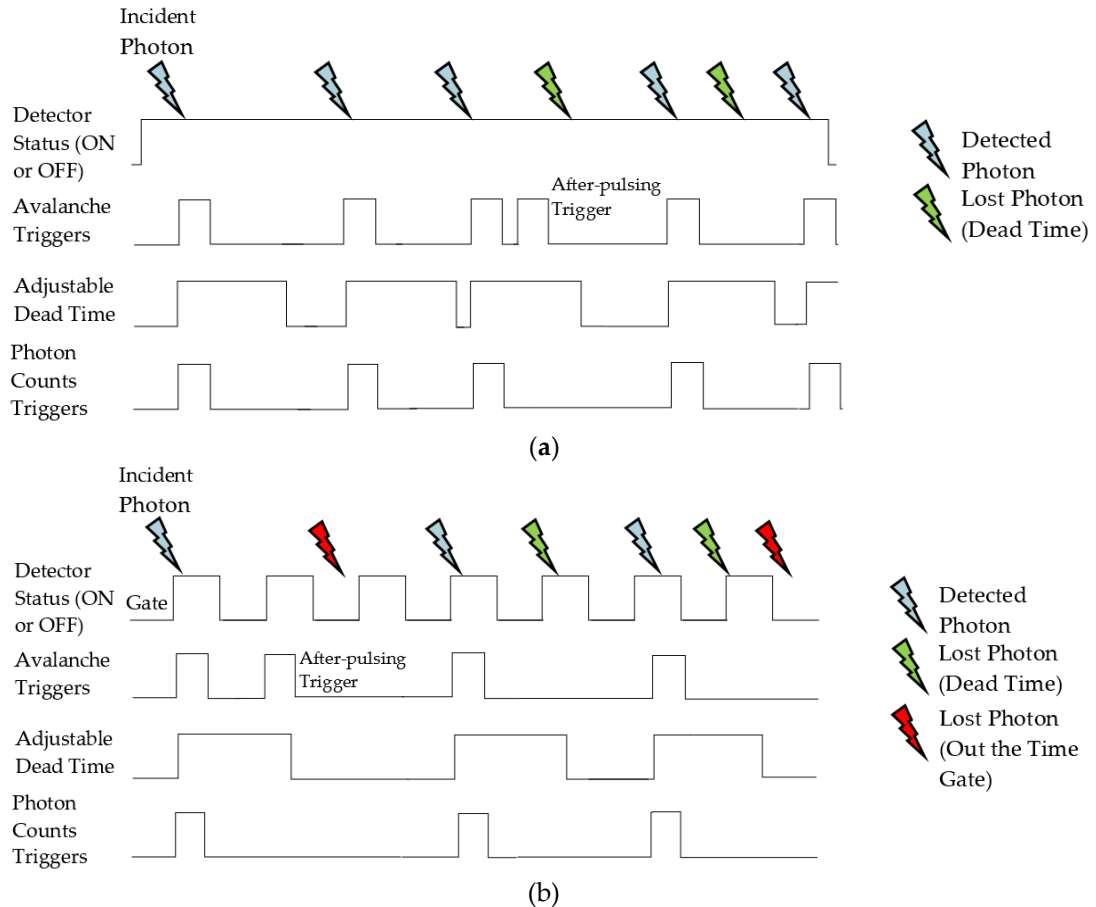


Figure 2-12: Photon counting process for identical incident photons using (a) FR detector, (b) TG detector. Reasons for missing photons are indicated on the right for each operation mode.

2.5.4. Features of the Detectors

In literature, several reported TR-DOS prototypes were built using seven SPADs or SiPMs detectors. Five of these detectors were SPADs [152] [141] [153] [130] [154], and two were SiPMs [155] [156]. Three of these detectors are state-of-the-art (PDM series) SPADs modules with three sizes of active area (diameters 50, 100, 200 μm) fabricated in custom silicon technology by Micro Photon Devices (MPD, Bolzano, Italy) [152] [141] [153]. Table 2.1 shows a summary of the features of the SPAD and SiPM detectors that have been used to build TR-DOS prototypes [25].

Table 2.1: Main features of SPADs and SiPM detectors used in TR-DOS prototypes.

Detector Type	Front-Side Illuminated SPAD				Backside-Illuminated SPAD	Excelitas-SiPM C30742-11-050-T1	Hamamatsu S10362-11-050C
Fabrication Technology	Custom (Planar) silicon			HV 0.35 μm CMOS	3D 130 nm CMOS	NA	NA
Operation Mode(s)	Free-Running and Time-Gated			Free-Running	Free-Running	Free-Running	Free-Running
No. of Pixels	1	1	1	128 \times 128	2 Arrays (1 \times 400)	400	400
Dimension of Pixel(s)	50 μm diameter	100 μm diameter	200 μm diameter	3.2 \times 3.2 mm^2	11 \times 11 μm^2 per pixel	50 \times 50 μm^2 per pixel	50 \times 50 μm^2 per pixel
Total Active Area	(1.963 \times 10 ³ μm^2)	(7.854 \times 10 ³ μm^2)	(3.1416 \times 10 ⁴ μm^2)	0.6144 mm^2	28 μm^2 per pixel	1 mm^2	1 mm^2
Time-Jitter (ps)	30	31	35	NA	260	100	<300
DCR (cps) @ Room-Temp.	2 k	5 k	60 k	NA	35,000	100 K	400 K
Dead Time (ns)	77	77	80	100	NA	NA	NA
Max. Count Rate (Mcps)	13	13	13	0.1	NA	27.6	NA
P _{AP} (%)	1	1	2	NA	NA	NA	NA
FoM _T Timing (m/s)	NA	3400 k	NA	NA	NA	152 k	NA

2.5.5. FR vs. TG TR-DOS

The major difference between FR and TG TR-DOS systems is the necessity to synchronize the time gate windows with the PTA of the re-emitted photons from the turbid medium [60]. Therefore, TG-TR-DOS systems require a common pulse generation unit to synchronize the laser pulses and time gate windows. In addition, a delay unit is required in TG-TR-DOS systems to adjust the delay of the gate and enable the detection of only on early or late re-emitted photons [60]. Nevertheless, FR-TR-DOS systems are simpler than TG because the driver (internally) triggers the laser pulse source according to the adjustable repetition rate in the range of one to tens of (MHz). Also, the detector is always ON and able to count incident photons unless a photon

arrives during the T_{DEAD} . Figure 2-13 shows the differences between the typical components of FR and TG-TR-DOS systems using SPAD detectors.

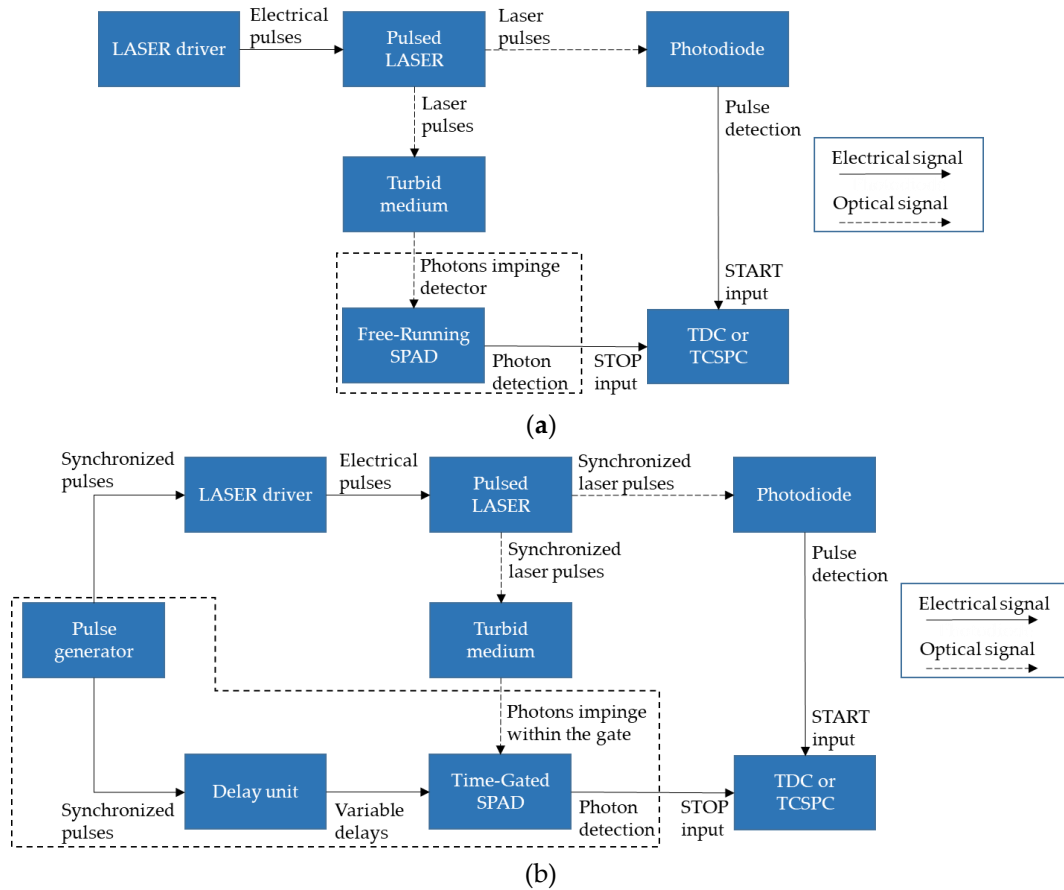


Figure 2-13: Components of TR-DOS prototypes using (a) FR Detector, (b) TG Detector.

2.6. Discussions and Research Challenges

At present, TR-DOS systems that were previously complex, bulky, and costly are being simpler, smaller and more affordable because of massive developments in photon timing and counting, and picosecond pulsed light source technologies. The cost and size have been reduced by more than two orders of magnitude, particularly for photon timing and counting. For example, ICCDs and streak cameras cost more than tens of thousands of US \$, whereas SPADs, SiPMs, and TDCs only cost hundreds of US \$ or less (see Figure 1-3). In this Section, several issues, challenges, and advances of the prospective TR-DOS systems are described.

Silicon detectors for photon counting and timing can be designed with several desirable performance features such as large total active area, good PDE in the NIR

range, short $IRF_{Detector}$ (tens of ps range), high dynamic range, low noise sources (P_{AP} , crosstalk, DCR and memory effect), high count rate, and short T_{DEAD} . However, trade-offs play an essential role in achieving desirable characteristics, since improving one performance feature usually leads to degrading another feature. Several examples are now given.

1. A large active area is one of the most desirable features for detectors to increase the number of impinging photons, and subsequently increase the number of detected photons. However, noise and IRF_{SPAD} increase greatly with larger active area for each SPAD pixel. Therefore, the active area can be enlarged by using arrays of pixels for SPAD detectors or SiPM detectors. Incorporating a dedicated TDC for each pixel increases the noise and reduces the FF which minimizes the total active area of the detector. To avoid this limitation, each TDC could be shared by multiple pixels to increase the FF of pixels, and subsequently, enlarge the total active area. However, when more pixels share one TDC, the acquisition time becomes longer [154].
2. A high PDE in the NIR range can be achieved by increasing the thickness of the depletion layer, and two approaches were demonstrated. The first being the use of a thick front-side illuminated detector and the other being the use of a thick back-side illuminated detector [130] [143]. However, the maximum thickness of the detectors is restricted by the increase of noise and $IRF_{Detector}$ when the thickness is increased. When $IRF_{Detector}$ exceeds a few hundreds of ps, the detectors compatibility with TR-DOS systems is compromised.
3. Timing jitter ($IRF_{Detector}$) can be enhanced by minimizing the active area and the thickness of the depletion layer. However, this results in the lowering of PDE and SNR because photons will transmit for short distances inside the depletion region in the detector, which reduces the probability of detection.
4. Dynamic Range (DR) can be improved by using TG instead of FR SPADs, but the IRF_{Total} of the TG-TR-DOS systems are usually wider than FR-TR-DOI systems. However, the design of fast-gating SPADs requires high-efficiency quenching circuits to ensure the fast transition time (range from a few tens of ps up to a few hundreds of ps) for the rising edge of the window.

5. To have low noise, reducing the contribution of sources of noise such as (P_{AP} , crosstalk, DCR , and memory effect in TG measurements) is required. Selecting a proper T_{DEAD} can eliminate the effects of P_{AP} , but the maximum count rate will be degraded considerably if T_{DEAD} is longer than necessary [150]. Avoiding large active area of pixels and monitoring the temperature of the detector are the best methods to reduce the contribution of DCR to the total noise in the measurements. In TG measurements, a new source of background noise, called the memory effect, appears as a result of the huge number of early photons that hit the active area of the SPADs while it is in the OFF state [157]. Therefore, zero SDD is not preferred because it increases the memory effect and subsequently reduces the SNR for late photons.

Conventional TCSPC devices are not compatible with the ongoing trend of minimizing size and reducing the cost for each detection channel in a TR-DOS system. Therefore, using a TDC is a good alternative to meet the small size and low-cost requirements, and leads to the possibility of building TR-DOS systems with dense source-detector pairs. Some challenges were highlighted regarding TDC design and particularly with incorporating TDCs and detectors on the same chip [21]. The lack of a general FoM for TDC designs to evaluate the validity of a specific application obstructs the performance comparisons between different architectures of TDCs [158]. Also, the absence of a proper method of modeling TDCs hinders researchers in the design of custom TDCs. Because a modeling method does not exist, researchers must design, fabricate, and test TDCs before determining whether the TDCs will be compatible with their specific TR-DOS systems.

TR-DOI prototypes usually suffer from some limitations that require more research work.

1. The inverse problems for the DE of diffused light are ill-posed, and there is no unique solution to them. No standard inverse problem modeling and image reconstruction tools are available yet. Therefore, a full custom-made analysis of DToF curves is needed for each built prototype to interpret the raw data (DToF curves) and recover the OP of the turbid medium. However, advanced features of the prototypes such as image reconstructions, localization of inclusions, and

- accurate recovery of the OP are time-consuming processes in 3D tomographic imaging if all points in the DTOF curves are used in the inverse problem-solving.
2. 3D Image reconstruction using only a few points of the DToF for measurements in reflectance and transmittance geometry could reduce the time of processing significantly. Parallel computation tools such as **graphics processing units (GPU)** can be exploited to generate DToF curves at multiple detection points during the iterative forward problem solver and to reconstruct several slices in DOT in parallel to reconstruct 3D images. However, for each slice, the inverse problem must be solved in series. To date, a fast forward problem model that uses a GPU is available, and the approach of using only a few points was validated in simulation for transmittance measurements only [86] [102] [24]. Therefore, the integration of these two approaches would lead to the reconstruction of images at a much faster speed (within tens to hundreds of seconds).
 3. Focusing on the most useful parts of DToF curves in reflectance geometry was proven to be an effective method in recovering the OP and detecting inclusions at different depths. Developing TG detectors that can collect re-emitted photons during multiple gate-windows (with flexible size and delays between the gates) simultaneously is a powerful approach which was demonstrated and reported for dual-gate measurements [159]. The timing of detected photons during the two gates was achieved using a commercial TCSPC module, and custom-made timing electronics and their performance were proven to be similar [159]. Therefore, the benefits of using a dual window (or more) and replacing expensive TCSPC modules needs further investigation.
 4. The detection of multiple inclusions at different depths using reflectance geometry measurements is a known limitation for TR-DOI systems. This limitation appears when there are more than one inclusion within the depth sensitivity range because the shallower inclusion usually makes it difficult for the inverse problem solver to detect the deeper inclusion. More sophisticated inverse problem solvers are required for TR-DOI systems to enable the detection of all inclusions without being distracted by shallow inclusions.

2.7. Conclusions

In this Chapter, we discussed how silicon solid-state detectors have contributed to developing the field of TR-DOS and DOI into a new era of affordability, portability, and compactness. In Section 2.1, the physical principles of diffuse optical spectroscopy in the biological window (600–950 nm) were introduced, and the TR-DOS systems were categorized based on geometry and methods of illumination and detection. Theory of diffuse optics was described briefly in Section 2.2. The main components of TR-DOI prototypes were described in Section 2.3. Parameters for the evaluation of the equipment and the entire prototype were stated in Section 2.4. The advantages and limitations of TR-DOI prototypes were specified, and the main features of the designing of SPADs that overcome the low detection efficiency of silicon in the range of red and near-infrared light (600–950 nm) are stated in Section 2.5. Moreover, the differences between FR and TG detection of photons, and FR vs. TG TR-DOS systems were mentioned in Section 2.5. The rising popularity of SPADs based TR-DOS systems as a result of the promising advances in SPADs technology are discussed, specifically the distinctive capabilities of the ultrafast time-gating SPADs in comparison with traditional FR measurements. The limitations and challenges and the expected future developments according to each component in TR-DOI prototypes were discussed in Section 2.6.

In general, FR-TR-DOI would mainly benefit from the recent and ongoing developments of low-cost SiPM detectors and arrays of SPADs which have a large total active area, and particularly when TDC units are integrated on the same chip as the detector. This can lead to building multichannel FR-TR-DOS prototypes that are portable, compact, and easy to use for several applications with fast data acquisition time. These FR-TR-DOS systems can have very good performance for transmittance geometry measurements for functional brain and muscles monitoring, and optical mammography.

On the other hand, developing on-chip array of TG CMOS SPADs would help in realizing low cost, compact, multichannel TG-TR-DOS portable prototypes for reflectance geometry measurements. These prototypes are expected to have high performance in depth sensitivity, depth selection, and spatial resolution, particularly for

the imaging of multilayered turbid media such as functional brain monitoring for neonates and adults.

Based on the discussion (in Section 2.6) of the recent development of equipment that can be utilized for TR-DOI prototypes, it is noticeable that the main drawbacks of traditional TR-DOI systems (such as size, cost, and complexity) are being eliminated. New generations of TR-DOI prototypes will mainly utilize affordable equipment for light illumination, photon counting and timing, and more accurate and computationally efficient image reconstruction tools. This will lead to spreading the uses of the new generation of TR-DOI prototypes in imaging applications over the next few years.

Chapter 3

INTEGRATION AND EVALUATION FOR A COMPUTATIONALLY EFFICIENT TIME- RESOLVED DIFFUSE OPTICAL TOMOGRAPHY SYSTEM²

In this Chapter, a computationally efficient time-resolved diffuse optical tomography (TR-DOT) prototype will be demonstrated. This TR-DOT prototype used an accelerated inverse problem solver to reconstruct high quality 3D images of highly scattering media such as tissues. The inverse problem solver used seven well-defined points on each experimentally recorded histogram of the DToF. The accuracy of the recovered OP and the computational load and time of TR-DOT prototype were investigated using cylindrical turbid phantoms. These phantoms were measured using transmittance geometry in multiple experiments to evaluate the performance of the prototype. The results of the evaluation are important for the realization of a real-time and highly accurate TR-DOT system for diffuse optical imaging applications such as detecting cancer tumor in the breast or diagnosing blood clots in the brain.

3.1. Introduction

Diffuse optical tomography (DOT) is an emerging noninvasive imaging technology that can be used to reconstruct 2D or 3D images (OP distribution) of turbid

² Most of this chapter was published as: Alayed, M., Naser, M.A., Aden-Ali, I. and Deen, M.J., 2018. Time-resolved diffuse optical tomography system using an accelerated inverse problem solver. *Optics Express*, 26(2), pp.963-979.

media such as biological tissues [10] [160] [161]. DOT exploits the particle nature of light (photons) in the biological window of 600 nm to 950 nm where light scattering dominates absorption to explore the chemical composition of tissues of up to a few cm in depth [10] [17]. Conversely, other optical tomography modalities such as optical coherence tomography (OCT) are utilized to explore shallow regions (1 - 3 mm depth) of the turbid media by exploiting the wave nature of the light [10] [51]. Therefore, in DOT, light loses its wave-like nature, and photons diffuse within turbid media thicker than 1 cm according to the radiative transfer equation (RTE) [10] [16] [160]. Because of the complexity of the RTE, its simplified approximation, the diffusion equation (DE), is more commonly used to simulate light propagation (forward problem modeling) and to reconstruct 3D tomographic images by recovering the optical properties (OP) distributions (inverse problem solver) of turbid media [48] [43] [104].

Reconstructing 3D images for some organs such as newborn heads or women breasts are useful to detect and localize inclusions such as cancer tumor or blood clots. However, this inverse problem is ill-conditioned, ill-posed and non-linear [8] [11] [12] [162]. The inverse problem can be simplified (linearized) and solved in one-step computation, but with a penalty of the low quality of the reconstructed 3D images [10]. Therefore, it is required to solve the nonlinear inverse problem iteratively to improve the quality of the reconstructed 3D tomographic images, but this is a time-consuming process [10] [12].

For DOT systems, prior knowledge of the structure (particularly hard prior) plays a significant role in improving the reconstructed 3D images of the turbid media because it limits the number of unknowns when estimating the OP [10] [12] [20]. Therefore, using prior knowledge leads to a reduction in the under-determination of the inverse problem [11] [162]. Prior knowledge is classified into two types based on the method of the minimization process — hard prior and soft prior [10] [11] [162]. In the hard prior approach, the turbid media can be segmented (using meshes or voxels) into several homogeneous regions where all nodes within a region have the same OP [10] [161] [162]. Therefore, the number of unknowns is reduced drastically to be the number of regions in the turbid medium instead of the total number of nodes that lead to significant reduction of the computation time for the iterative inverse problem-solving.

On the other hand, prior knowledge is called soft prior when the number of unknown nodes is preserved, whereas the structural information is incorporated into the regularization term [10] [11] [162]. Moreover, the anatomical information of any organ can be extracted from another imaging modality such as **magnetic resonance imaging** (MRI) or **computed tomography** (CT) [42] [162].

In DOT, the TR approach is known for its superiority over other approaches of DOT such as CW and FD (see Table 1.1) [10]. This is because the TR approach can be used to accurately quantify the values of the OP (μ_s' and μ_a) separately, and to reconstruct the highest quality images of the OP distribution within the turbid medium [10] [21]. However, the inverse problem solvers suffer from costly computations of a large amount of raw data that is generated by TR-DOT prototypes [10]. Therefore, for functional monitoring, reconstructing 2D images or analyzing spectroscopic measurements are usually used due to the need for real-time results.

During the last few decades, the issue of having a huge amount of data when using TR-DOT systems to reconstruct 3D images was one of the principal challenges that hindered its expansion and wider use. Recently, several methods and algorithms were developed by researchers in the field to speed up data processing [104]. One of these approaches is to reduce the amount of data that is processed by the inverse problem solver and improve the image quality by focusing on the most useful points (seven well-defined points) of the DToF curves of the re-emitted photons [102]. After that, an inverse problem solver (utilizing seven well-defined points of DToF curves) was developed in our research group to reconstruct high-quality images for several shapes of turbid media (simulation based), which increases the algorithm's computational efficiency [24].

In this Chapter, a TR-DOS setup was built and integrated with the accelerated inverse problem solver to reconstruct 3D tomographic images of solid cylindrical phantoms [24]. The performance of this integrated TR-DOT prototype is investigated using the accelerated inverse problem solver to analyze the experimental raw data (DToF curves) generated by the TR-DOS setup. The performance of the TR-DOT prototype is evaluated based the computational load and time (speed of image reconstruction process) along with several essential criteria for diffuse optical imaging

such as accuracy of the OP quantification of inclusions and phantoms, inclusions detection, and localization.

The Chapter is organized as follows. In Section 3.2, the components of the TR-DOT prototype such as light sources, the photons counting and timing subsystem, and the inverse problem solver are discussed. In Section 3.3, preparation of phantom and inclusion materials, measurement of IRF_{Total} , and procedures for recording the DToF histograms are described. In Section 3.4, the results of the system (3D images and recovered OP of the turbid media) are discussed, and the performance of this prototype is evaluated according to different conditions for the experiments. The main contribution of this Chapter is to validate a computationally efficient TR-DOT that ensures fast reconstruction of high quality 3D images using a relatively small amount of measured data from a reasonable number of source-detector pairs. This work can lead to the development of real-time TR-DOT systems in the near future.

3.2. Prototype Architecture

The TR-DOT prototype has two main parts: TR-DOS setup and software for the image reconstruction process.

3.2.1. TR-DOS setup

A pulsed diode laser (685 nm) is used for illumination with a maximum average power of ~ 10 mW [68]. Light is transmitted from the laser source to a phantom through a multi-mode optical fiber [163]. Another optical fiber collects the re-emitted photons from the phantom (Edmund Optics Inc., numerical aperture= 0.22 and diameter = 1 mm). These photons are counted by a state of art SPADs detector (PDM series, MPD Italy) with a pixel that has a diameter of $50 \mu\text{m}$ [164] [152]. The laser driver and SPADs are connected to a Time-Correlated Single Photon Counting (TCSPC) module (PicoHarp 300, Picoquant) to measure the IRF_{Total} of the TR-DOS setup, and to acquire histograms of DToF for all source-detector pairs [94]. Figure 3-1 shows the main components of the TR-DOT prototype.

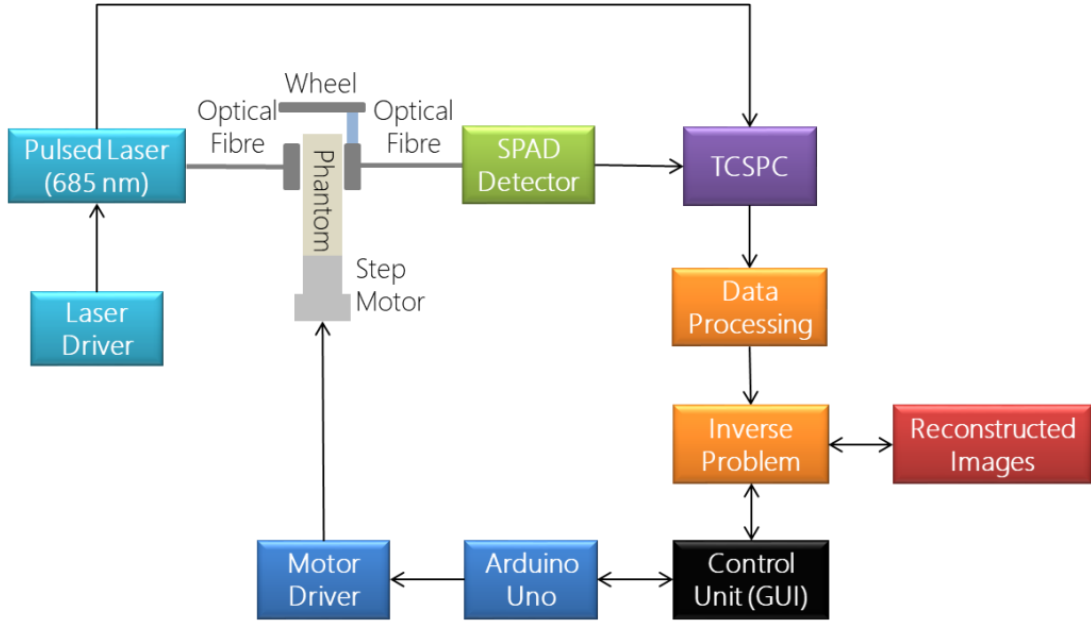


Figure 3-1: Diagram of the time-resolved diffuse optical tomography (TR-DOT) prototype.

In the TR-DOS setup, a wheel is installed horizontally to adjust the positions of the detectors, while source positions are adjusted using a bipolar stepper motor to rotate the phantom [165]. The motor makes precise movements and has 200 steps per rotation (1.8 degrees per step). In order to control this motor effectively, it is paired with a motor driver and an Arduino Uno microcontroller. With this setup, it is possible to perform precise measurements to emulate a multichannel system and accurately replicate experiments.

3.2.2. Image Reconstruction Process

Light propagation in a turbid medium can be described using the time-dependent diffusion equation (TD-DE) with a boundary condition such as the Robin boundary condition at a particular wavelength [23] [24]. The TD-DE and the Robin boundary condition are given by Eq. (3.1) and Eq. (3.2) respectively.

$$\left(\frac{1}{c'} \frac{\partial}{\partial t} - \nabla \cdot \kappa(r, \lambda) \nabla + \mu_a(r, \lambda)\right) \varphi(r, t, \lambda) = S(r, t, \lambda) \quad (r \in \Omega) \quad (3.1)$$

$$[1 + 2\kappa(r, \lambda) \xi \hat{n}(r) \cdot \nabla] \varphi(r, t, \lambda) = 0 \quad (r \in \partial\Omega) \quad (3.2)$$

Here c' is the speed of light in turbid media, $\kappa(r, \lambda)$ is the diffusion coefficient at a specific wavelength and is defined as $[3(\mu_a(r, \lambda) + \mu'_s(r, \lambda))]^{-1}$. In addition, $\mu_a(r, \lambda)$ and

$\mu'_s(r, \lambda)$ are the absorption and reduced scattering coefficients, respectively. However, in the TD-DE, the role of the absorption coefficient can be eliminated because most tissues have $\mu'_s \gg \mu_a$, hence the diffusion coefficient can be expressed as $[3 \mu'_s(r, \lambda)]^{-1}$ [8] [10]. The light fluence rate is $\phi(r, t, \lambda)$ and the source distribution is $S(r, t, \lambda)$. The domain is represented by Ω and the boundary is the derivative of the domain $\partial\Omega$. \hat{n} is a unit vector pointed outwardly normal to $\partial\Omega$, whereas ξ is derived from Fresnel's law as follows:

$$\xi = \left((2/(1 - R_0)) - 1 + |\cos \theta_c|^3 \right) \quad (3.3)$$

In Eq. (3.3) R_0 is the reflectivity and $R_0 = (n-1)^2 / (n+1)^2$, where n is the refractive index of the turbid medium (e.g. tissue). Also, θ_c represent the critical angle and is given by $\theta_c = \sin^{-1}(1/n)$.

In this Chapter, 3D DOT images are reconstructed using an algorithm that was described and published in [24] [166]. The algorithm discretizes equation (3.1) for each temporal bin in the histograms of DToF. The finite element method is then used to solve the discretized equation (3.1) for each mesh node within the turbid media. This algorithm analyzes only three points from the rising edge and four points from the falling slope of the DToF histogram for each source-detector pair, and these seven points are stored in the index matrix. These points are specified as a fraction of the maximum number of counted photons of each DToF histogram, which are 20%, 50%, and 80% on the rising edge and 80%, 50%, 20%, and 10% on the falling slope [102] [24]. The Jacobians are calculated by a recursive direct method from these seven points to recover the OP of each node inside the turbid medium and to detect and localize any heterogeneity [24].

The recursive algorithm assumes equal μ'_s and μ_a for all nodes in the phantom in the first iteration. In the following iterations, the values of μ'_s and μ_a are only updated for nodes within the **region of interest (ROI)** while the OP values remain constant in the rest of the medium. During each iteration, the Jacobian matrix is calculated for all seven selected points (using a direct matrix multiplication) for all source-detector pairs which significantly reduces the computation time. The algorithm reconstructs images by recovering the OP of each mesh node within the ROI that represents a specific part of the cylindrical phantom, and the source-detector plane is located in the center around

the ROI. This iterative inverse problem algorithm ends when either the results of the forward model (fitted DToF curves) using the assumed OP match the measured results to a certain degree (by solving the minimization problem) or when the specified maximum number of iterations is reached (Figure 3-4).

The minimization problem is ill-posed and requires a regularization scheme to get a convergent and stable solution. The regularization scheme used, as described in [24], is based on solving the minimization problem in a normalized space wherein the sensitivity of the Jacobian matrix is made equal for all nodes in the ROI. Therefore, at each iteration, the minimization function uses different dynamic ranges of the lower and upper limits of the OP at each node based on the corresponding magnitudes of the Jacobian matrix. Therefore, to fit the light fluence data, the minimization function gives priority for changing the OP for deep regions where the Jacobian magnitudes are low, more than that given to the boundary regions where the Jacobian magnitudes are high. This regularization scheme does not require adding an additional penalty term to the objective function for convergence [24]. The reconstructed OP in the original space are obtained by scaling back the reconstructed OP in the normalized space as shown in [24]. In this Chapter, the iterative solution of the minimization problem continues until the change in the maximum error of the simulated fluence relative to the measured fluence goes below 5%, or the predefined maximum number of iterations is reached. More details about the image reconstruction algorithm that is used in this Chapter can be found in [24] [166].

3.3. Measurements

Measurements were taken using an identical arrangement for the source-detector pairs. Each source was monitored with seven detectors located at 90°, 120°, 150°, 180°, 210°, 240°, and 270° degrees (with respect to the source) around a cylindrical phantom. The required number of source-detector pairs was investigated (in simulation) to determine the best possible arrangements to reduce the time in the image reconstruction process and maintain a high quality of the images. It was found that increasing the number of sources to more than 12 did not have a significant effect on the quality of images, probably due to the small size of the phantoms. This configuration was used at multiple positions around the phantom (scanning) to emulate a multichannel prototype.

For precise positioning, a computer controlled step motor was used to rotate the phantom to adjust the positions of the injected laser pulse according to the number of views. The standard configuration used: hard prior, 15 mm ROI, 20 is the maximum number of iterations, 12 sources with 84 detectors at the same height around the phantoms for all measurements except when the impact of fewer sources or detectors, the impact of prior knowledge, and a larger ROI are investigated.

3.3.1. Phantoms and Inclusions

Phantoms were prepared using epoxy resin with hardener, titanium dioxide (TiO_2), and India ink for the phantom matrix media, scattering agent and absorbing agent, respectively. A ratio of weight (10/3) is used for mixing Araldite® Epoxy Resin with Aradur® hardener produced by Huntsman Advanced Materials Inc., USA [167]. To adjust μ_s' and μ_a , TiO_2 from Sigma-Aldrich Co. LLC, USA, and India ink were used, respectively [168]. On the other hand, inclusion materials were prepared using mixtures of matrix media (gelatin), scattering agent (TiO_2), and absorption agent (India ink). The OP values of each mixture of these materials were determined using a steady-state spatially resolved diffuse reflectance system (Figure 3-2). In this system, a Quartz Tungsten Halogen (QTH) lamp was used to illuminate the phantom and inclusion materials. The re-emitted light was detected at different distances from the source (see the probe in Figure 3-2). Then, an inverse problem solver was used to recover the OP of the phantom and inclusion materials over a broad range of wavelengths.

In this Chapter, two solid cylindrical phantoms (25 mm diameter each) are used, one with one hole, and the other with two holes. The first phantom has one hole (15 mm diameter) and the second phantom has two holes (5 mm diameter each), and each hole was filled with a mixture of inclusion.

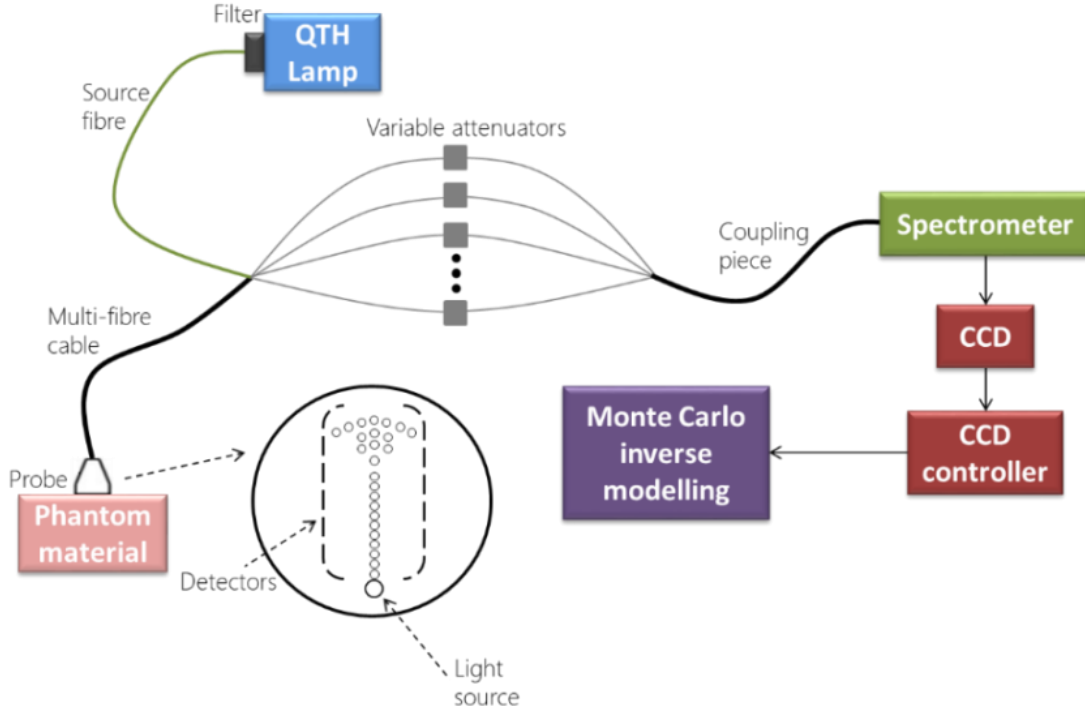


Figure 3-2: Diagram of steady-state spatially resolved diffuse reflectance system used to determine the optical properties (OP) accurately for the phantoms and the inclusion materials.

3.3.2. Instrument Response Function

For TR-DOT experiments, the FWHM of the IRF_{Total} of the system should be estimated and considered in the inverse problem solving to improve the accuracy of the recovered OP [58] [82]. The FWHM of the IRF_{Total} represents the square root of the sum of squares of the IRF for each equipment in the setup such as the laser source, the detector, optical fibers, and the TCSPC module using [91] [117] [118] [145]:

$$FWHM \text{ of the } IRF_{Total} \approx \sqrt{IRF_{laser}^2 + IRF_{Detector}^2 + IRF_{OpFb}^2 + IRF_{TCSPC}^2} \quad (3.4)$$

To accurately measure the FWHM of the IRF_{Total} , the detected photons should have a similar angular distribution of the re-emitted photons from a thin highly scattering material, such as a sheet of white paper or Teflon tape that is inserted between the light source and detector [105]. A very thin sheet ensures negligible broadening of the illuminated pulse while scattering events occur inside the sheet [91] [105]. However, when the IRF_{Total} is measured with nothing between the detector and source, the photons arrive in one direction. The IRF_{Total} is measured by placing a thin diffuser (a sheet of white paper) between the terminals of the two optical fibers that are connected

to the laser source and detector [120]. The IRF_{Total} must not exceed one ns because a large IRF_{Total} may ruin the DToF histograms causing them to be invalid for image reconstruction. This is because an ultrashort pulse (FWHM < 100 ps) of injected light is broadened by about one ns (FWHM) for each centimeter that light propagates in biological tissues [75]. However, the measured IRF_{Total} of this setup was very good (< 300 ps) which helped the inverse problem solver in image reconstruction (Figure 3-3) [169].

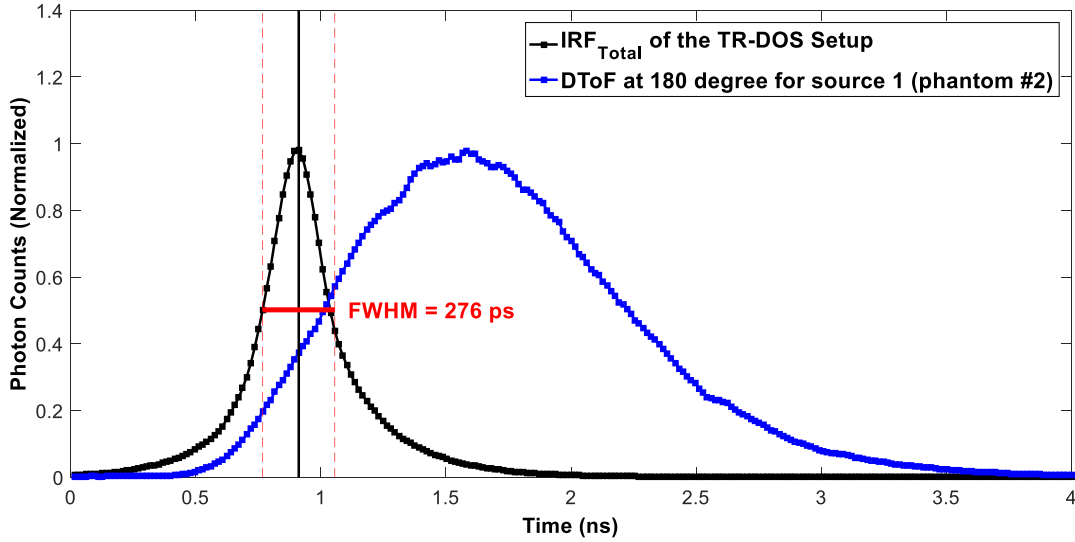


Figure 3-3: The FWHM of the IRF_{Total} of our TR-DOS setup (~ 0.3 ns) and the acquired DToF at 180° .

The measured FWHM of the IRF_{Total} should be deconvolved from the measured DToF histograms to calibrate the raw data, or convolved in the iterative inverse problem-solving. It is worth noting that deconvolution is time-consuming and an ill-posed problem [75]. Therefore, the measured FWHM of the IRF_{Total} is convolved with the simulated $DToF$ in the inverse problem solver to eliminate the impact of IRF_{Total} of the setup using [170]:

$$DToF_{Fitted} = DToF_{Simulated} * FWHM \text{ of the } IRF_{Total} \quad (3.5)$$

3.3.3. Data Acquisition

Light injected into the phantoms had 0.5 mW optical power measured at the tip of the fiber, and a repetition rate of 10 MHz. A SPAD detector counts the re-emitted photons in free running mode [25]. All DToF histograms are acquired using the same period of measurement (30 s to count the reemitted photons for each source-detector pair) for all phantoms with a temporal resolution of 16 ps for the TCSPC module. Also,

the laser power is fixed for illuminating the two phantoms, and all measurements are taken with no “pile-up” effect which may significantly degrade the accuracy of the measured data [82] [118]. Figure 3-4 shows a flowchart that describes the process, starting from data acquisition, followed by the iterative inverse problem solver, until the reconstruction of tomographic images of the phantom. It is worth noting that the stated computation times in this Chapter is for image reconstruction processes that are done using a personal laptop (Asus N43S) with the following specifications. The processor is Intel Core i7-2670QM 2.2GHz Quad-Core, Cache memory is 6 MB, and Random-access memory (RAM) is 8 GB.

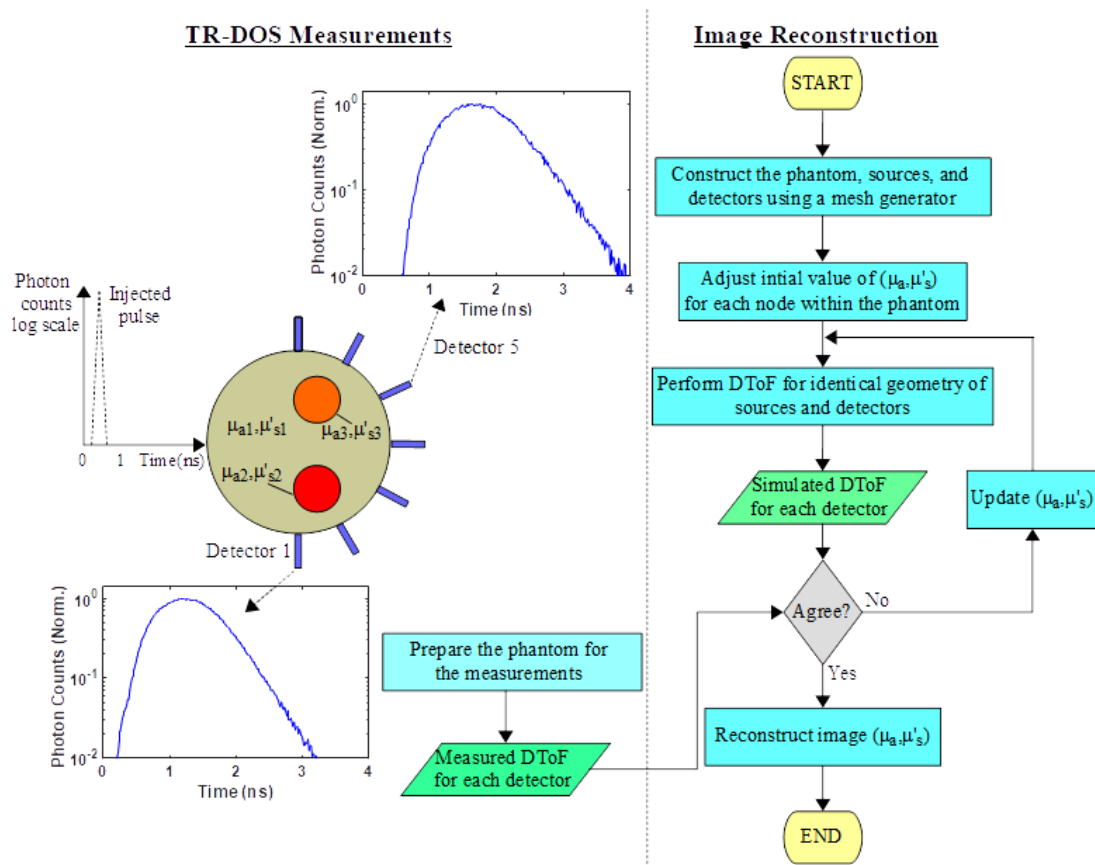


Figure 3-4: Flowchart of the integrated TR-DOT prototype.

In this Chapter, hard prior was used to segment the phantoms in all experiments. Therefore, in the first step of the image reconstruction process, tetrahedral meshes are generated by Iso2mesh (open-source software) to construct the phantom, inclusions, sources, and detectors [171]. Fine density of meshes (10 nodes per mm³) of the phantoms was used in these experiments to ensure the high quality of the reconstructed

images. Then, the iterative inverse problem solver starts the comparison with the calibrated raw data (DToF for each source-detector pair) as described earlier (subsection 3.2.2). This comparison is achieved by solving the minimization problem using the function ‘fmincon’ of Matlab. In all experiments, the initial guess of μ_s' and μ_a were 1.8 mm^{-1} and 0.015 mm^{-1} , respectively. The lower and upper limits used (in the minimization problem) are 0.25 and 7 mm^{-1} of μ_s' , and 0.0025 and 0.08 mm^{-1} of μ_a , respectively. Also, the results using different number of points on the recorded DToF histograms were compared and analyzed. From this analysis, it was determined that using seven points is enough to maintain the quality of the reconstructed images and speed up of the computational process.

3.3.4. Quantification Accuracy of the OP

To reconstruct the OP accurately, the linearity and accuracy of the prototype should be evaluated [172] [173]. For this purpose, the impact of changing μ_s' and μ_a for inclusion were simulated separately, and the recovered OP for inclusion and background obtained in two different ways. First, in Figures 3-5 (a) and (b), the linearity is shown of the recovered μ_s' and μ_a for inclusion and background versus several values of the actual μ_s' and μ_a of the inclusion, respectively. Second, the crosstalk (coupling) between μ_s' and μ_a is displayed. The crosstalk can be observed in Figures 3-5 (c) and (d) from the recovered μ_a and μ_s' for inclusion and background versus several values of the actual μ_s' and μ_a of the inclusion, respectively. From these results, it is seen that the prototype maintains accurate linearity for the recovered OP of the inclusion in Figures 3-5 (a) and (b), and the recovered OP values for the background slightly fluctuate. However, the crosstalk between μ_s' and μ_a is negligible with small values of the actual OP, but it increases noticeably when larger values of μ_s' and μ_a are used.

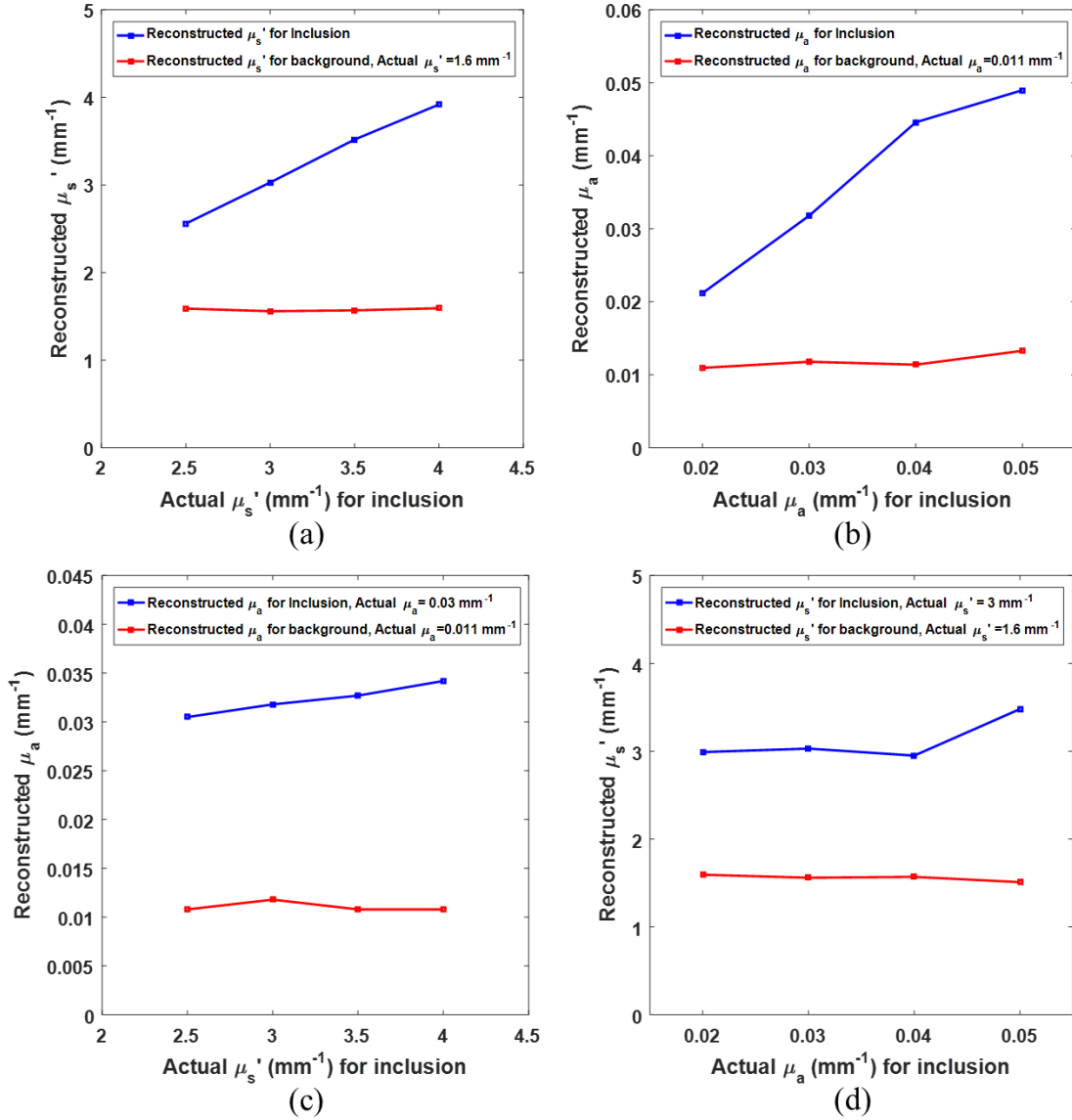


Figure 3-5: Cross-correlation of the actual OP of the inclusion versus the recovered OP for inclusion and background of the first phantom (one inclusion). (a) Recovered μ_s' against actual μ_s' ; (b) Recovered μ_a against actual μ_a ; (c) Recovered μ_a against actual μ_s' ; and (d) Recovered μ_s' against actual μ_a .

3.4. Results and Discussions

The TR-DOT prototype is evaluated separately for each change in the configurations of the source-detector pairs, sizes and the OP of inclusions, as well as the chosen settings for the inverse problem. First, the accuracy of the OP quantification and the time of image reconstruction for two phantoms are estimated using the standard configuration described in Section 3.3. The first phantom has one inclusion, and the second phantom has two inclusions. Second, the effect on the image quality and the time of image reconstruction using a fewer number of sources (6) with seven detectors

for each source is shown for the second phantom. Third, 12 sources are used, but each source is with a fewer number of detectors (5 and 4) to investigate the expected decrease in the image quality and the time of image reconstruction of the second phantom. Fourth, the impact of prior knowledge of the structure of the first phantom is investigated by comparing reconstructed images with and without hard prior. Fifth, the influence of prior knowledge on the image quality and the time of image reconstruction are studied for the second phantom using different sizes for the ROI (1.5 and 1.8 cm). Figure 3-6 displays images of the actual OP recovered by the steady-state spatially resolved diffuse reflectance system (Figure 3-2) for the phantoms. For the first phantom, the actual values of μ_s' and μ_a are 1.6 mm^{-1} and 0.011 mm^{-1} for the background, and 4 mm^{-1} and 0.05 mm^{-1} for the inclusion, respectively. For the second phantom, the actual values of μ_s' and μ_a are 1.6 mm^{-1} and 0.011 mm^{-1} for the background, 6 mm^{-1} and 0.075 mm^{-1} for the right inclusion, and 3 mm^{-1} and 0.038 mm^{-1} for the left inclusion, respectively.

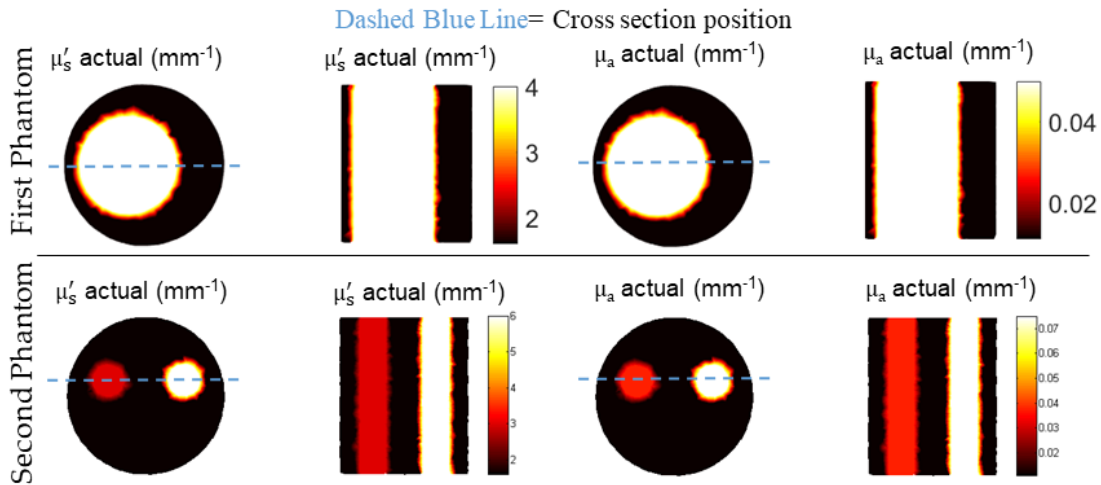


Figure 3-6: Cross-sectional and sagittal views of images for actual μ_s' (left) and μ_a (right) coefficients for two phantoms: (row one) the first phantom, and (row two) the second phantom.

3.4.1. Image Reconstruction on Phantoms

The first step in evaluating the performance of the prototype is to compare the quality of the reconstructed images for both phantoms that have known OP as shown in Figure 3-6. Accurately determining the OP is important; however high precision is mainly required for μ_a because small variations of μ_a is the main factor associated with blood clots and tumors that usually contain more blood vessels than healthy tissues.

Also, μ_a is associated with the hemodynamic response during muscles or brain activities in functional imaging [119] [174] [54]. 3D images were reconstructed, and Figure 3-7 shows cross-sectional and sagittal views for all phantoms using the standard configuration described in Section 3.3. The total time for image reconstruction process (shown in Figure 3-7) was ~ 480 seconds of each phantom.

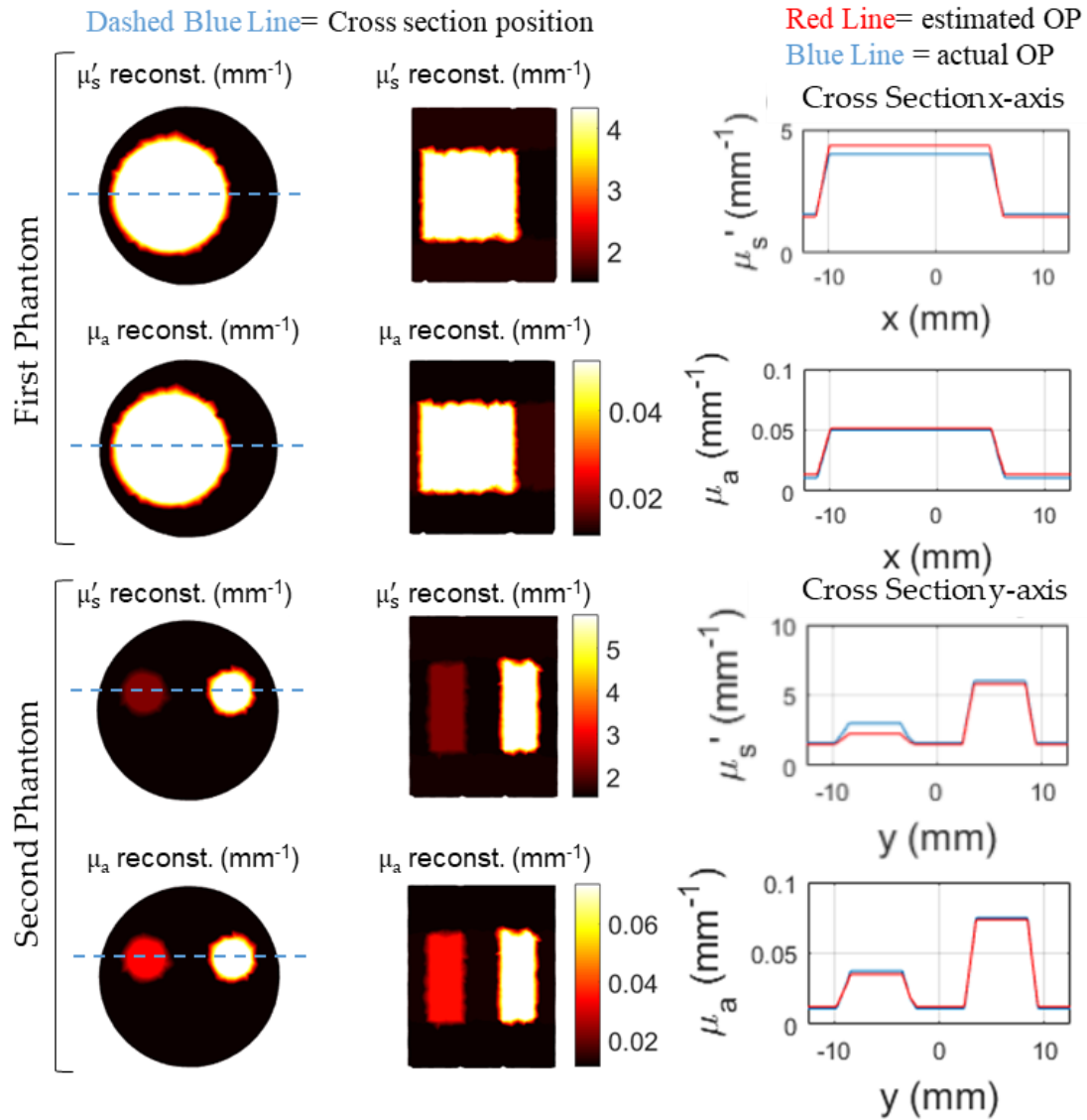


Figure 3-7: Left column: cross sectional and sagittal views of images. Right column: the recovered μ'_s and μ_a for: the first phantom (rows one and two), and the second phantom (rows three and four).

The image reconstruction using this configuration yields good results for both phantoms. The good results can be attributed to having enough information for the image reconstruction process due to the small size of the phantoms and using hard prior.

For instance, hard prior is used to segment the first and the second phantoms into two and three homogeneous regions, respectively. The error percentage in accuracy for the reconstructed OP for phantom (background or inclusion) can be calculated using the following equation [106]:

$$\varepsilon = \frac{OP_{reconstructed} - OP_{Actual}}{OP_{Actual}} \times 100 \quad (3.6)$$

Overall, the accuracy of the reconstructed μ_s' and μ_a is very good (error $\sim 5\%$), particularly for μ_a . Note that the recovered μ_s' of the inclusion material is overestimated by an acceptable range of error ($\sim 8\%$) for the inclusion in the first phantom, and underestimated for one inclusion for the second phantom ($\sim -13\%$). The overestimation of the recovered μ_s' of the inclusion (in the first phantom) is probably caused due to the crosstalk between μ_s' and μ_a as described in subsection 3.3.4. On the other hand, the underestimation of the recovered μ_s' for the left inclusion (in the second phantom) is caused by the variation of μ_s' and μ_a in the right inclusion. This inaccurate estimation was also noticed in the simulated results when there is a large variation between the OP used for the two inclusions. The experimental results in this subsection are for the standard configuration for the prototype and will be referenced throughout this Chapter. The results of varying the experimental conditions such as the number of sources and detectors, prior knowledge and ROI size are examined in the following subsections.

3.4.2. Impact of Number of Sources

Increasing the number of source-detector pairs plays a significant role in improving the quality of the images because more photons are collected at more positions on the phantom surface. This results in a larger dataset of the DToF histograms to be processed by the inverse problem solver. In this subsection, the impact of using fewer source-detector pairs is investigated by reducing the number of sources, but keeping the number and positions of detectors for each remaining source the same as in the standard configuration (7 detectors per source). Therefore, the variation in image quality and the time of image reconstruction are compared using two measurement configurations with 12 and 6 sources attached to 84 and 42 detectors respectively. The tradeoff is investigated between reducing the time of data acquisition

and image reconstruction process without losing the acceptable quality of images. The results are shown in Figure 3-8.

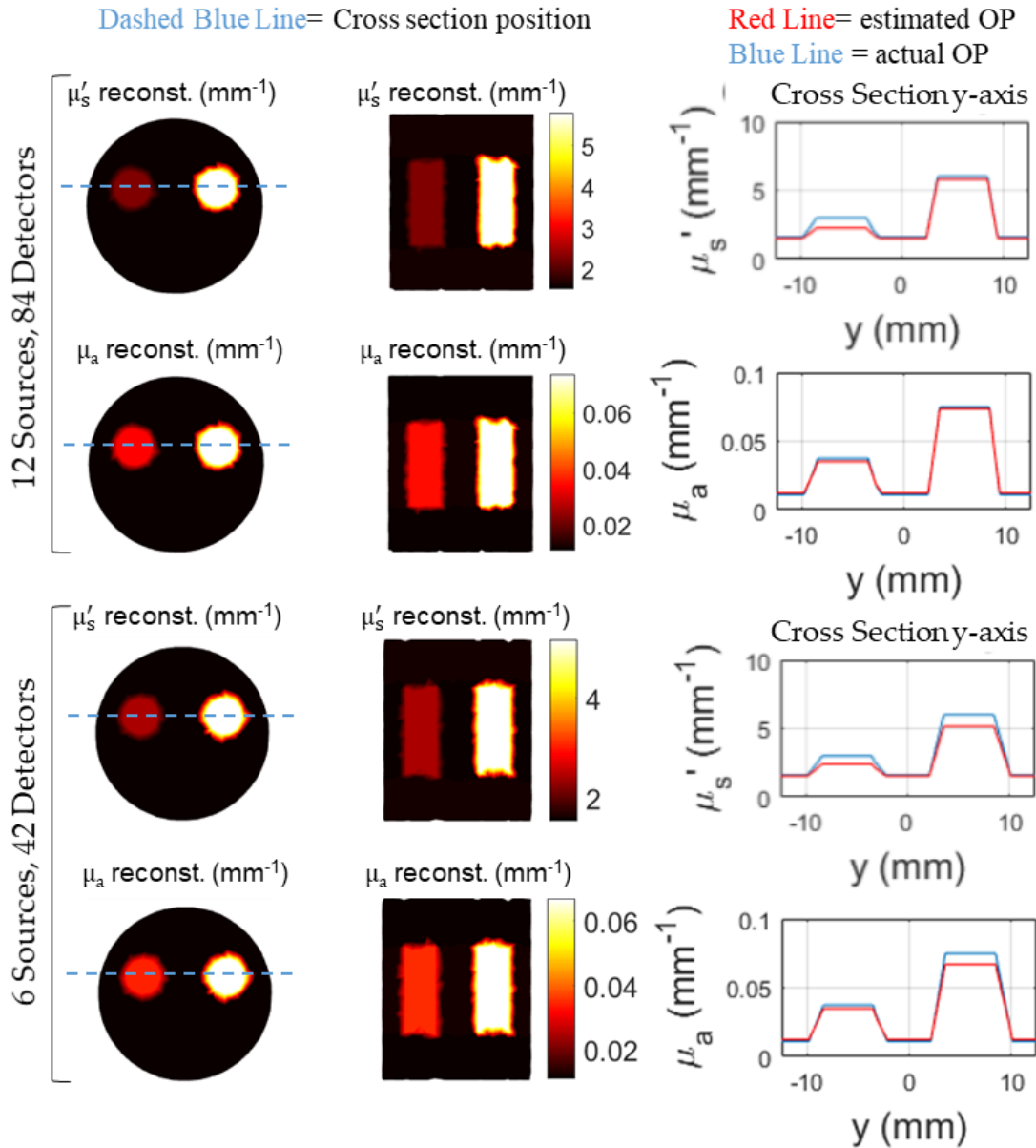


Figure 3-8: Left column: Cross-sectional and sagittal views of images. Right column: the recovered μ_s' and μ_a for the second phantom: 12 sources and 84 detectors (rows one and two), and 6 sources and 42 detectors (rows three and four).

In Figure 3-8, it is shown that reducing the number of sources to 6 yields nearly the same accuracy of the recovered OP of the background (phantom) as the standard configuration in subsection 3.4.1 with 12 sources and 84 detectors. Also, the accuracy of the recovered μ_s' and μ_a of the right inclusions is slightly lower than the actual values

as a result of decreasing the number of measured DToF histograms that are used in the inverse problem. This underestimation of the recovered μ_s' and μ_a for the right inclusion leads to a decrease in the variation between the actual and the recovered μ_s' of the left inclusion due to the crosstalk between the two inclusions. All 3D images were reconstructed, and total time for image reconstruction for the experiments using 12 and 6 sources were 480 s and 300 s, respectively. Overall, for a phantom of this size, using half the number of sources compared to the standard configuration results in accurate images requiring a shorter time for data acquisition and analysis. For this size of phantoms or tissue, a smaller number of sources is beneficial as the data acquisition time and the time of image reconstruction will be reduced, and the inclusions are still detected but with a slightly lower accuracy of quantification of the OP values.

3.4.3. Impact of Number of Detectors

Reducing the number of source-detector pairs by using fewer detectors per source is expected to reduce the quality of the images and the time of image reconstruction. Here, these effects are investigated by comparing results from the standard configuration (seven detectors per source) with experiments in which five and four detectors per source are used. The first experiment has the same detector configuration as the standard configuration, except that two detectors are removed (90° and 270°) when five detectors are used. In the second experiment, four detectors are used (90° , 150° , 210° and 270°) to investigate the effect of reducing the number of detectors without reducing the span.

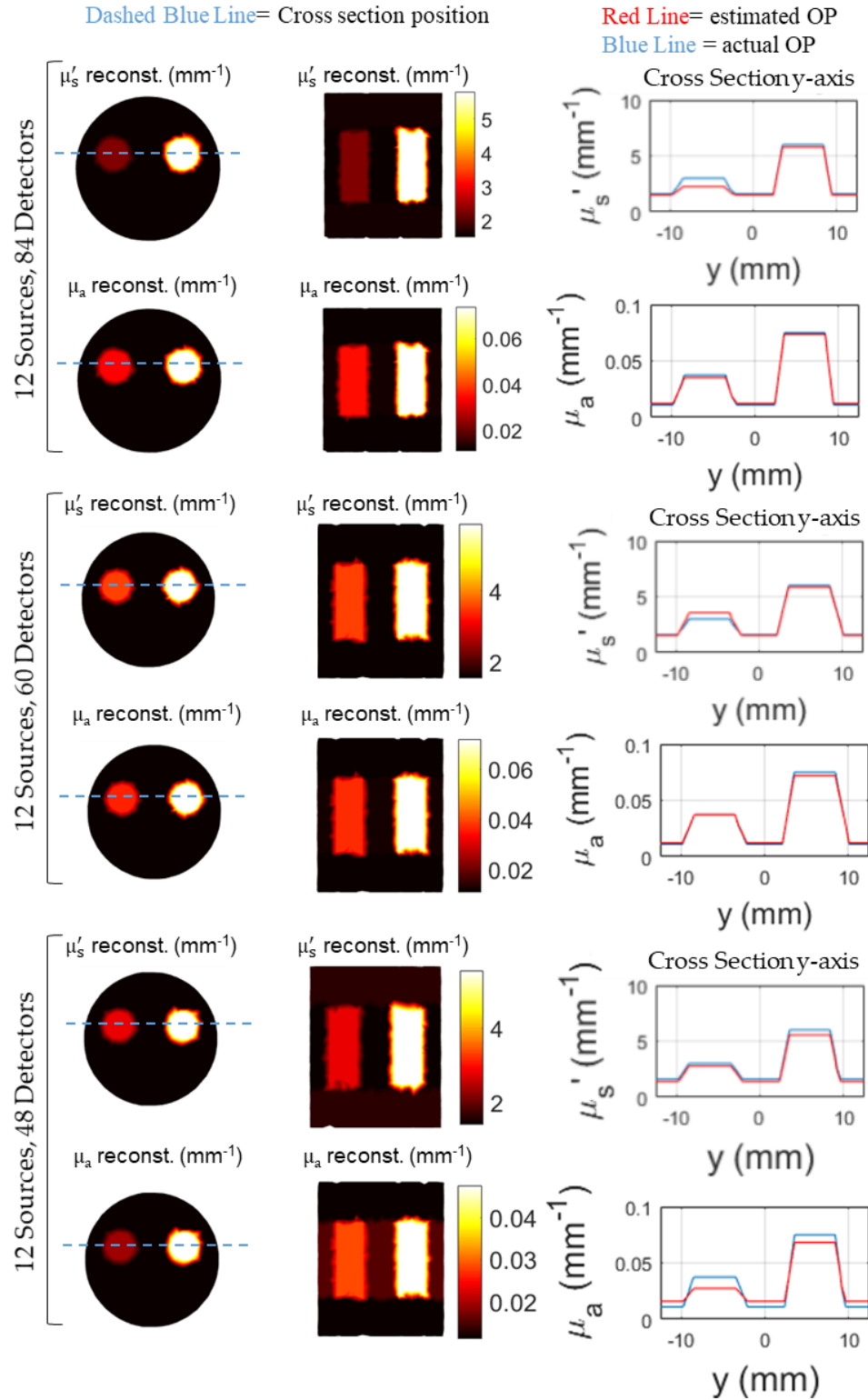


Figure 3-9: Left column: Cross-sectional and sagittal views of images. Right column: the recovered μ_s' and μ_a for the second phantom: 12 sources and 84 detectors (rows one and two), 12 sources and 60 detectors (rows three and four), and 12 sources and 48 detectors (rows five and six).

From the results in Figure 3-9, it can be noticed that decreasing the total number of detectors from 84 to 60 resulted in almost the same accuracy in the estimation of the OP of the phantom and the inclusions. In the experiment with five detectors per source, μ_s' of the inclusions are slightly overestimated (for left inclusion) while the estimated μ_a remain almost as accurate as in the standard configuration. In contrast to the previous experiment, the accuracy of the reconstructed OP is degraded significantly when only four detectors per source (12 sources – 48 detectors) are used for the span of 90° to 270° . Therefore, using four detectors for this span automatically increases the gap between each two detectors to 60° , which results in a noticeably reduced accuracy of the recovered μ_a (in this experiment) for the background and two inclusions. Consequently, in this experiment, the resulting large overestimation of the recovered μ_a (almost 35%) for the background degrades the accuracy of the recovered OP. The total time for image reconstruction for the experiments using 84, 60 and 48 detectors was 480 s, 370 s, and 310 s, respectively. Overall, by a reasonable reduction in the number of detectors without increasing the separation of 30° between them, the data acquisition and the time of image reconstruction can be shortened while obtaining accurate OP.

3.4.4. Influence of Prior Knowledge

Having prior knowledge of a phantom's structure is required to generate high quality images using any inverse problem solver. Without prior knowledge, the DToF data alone is not enough to estimate the size and accurately localize inclusions and OP [12] [33] [119]. In this subsection, the impact of the incorporated prior knowledge on the image reconstruction with this prototype is investigated. In Figure 3-10, the results obtained for the first phantom are compared with hard prior and without the use of prior knowledge.

The results obtained from the reconstruction process without prior knowledge demonstrate poor localization and poor size estimation of the inclusion. They also show that the recovered OP of the phantom and inclusion are not very accurate, and variations between the actual OP and the recovered OP will be higher at other positions in the cross-section. Also, it is noticed that in this prototype, we can detect the existence of one large inclusion in the phantom (Figure 3-10, rows 3 and 4) which is very beneficial

for situations where prior anatomical knowledge is not available. The poor localization and size estimation results of the inclusion agree with known limitations of the full image reconstruction problem in DOT which leads to blurry images when no prior knowledge is incorporated into the ill-posed inverse problem [103]. On the other hand, the absence of prior knowledge increases the number of unknowns (mesh nodes) which dramatically increases the computation time for image reconstruction [11]. To reconstruct images without prior structural information, the computation time increased to 3300 s, whereas it required only 480 s when hard prior knowledge was incorporated.

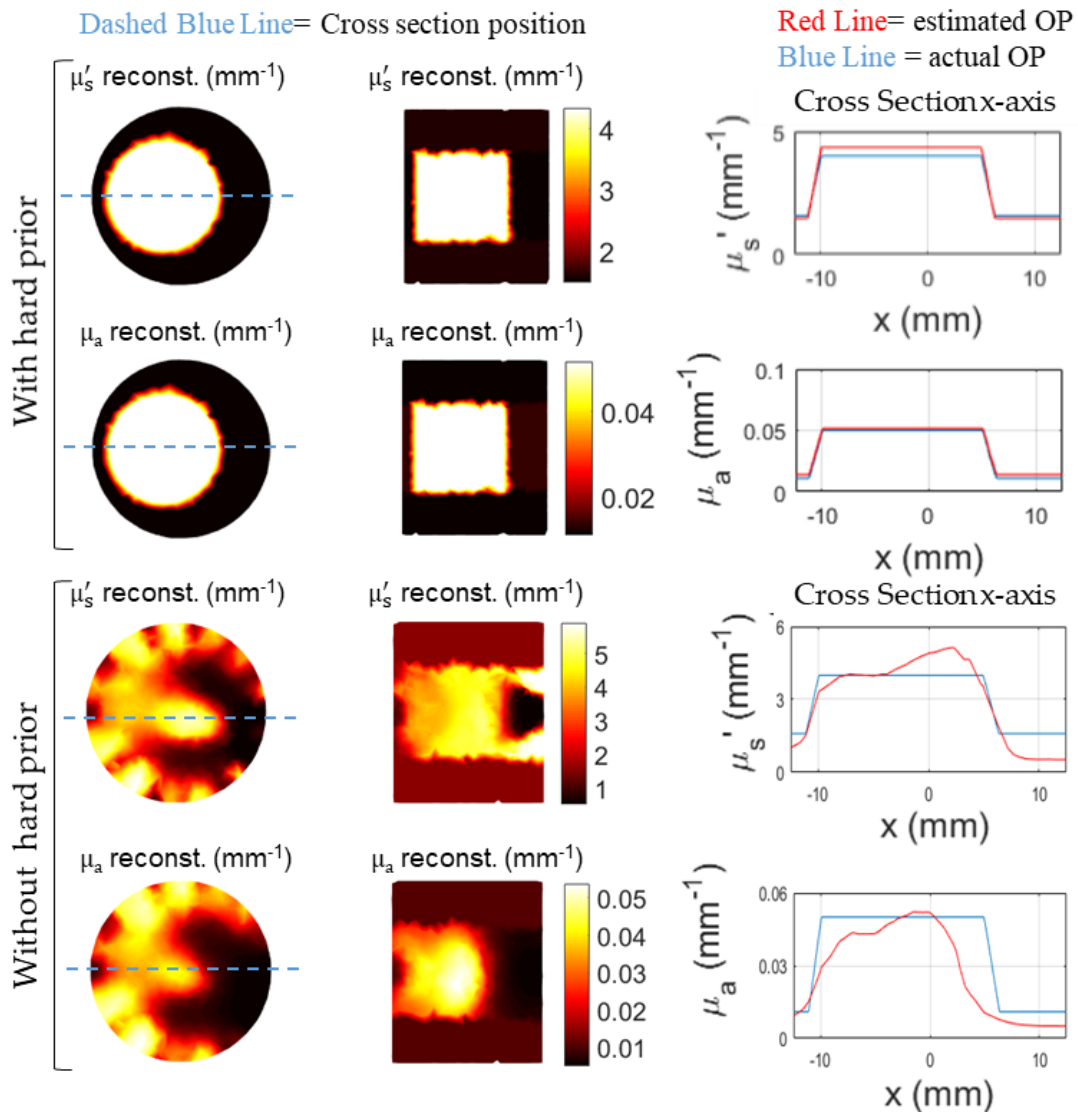


Figure 3-10: Left column: cross sectional and sagittal views of images. Right column: the recovered μ'_s and μ_a for the first phantom: with hard prior (rows one and two), and without prior knowledge (rows three and four).

3.4.5. Influence of ROI Size

Increasing the size of the ROI is expected to increase the under-determination of the inverse problem and consequently reduce the accuracy of the estimated OP and increase the time it takes to reconstruct images from measurements. Also, the absence of prior knowledge along with a larger ROI is expected to decrease the accuracy of the reconstructed images because of the larger amount of unknown nodes that require OP estimation. In this subsection, the ability of the prototype to detect two small inclusions in the second phantom using two different sizes of ROI (1.5 and 1.8 cm), and without incorporating hard prior is investigated. Figure 3-11 shows the results using 12 sources and 84 detectors.

These results show that there is poor localization of the inclusions which degrades the quantification of the recovered OP in the cross-section at the real positions of inclusions. Also, from the cross-sectional images, the inclusions can be observed in the upper half of the cylinder. The right inclusion can be detected without difficulty due to its large OP values. However, the absence of prior knowledge makes the inclusion's detection, OP quantification, and localization less accurate, particularly for small inclusions. In addition, several source-detector planes at different heights around the phantom are required if the ROI is enlarged and prior knowledge is not incorporated. Therefore, the ROI was increased by 20% to 1.8 cm, and the results are similar to the original ROI (1.5 cm), whereas the computation time for image reconstruction increased noticeably. The total reconstruction time was 3200 s, and 3700 s for 1.5 and 1.8 cm ROI sizes, respectively.

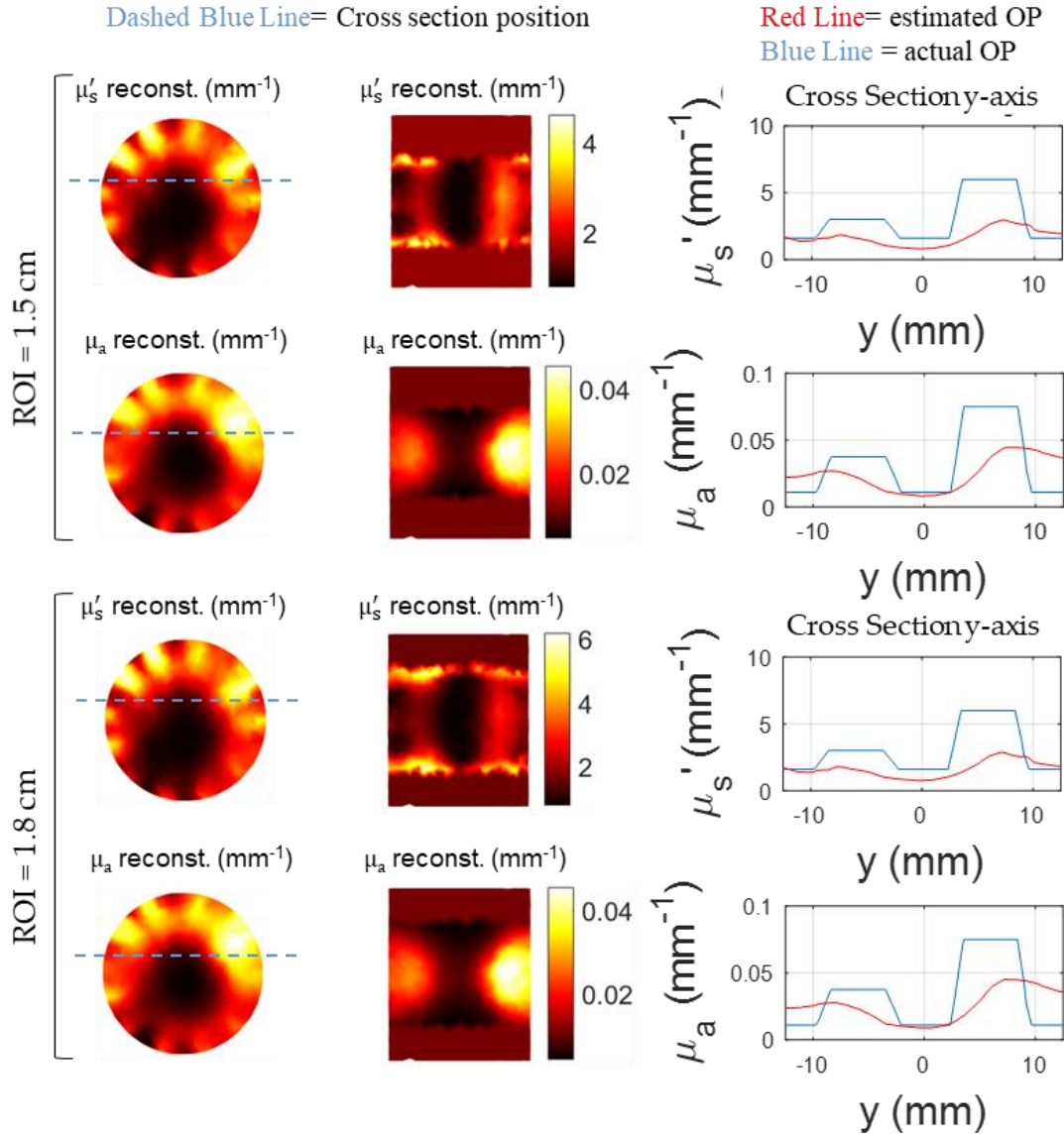


Figure 3-11: Left column: cross sectional and sagittal views of images. Right column: the recovered μ_s' and μ_a for the second phantom without prior knowledge: 1.5 cm ROI (rows one and two), and 1.8 cm ROI (rows three and four).

3.5. Conclusions

In this Chapter, a major step towards building real-time TR-DOT prototypes to reconstruct high quality 3D images was demonstrated through experiments. The reported TR-DOT prototype significantly reduces the total amount of time required to generate high quality images of objects using a TR approach, when using 7 points on each recorded DToF histogram. This reduces the computational complexity of the

inverse problem solver, which accelerates the image reconstruction without degrading the accuracy of the OP quantification for phantoms and inclusions.

To evaluate this prototype for diffuse optical tomography applications, several experimental variations were used with the configuration, phantoms, and inverse problem solver settings. Two phantoms that were cylindrical in shape and had OP similar to normal human tissues were used. The first phantom has a large inclusion (15 mm diameter) and the second phantom has two small inclusions (5 mm diameter each). In the first experiment, images are reconstructed on both phantoms using the standard configuration (hard prior, 15 mm ROI, 20 is the maximum number of iterations, 12 sources with 84 detectors at the same height around the phantoms), and high quality images were reconstructed in 8 minutes for each phantom. Also, the accuracy of distinguishing the variation of the OP of two small inclusions in the same phantom was successfully tested.

In the second and third experiments, the results were discussed when using fewer numbers of sources and detectors on the second phantom. The accuracy of the recovered OP and the time of image reconstruction process in the second and third experiments were compared with the first experiment. Reducing the total number of sources and detectors by 50% (in the second experiment) from the standard configuration maintained the quality and accuracy of the reconstructed images and the estimated OP, respectively. Also, the time of image reconstruction process is reduced from 8 minutes in the first experiment to 5 minutes in the second experiment (using 6 sources and 42 detectors).

In the third experiment, reducing the number of detectors per source (when 5 detectors per source are used, and the small gap 30° between detectors is maintained) preserved the quality of the reconstructed images. Also, the accuracy of the recovered OP is preserved particularly of μ_a , when compared to the results of the first experiment, whereas the time of image reconstruction process is decreased from 8 minutes to almost 6 minutes. However, the accuracy of the recovered OP was degraded considerably when four detectors per source (larger gap 60° between detectors) were used in the third experiment, and the time of image reconstruction process is decreased from 8 minutes to almost 5 minutes. In general, the second and the third experiments proved

that the data acquisition time of the measurements and the time required for the image reconstruction could be reasonably reduced if enough source-detector pairs (> 40) are used, and the small gap of 30° between detectors is maintained without degrading the quality of the reconstructed images.

In the fourth experiment, when the hard prior knowledge was not used, the image reconstruction process required a much longer time (~ 55 minutes), and poor size estimation and localization of the inclusion were observed. This requires further investigations into what alternative methods can be incorporated into our inverse problem solver to eliminate the poor results obtained when no prior knowledge is used.

In the fifth experiment, a larger ROI (1.8 cm) maintained the same level of accuracy in comparison with small ROI (1.5 cm), but the time for image reconstruction increased from 53 minutes to almost 62 minutes. The fifth experiment demonstrated that source-detector pairs at several heights are required with a larger turbid media in transmittance geometry when no prior knowledge is used, but the time of image reconstruction will be very long (> 1 hour). Overall, the variation of these conditions also helps to establish the best conditions to make image reconstruction fast and accurate when using this TR-DOT prototype for diffuse optical tomography applications.

Chapter 4

DEVELOPMENT OF A TIME-RESOLVED DIFFUSE OPTICAL SPECTROSCOPY PROTOTYPE USING LOW-COST AND COMPACT SPAD DETECTORS³

Time-resolved diffuse optical spectroscopy (TR-DOS) is an increasingly used method to determine the optical properties (OP) of diffusive media, particularly for medical applications including functional brain, breast and muscle measurements. For medical imaging applications, important features of new generation TR-DOS systems are low-cost, small size and efficient inverse modeling. To address the issues of low-cost, compact size and high integration capabilities, we have developed free-running (FR) single-photon avalanche diodes (SPADs) using 130 nm silicon complementary metal-oxide-semiconductor (CMOS) technology and used it in a TR-DOS prototype. This prototype was validated using assessments from two known protocols for evaluating TR-DOS systems for tissue optics applications. Following the basic instrumental performance protocol, our prototype had sub-nanosecond total instrument

³ Most of this chapter was published as: Alayed, M., Palubiak, D. and Deen, M., 2018. Characterization of a Time-Resolved Diffuse Optical Spectroscopy Prototype Using Low-Cost, Compact Single Photon Avalanche Detectors for Tissue Optics Applications. *Sensors*, 18(11), p.3680, pp. 1-18.

response function and low differential non-linearity of a few percent. Also, using light with optical power lower than the maximum permissible exposure for human skin, this prototype can acquire raw data in reflectance geometry for phantoms with optical properties similar to human tissues. Following the MEDPHOT protocol, the absolute values of the OP for several homogeneous phantoms were retrieved with good accuracy and linearity using a best-fitting model based on the Levenberg-Marquardt method. Overall, the results of this study show that our silicon CMOS-based SPAD detectors can be used to build a multichannel TR-DOS prototype. Also, real-time functional monitoring of human tissue such as muscles, breasts and newborn heads will be possible by integrating this detector with a **time-to-digital converter (TDC)**.

4.1. Introduction

Diffuse optical spectroscopy (DOS), also called **near-infrared spectroscopy (NIRS)**, is non-invasive and non-destructive technology to determine the OP of turbid objects such as tissues in which scattering dominates absorption [8] [21] [25]. DOS exploits the low absorption and high scattering of tissues in the optical window (also called biological window) at red and near-infrared wavelengths (600–950 nm) [9] [10]. In this range of wavelengths, light can diffuse in the tissue and penetrate up to a few cm [9]. Light propagation in turbid media is well described by the **radiative transfer equation (RTE)** and its simplified version, the **diffusion equation (DE)** [48]. Hence, re-emitted photons can be detected either in transmittance geometry (source and detectors not on the same side), or in reflectance geometry (source and detector on the same side of the object) for thin and thick objects [8] [98]. The detected signal using DOS can be analyzed using an inverse problem solver to retrieve the OP, particularly the reduced scattering coefficient (μ_s') and the absorption coefficient (μ_a) [10] [104]. Therefore, the OP of a homogeneous object or the distribution of OP for a heterogeneous object can be recovered [72] [175]. DOS measurements are made using three main approaches: **continuous-wave (CW)**, **frequency-domain (FD)**, and **time-resolved (TR)** [9] [176].

Continuous-wave diffuse optical spectroscopy (CW-DOS) has limitations in retrieving the absolute values of μ_s' and μ_a because this approach depends on one quantity (changes of light intensity) which only allows for estimating the change of μ_s'

and μ_a values [8] [10]. Both FD-DOS and TR-DOS can estimate the absolute values of μ_s' and μ_a with good accuracy [13]. However, TR-DOS has depth selectivity because it discriminates between early and late photons in the histograms of the raw data [16]. This is an important feature in functional brain imaging for retrieving the absolute values of μ_s' and μ_a in multilayered objects such as a human head [10] [16] [53]. However, current TR-DOS requires complex, expensive equipment and costly computation to analyze the raw data [21] [61]. These requirements limit the use of TR-DOS systems for potential applications such as nondestructive optical characterization of food, wood, and for clinical applications such as muscle monitoring, functional brain imaging and optical mammography [21] [25]. Therefore, significant efforts are being made to simplify the complexity of TR-DOS systems to develop and utilize affordable instruments and to analyze the experimental data using efficient computational methods [21] [24] [25] [121]. As a result, it is expected that compact, low cost and portable multichannel TR-DOS systems will be available in the near future [21] [25] [83].

The main advances in reducing the cost and the size for instruments used for single-photon timing applications such as TR-DOS are achieved due to the recent developments in silicon photonics technologies [25] [131]. Using technologies such as the complementary metal-oxide-semiconductor (CMOS) silicon technology simplify the implementation and the fabrication for the solid-state detectors [21] [25] [177]. These detectors, mainly SPADs and SiPMs, are much smaller and cheaper than sophisticated traditional photon timing equipment such as Streak cameras, ICCD cameras, and PMTs detectors as shown in Figure 1-3 [21] [25].

Therefore, several CMOS SPAD detectors have been reported recently for single-photon timing applications, and some of them have been validated for TR-DOS applications [130] [154]. Although CMOS SPAD detectors have lower performance versus SPAD detectors based on custom silicon technologies, they have the potential to be used in building low cost and compact photon timing systems for tissue optics applications using several available options of standard CMOS technologies [25] [177]. Therefore, smaller dimensions CMOS technologies such as 130 nm, 90 nm, 65 nm can be utilized to miniaturize the size of SPAD arrays, and to integrate timing electronics

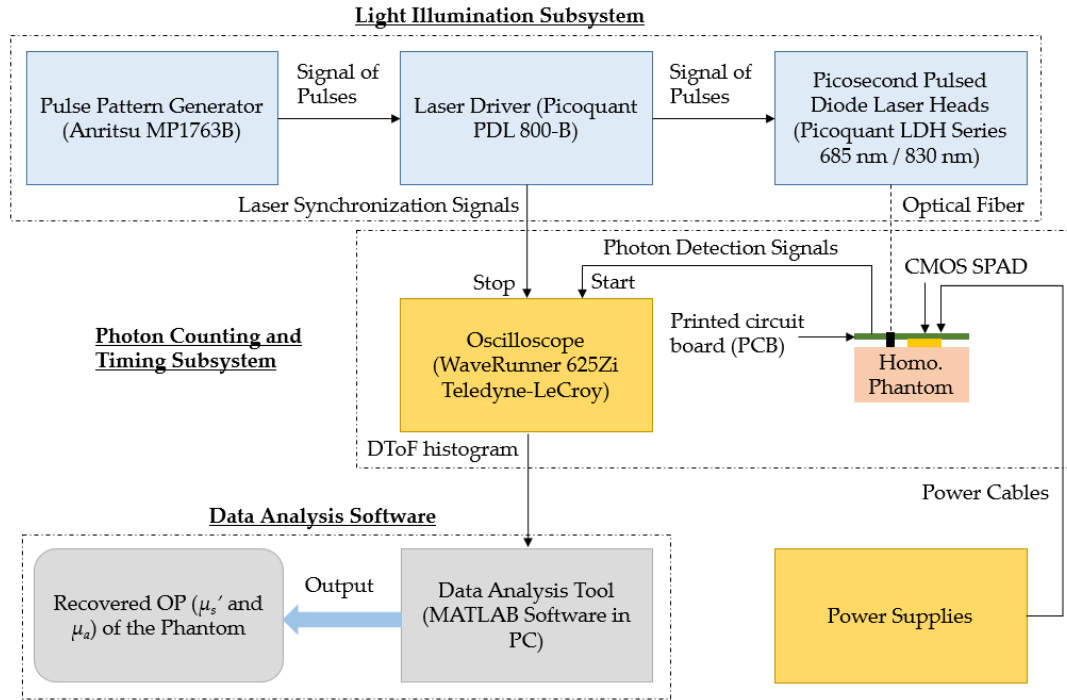
without significant degradation of the fill factor of the detector in comparison with larger dimensions CMOS technologies (800 nm and 350 nm) [178]. For instance, the fill factor of the SPAD detectors are in the range of 1%, 9%, and 25% for 800 nm 350 nm, and 130 nm CMOS technologies, respectively [179]. Towards this target, we have developed a compact **free-running (FR) single-photon avalanche diodes (SPADs)** in a standard, low-cost, digital 130-nm CMOS technology that builds on the previous works of our group on SPADs [125] [150] [180] [181] [182] [183].

In this Chapter, we built a TR-DOS prototype using our FR-CMOS SPAD detectors to investigate the importance of each performance feature for the FR-CMOS SPADs in TR-DOS measurements since some desired characteristics of the CMOS SPAD detectors need to be studied, as explained in Chapter 2 and our recent review [25]. The main desired characteristics of the CMOS SPAD detectors are low levels of noise (dark count rate and afterpulsing), short timing jitter, large fill-factor and good photon detection efficiency. When good performance features are achieved for one pixel SPAD detector, it is possible to replicate the pixel to build an array of SPADs [177]. Also, we report on a comprehensive evaluation of this TR-DOS prototype, and we demonstrate its capability when used for tissue optics applications. The evaluation of this prototype was achieved in two different levels that included the instrument performance and the quantification of the OP of realistic phantoms. Our prototype has a short total instrument response function (IRF_{Total}) and low **differential non-linearity (DNL)**. The accuracy assessments showed low average errors that were less than 10% for retrieving μ_s' and μ_a for several homogeneous phantoms. Also, this prototype demonstrates good linearity and can be used to estimate differences in the OP values among realistic phantoms.

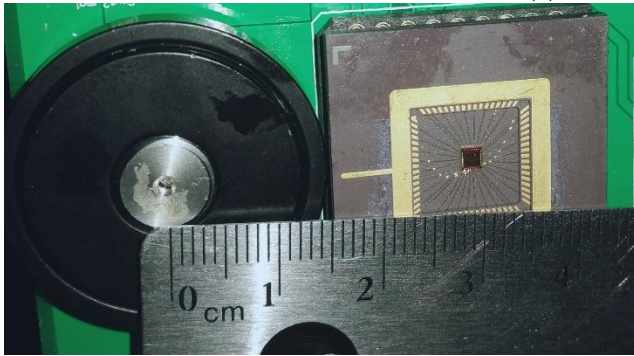
4.2. TR-DOS Prototype

The main components of this TR-DOS prototype can be classified into three parts. The first part is the light illumination subsystem-pulsed laser source and associated electronics. The second part is the photon counting and timing subsystem. These two parts represent the TR-DOS setup which generates raw data called the **distribution of time of flight (DToF)** histograms for the re-emitted photons from a phantom. The third

part is the data analysis software which preprocesses the DToF histograms and recovers the OP of the phantoms using a best-fitting model. Figure 4-1 illustrates the main components of the TR-DOS prototype.



(a)



(b)



(c)

Figure 4-1: (a) Diagram of main components of the TR-DOS prototype; (b) light source and detector arrangement (28 mm source-detector distance) that are attached to the surface of phantoms; and (c) a sample of the homogeneous phantoms.

4.2.1. Light Sources

Two picosecond pulsed diode laser sources are used to illuminate the phantoms at two wavelengths—685 and 830 nm—within the biological window [68]. These two chosen wavelengths of 685 and 830 nm are suitable to observe the concentrations for deoxy-hemoglobin (HHb) and oxyhemoglobin (HbO₂) in tissues, respectively [9]. The

maximum average optical power of the laser sources is ~ 10 mW [68]. A multi-mode optical fiber (four-meters long) is used to transmit light from each laser source to a phantom Figure 4-1 (a) [184]. An external pulse generator (MP1763B, Anritsu, Atsugi, Japan) is connected to the laser driver to trigger the laser sources with a repetition rate (RR) that can vary from 1 Hz to 80 MHz [185] [186]. Increasing the intensity and the repetition rate (RR, maximum is 80 MHz) for the laser driver increases the optical power of the light from the laser sources. The maximum average optical power of laser sources decreases by 5% to 15% due to the light losses through long optical fibers. Here, we used 50 MHz of RR of the pulses, that is, one laser pulse every 20 ns. This chosen RR allows the maximum average optical power of the illumination source to reach up to ≈ 6 mW if the highest intensity is used. This high RR increases the probability for detecting the re-emitted photons relative to the noise, thus improving the signal-to-noise ratio (SNR) of the measured DToF histograms.

4.2.2. Photon Counting and Timing Subsystem

The re-emitted photons from a phantom are collected by our custom designed FR CMOS SPAD detectors ($100 \mu\text{m}^2$ active area) in reflectance geometry [150]. In the excess voltages used ($V_{\text{ex}} = 1.2$ V), our detector has short timing jitter (< 150 ps), low dark count rate (DCR) ≈ 13 kHz at room temperature, and a photon detection efficiency (PDE) $\approx 0.6\%$ at 685 nm and $\approx 0.2\%$ at 830 nm [180]. Also, the dead-time of this detector is approximately $1 \mu\text{s}$ which allows for a maximum ≈ 0.5 million counts per second. The source to detector distance (SDD) between the fiber of the light source and the detector fixed at 28 mm, as shown in Figure 4-1 (b). The output signals of the FR CMOS SPAD and laser driver are connected to a Teledyne LeCroy oscilloscope (WaveRunner 625Zi, Teledyne LeCroy, Chestnut Ridge, NY, USA) to determine the delay between the edges of the two signals and record the photon time of arrival (PTA) for each detected photon [187]. Then, a DToF histogram can be performed by counting a reasonable number ($\sim 10^5$) of re-emitted photons.

4.2.3. Data Analysis Tool

We have developed an iterative inverse problem solver to preprocess the raw data (DToF histograms) and retrieve the OP of the measured phantoms based on MCXLAB

capabilities [86]. Figure 4-2 illustrates the steps of preprocessing and analyzing the raw data from the TR-DOS setup.

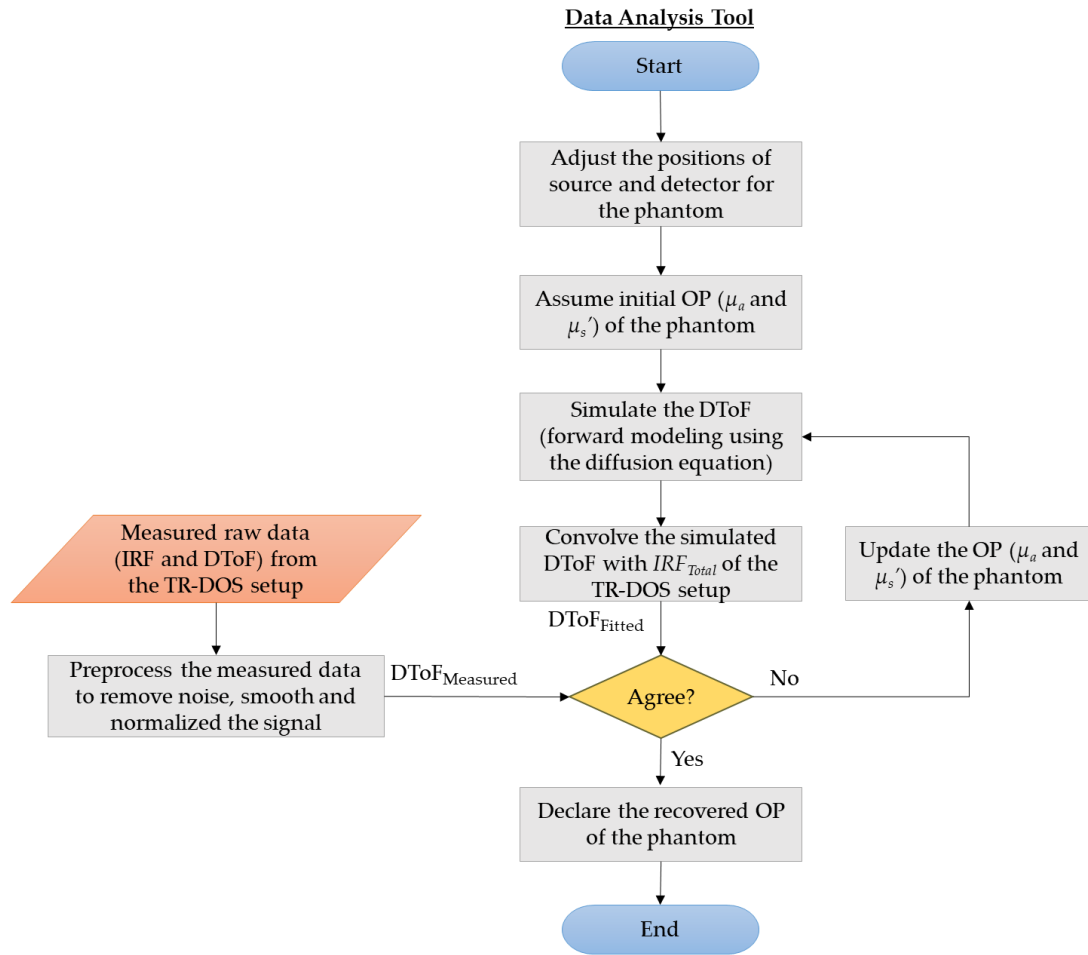


Figure 4-2: Flowchart of the data analysis process to recover the OP of the phantoms using the TR-DOS prototype.

This inverse problem solver uses an analytical solution of the **time-dependent diffusion equation (TD-DE)** for a semi-infinite medium to simulate the light propagation (the forward problem) and generate DToF histogram for each assumed μ_a and μ_s' of a phantom. Before analyzing the raw data using this best fitting model, three steps of preprocessing are performed in sequence - noise removal from the signal, smoothing, and normalizing the DToF curve. In each iteration, the simulated DToF histogram is convolved with the IRF_{Total} of the TR-DOS setup to give a fitted DToF histogram. Then, the fitted DToF histogram (already convolved with IRF_{Total}) is matched to the experimentally measured DToF using a nonlinear least square solver (the Levenberg-Marquardt method). The iterative process starts with adjusted initial

values of μ_s' and μ_a that are typical of human tissues: $\mu_s' = 1.0 \text{ mm}^{-1}$ and $\mu_a = 0.01 \text{ mm}^{-1}$ [188] [189]. Other OP parameters such as the anisotropy factor ($g = 0.9$) and the refractive index ($n = 1.5$) are kept constant while the iterative process is running. Then, the iterative process continues until the inverse problem solver finds the best solution of the objective function.

4.3. Characterization Methods

We evaluated the performance of our prototype using assessments based on two well-known protocols. The first protocol is the **basic instrumental performance** (BIP) that focuses on the characterization of the TR-DOS setup and its equipment without considering a measuring object (such as a phantom) [105]. The second protocol is MEDPHOT which evaluates the capability of TR-DOS prototype to recover the OP for homogeneous phantoms [106]. In this Section, we describe the concepts and the experiments to characterize our TR-DOS prototype.

4.3.1. Basic Instrumental Performance Protocol

Following the BIP protocol, three parameters of the TR-DOS setup are measured. These parameters are the average delivered optical power on the phantoms (P_{Source}) from the laser source, the **differential non-linearity** (DNL), and the total Instrument Response Function of the setup (IRF_{Total}) [105].

Light Power

An optical power meter (Model 1830-C, Newport, Irvine, CA, USA) was used to measure the power of the light from the fiber that transmits light from laser sources to phantoms [190] [191]. Measurements were taken for both light sources with the same repetition rate (50 MHz) that were used to illuminate the phantoms. The illuminated areas (A_{source}) on the surface of the phantoms were $\approx 3 \text{ mm}^2$ for both light sources. The optical powers of the delivered light to the phantoms were 2.2 mW and 3.6 mW for the 685 nm and 830 nm laser sources, respectively. These levels of optical power are much lower than the **maximum permissible exposure** (MPE) for human skin. The MPE levels for skin are estimated as $6 \text{ mW}/A_{source}$ (3 mm^2) for 685 nm and $11 \text{ mW}/A_{source}$ (3 mm^2) for 830 nm laser beams. At each wavelength, we calculated the MPE according to

the data acquisition time in the experiments (20 min for each phantom) using formulas reported in the literature [69].

Differential non-linearity (DNL) of Photon Timing

The **differential non-linearity (DNL)** is mainly used to estimate the non-uniformity of the width of the time bins in the photon timing equipment such as **time-to-digital converter (TDC)** or **time-correlated single photon counting (TCSPC)** [105]. The DNL is a routine test that is required for TR-DOS systems even if the **photon time of arrival (PTA)** is measured using different equipment such as an oscilloscope. Ideally, the counted photons in each bin in the histogram should be equal [105]. However, during the experiments, there are differences in the distribution of the counted number of photons as a result of the DNL. We measured the DNL using a pulse pattern generator to send repetitive signals (50 MHz) as the start signal to the oscilloscope, and the FR CMOS SPAD to count photons and send the stop signal to the oscilloscope. It is worth noting that to measure the DNL, a battery-powered light source to illuminate the detector to prevent any electrical power-line interference is recommended [105]. Also, we placed **neutral-density (ND)** filters between the light source and CMOS detector to attenuate ($\sim 95\%$) the light and prevent saturation of the detector. An optical bandpass filter (680 nm) was used to allow only light at the required wavelength to reach the detector. Figure 4-3 illustrates the experimental setup for DNL measurements. It is recommended to measure PTA for more than 10^5 counted photons in each time bin to obtain a good SNR and more accurate estimation of the ϵ_{DNL} using the following equation [105]:

$$\epsilon_{DNL} = \frac{N_{DNL,max}(t) - N_{DNL,min}(t)}{\overline{N_{DNL}}} \quad (4.1)$$

where $N_{DNL, max}$ and $N_{DNL, min}$ are the maximum and the minimum number of recorded photons in the time bins (maximum peak to minimum peak). $\overline{N_{DNL}}$ is the average number of counted photons in time bins.

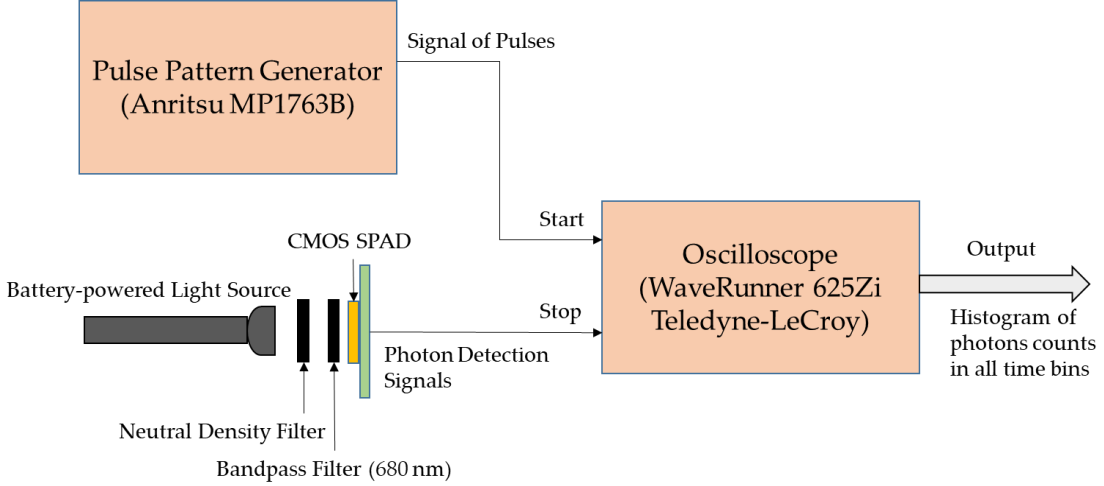


Figure 4-3: DNL measurement setup to acquire histograms of the PTA for all detected photons.

Total IRF of the TR-DOS Setup

The IRF_{Total} is an important performance measure for TR-DOS systems, and the full-width-at-half-maximum (FWHM) of the IRF_{Total} should be as short as possible, especially if short source-detector separations are used. Moreover, the FWHM of IRF_{Total} must be less than 1.0 ns so as not to distort the raw data (DToF histograms) [120] [75]. The FWHM of IRF_{Total} represents the root of the sum of squared IRF for each instrument such as laser source, photon detector (timing jitter of the CMOS SPAD), optical fiber and photon timing equipment (WaveRunner 625Zi, Teledyne LeCroy, Chestnut Ridge, NY, USA) in our TR-DOS setup. The FWHM of IRF_{Total} of this TR-DOS setup is given by [25]:

$$FWHM \text{ of } IRF_{Total} \approx \sqrt{IRF_{laser \ source}^2 + IRF_{OpFb}^2 + IRF_{CMOS \ SPAD}^2 + IRF_{Oscilloscope}^2} \quad (4.2)$$

To measure the FWHM of IRF_{Total} of the TR-DOS setup, the optical fiber connected to the laser source is placed in front of the CMOS SPAD detector, and a thin diffuser such as a sheet of white paper was used between the fiber and the detector to ensure scattering of the light [120] [105] [192]. Multiple scattering interactions happen for photons in the thin diffuser that vary the directions of detected photons with a negligible broadening of the measured FWHM of IRF_{Total} [105].

4.3.2. Optical Properties Quantification of Homogeneous Phantoms

Following the MEDPHOT protocol, we used two assessments such as accuracy and linearity to characterize the OP for several homogeneous phantoms using the TR-

DOS prototype. The measured DToF histograms (raw data) were preprocessed to remove the noise and smooth the DToF curves. After that, the measured DToF histogram for each phantom was analyzed using the best fitting model to estimate the OP of the phantom as described earlier in Section 4.2.3.

Accuracy Assessment

The accuracy of the OP quantification is determined by comparing the true OP of the phantoms with the recovered OP. The accuracy of the retrieved μ_s' and μ_a is estimated separately for each phantom by calculating the error using the following equation [106]:

$$\varepsilon = \frac{OP_{recovered} - OP_{true}}{OP_{true}}. \quad (4.3)$$

The result from Equation (4.3) ε is converted to a percentage, determines the discrepancy in accuracy assessments.

Linearity Assessment

The linearity test focuses on the changed values of the retrieved μ_s' or μ_a when the true μ_s' or μ_a are varied. The main sources of inaccuracies in the retrieved μ_s' or μ_a are from three factors [49]. First, there are some small fluctuations of the time origin (t_0) from one measurement to another, and these fluctuations have impacts on the accurate estimation of the OP, particularly μ_s' . Second, there is a systematic distortion of the measured DToF histograms due to the impact of the *IRF* and the noise (background and false triggering). Third, there is some error in the theoretical approximations when the diffusion equation (DE), which is less accurate than the radiative transfer equation (RTE), is used simulate the light propagation in diffusive media [49] [100].

Preparation of Phantoms

To perform accuracy and linearity assessments, sets of nine homogeneous solid cylindrical phantoms were prepared for the measurements. The phantoms have three μ_a (0.005 mm^{-1} , 0.009 mm^{-1} and 0.013 mm^{-1}) and three μ_s' (0.4 mm^{-1} , 0.8 mm^{-1} and 1.2 mm^{-1}) values. These phantoms are named according to their OP using letters for variable μ_s' (A, B, and C) and numbers for variable μ_a (1, 2, and 3). Thus, the OP for phantom A1 are almost 0.005 mm^{-1} and 0.4 mm^{-1} , and the OP for phantom C3 are almost 0.013 mm^{-1} and 1.2 mm^{-1} for μ_a and μ_s' , respectively. The range of OP for these phantoms has been chosen to be in the range of the known OP of human tissue [193].

The height of each phantom is 27 mm, and the diameter is 67 mm, as shown in Figure 4-1 (c).

Phantoms were prepared using epoxy-resin, titanium dioxide (TiO_2), and India ink for the phantom matrix media, scattering agent and absorbing agent, respectively [74]. The concentrations of TiO_2 and ink were varied linearly to produce changes of about 0.005 mm^{-1} and 0.4 mm^{-1} (at the wavelengths range between 685 nm and 830 nm) for μ_a and μ_s' , respectively. The TiO_2 was suspended in an ethanol solution (ratio is 1 gm TiO_2 / 3 ml ethanol) to ensure good mixing with the resin. To determine the required TiO_2 and ink concentrations to produce specific OP of phantoms, we used a steady-state spatially resolved diffuse reflectance system with a custom-made inverse problem solver that was described in Chapter 3 and our previous work [175]. After fabricating the phantoms, the surfaces were polished using several sandpapers (grits vary from 120 to 600) to remove scratches. Then, we estimated the actual OP for each phantom using our time-resolved diffuse optical tomography system [175]. Table 4.1 summarizes the actual OP of the used phantoms in this Chapter at the used two wavelengths 685nm and 830 nm.

Table 4.1: The nominal OP of the measured phantoms.

Phantom	685 nm		830 nm		n
	μ_s' (mm^{-1})	μ_a (mm^{-1})	μ_s' (mm^{-1})	μ_a (mm^{-1})	
A1	0.41	0.0047	0.4	0.0049	1.5
A2	0.41	0.0083	0.4	0.0088	1.5
A3	0.41	0.0124	0.4	0.0131	1.5
B1	0.81	0.0047	0.78	0.0049	1.5
B2	0.81	0.0083	0.78	0.0088	1.5
B3	0.81	0.0124	0.78	0.0131	1.5
C1	1.23	0.0047	1.17	0.0049	1.5
C2	1.23	0.0083	1.17	0.0088	1.5
C3	1.23	0.0124	1.17	0.0131	1.5

Data Acquisition and Preprocessing

To measure the DToF histogram for each phantom, laser light is injected to the phantom, and the re-emitted photons are detected in reflectance geometry using an identical source to detector distance (SDD) of 28 mm. Each measurement is done for

20 min until the DToF histogram was acquired and around 600 K photons and background noise signal were counted. It is worth noting that this long time for data acquisition is not necessary since 200 s of data acquisition time is enough to count $\approx 10^5$ events (photons and noise). In our experiments, this slow photons timing process is a result of the limited update rate of the oscilloscope for the time base (20 ns) used. This slow update rate allows only for recording a small portion of the counted photons and noise from the SPAD detectors (~ 500 counts per second), whereas the maximum count rate of our SPAD detectors is up to ~ 0.5 million counts per second. Therefore, using a longer data acquisition time (20 min) is useful to increase the number of the counted photons to acquire smoother DToF curves to more accurately retrieve the OP.

On the other hand, to use this prototype in real-time applications, the SPAD detectors should be connected to TDCs or a TCSPC module to acquire a raw data histogram and count $\geq 10^6$ photons within a few seconds. In this Chapter, all the acquired DToF histograms have 20 ns range, and 1000 time bins (width of each bin is 20 ps). These measurements were taken three times (at different positions on the surface for each phantom) using two laser sources at 685 and 830 nm. Figure 4-4 shows the DToF histograms that were measured for high scattering phantoms and high absorption phantoms at 685 nm and 830 nm, and the corresponding IRF_{Total} . In these Figures, the variation of the dynamic range between the IRF_{Total} and the measured DToF curves can be observed. The DCR (~ 13 kHz) of the detector versus the maximum count rate (500 K) restricts the dynamic range of this prototype to be 1.7 orders of magnitude for high-intensity light in the IRF_{Total} measurements. This maximum level of the DR is lower than the reported dynamic range for FR-TR-DOS systems by one order of magnitude [154]. The limited DR for our TR-DOS systems is a result of a relatively high percentage DCR ($\sim 2.5\%$ of the maximum count rate) and the modest PDE of the SPAD detectors used. Therefore, it is noticed that the DToF curves have a lower order of magnitude of the DR due to the lower intensity of the measured light in DToF measurements.

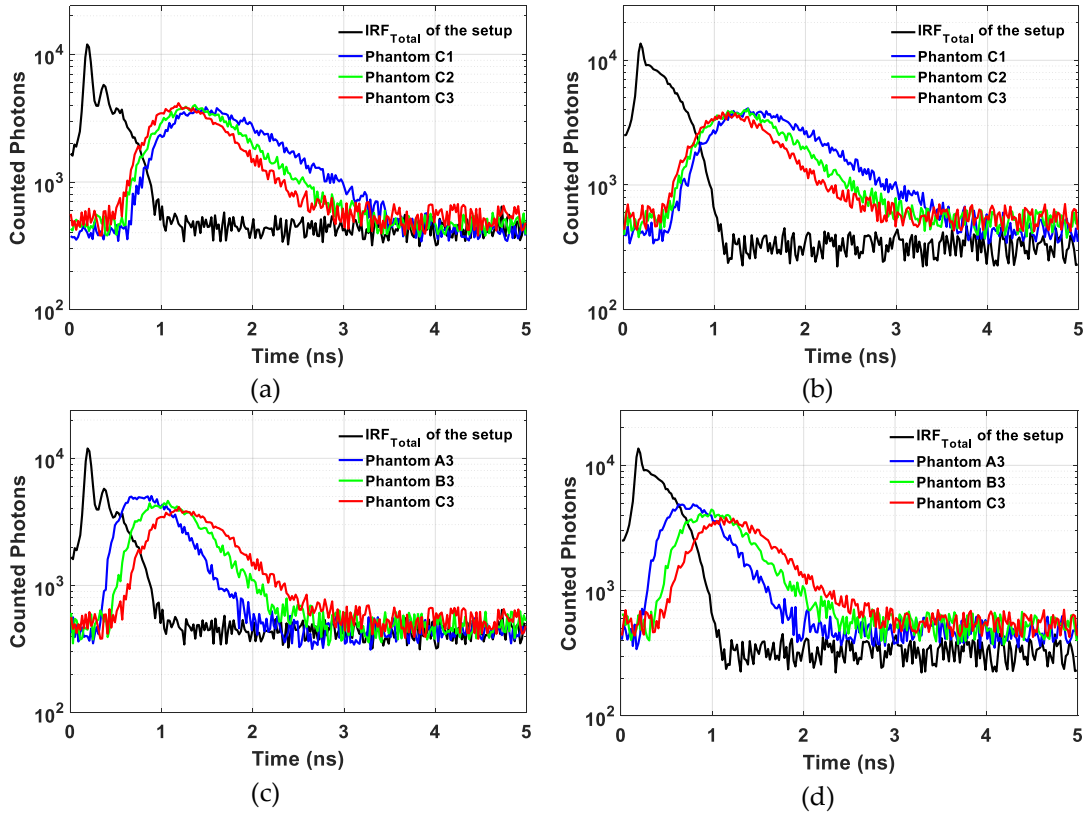


Figure 4-4: The IRF_{Total} versus the measured DToF histograms for the phantoms: (a) high scattering phantoms with variable μ_a at 685 nm; (b) high scattering phantoms with variable μ_a at 830 nm; (c) high absorption phantoms with variable μ_s' at 685 nm; and (d) high absorption phantoms with variable μ_s' at 830 nm.

To prepare the DToF histograms for analysis, noise such as DNL distortion is removed from the signals. After that, each DToF curve is smoothed using a moving average filter for a span of seven time bins (representing 140 ps). The last step of preprocessing is the normalization for each DToF before starting the best fitting model process, as illustrated earlier in Figure 4-2. We compared the results (for the OP quantification) for different ranges of points in the DToF histograms that are involved in the best fitting process. Then, we chose the range of points from 60% of the DToF curve peak in the rising edge and 15% of the DToF curve peak in the falling tail because the most accurate OP quantification results were obtained using this range. Figure 4-5 shows an example of the fitting process for the same phantom (B2) at both wavelengths used. The time in the x-axis represents the delay between the DToF curve and the rising edge of the IRF_{Total} (0 ps).

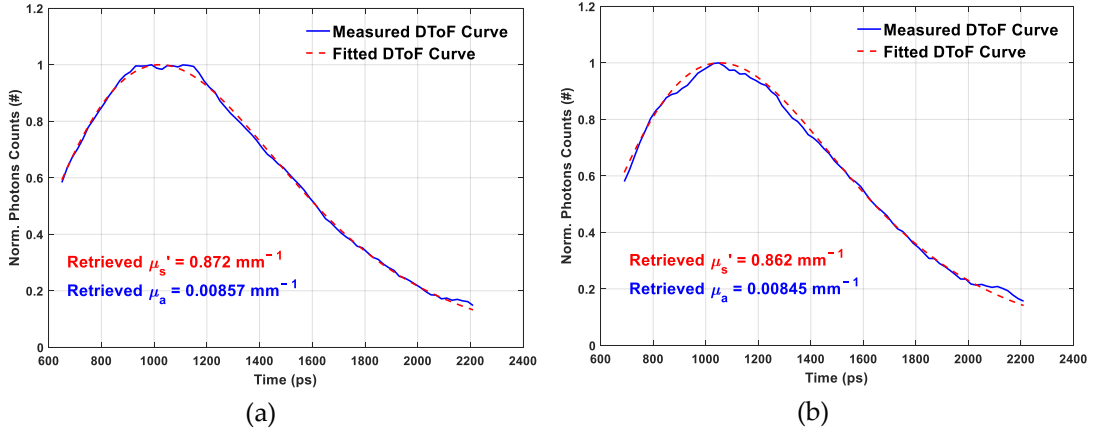


Figure 4-5: DTof_{Measured} curves and DTof_{Fitted} curves for B2 phantom with SDD = 2.8 cm: (a) at 685 nm; and (b) at 830 nm.

4.4. Results and Discussions

Several measurements were taken to characterize the TR-DOS prototype following the BIP and MEDPHOT protocols. In this Section, we report and discuss the results of the following assessments: DNL, IRF_{Total} , accuracy, and linearity. Then, we evaluate this prototype and describe its limitations.

4.4.1. Differential Non-Linearity

In the DNL measurements, 10^7 photons were counted for all time bins (1000 bins and width for each bin is 20 ps). In Figure 4-6, the histogram of PTA distributions that was used to calculate the DNL is shown. The ϵ_{DNL} was estimated to be 0.073 (7.3%) using Equation (4.1) and the measurement setup illustrated in Figure 4-3. This level of error is acceptable because the level of DNL error is normally several percent ($< 10\%$) [105]. It is worth noting that if the error of DNL exceeds 10%, a correction of DNL should be used [75] [83] [105]. However, no correction of the DNL is required for this TR-DOS system because the DNL result indicates that the oscilloscope performs the time-to-digital conversion (for the counted photons) with a slight distortion of the width for time bins.

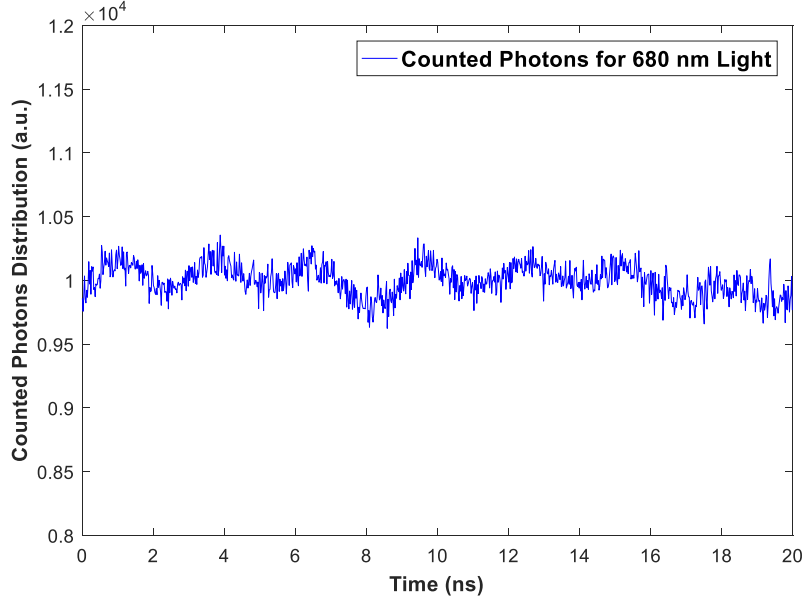


Figure 4-6: Histogram of PTA distributions for 10^7 counted photons in all time bins (1000 bins for 20 ns range).

4.4.2. Total Instrument Response Function

The narrowest FWHM of IRF_{Total} in each wavelength is less than 120 ps for low-power light are shown in Figures 4-7 (a) and (b). However, we used a higher power to illuminate the phantoms, which is essential to eliminate the impact of the CMOS SPAD's modest PDE and the small active area. At a higher power level, the width of pulses for the picosecond diode laser is increased significantly, which leads to broadening of the FWHM of IRF_{Total} of the TR-DOS setup [25] [68]. Therefore, the temporal widths of IRF_{Total} are broadened to 120 ps and 350 ps using 685 nm and 830 nm laser sources, respectively. Figure 4-7 shows the IRF_{Total} (shown in log scale) that were measured at both wavelengths of 685 nm and 830 nm versus the shapes of the pulses of the light sources (shown in linear scale). In these subfigures, the short timing jitter of the CMOS SPAD detector used makes it possible to produce accurate IRF_{Total} signals that have similar shapes to the pulses of the light sources at different optical power.

An accurate determination of the FWHM of IRF_{Total} is essential because it will be convolved with the simulated DToF (from the forward modeling) to perform the fitted DToF ($DToF_{Fitted}$) as follows [49] [62] [194]:

$$DToF_{Fitted} = DToF_{Simulated} * \text{FWHM of } IRF_{Total} \quad (4.4)$$

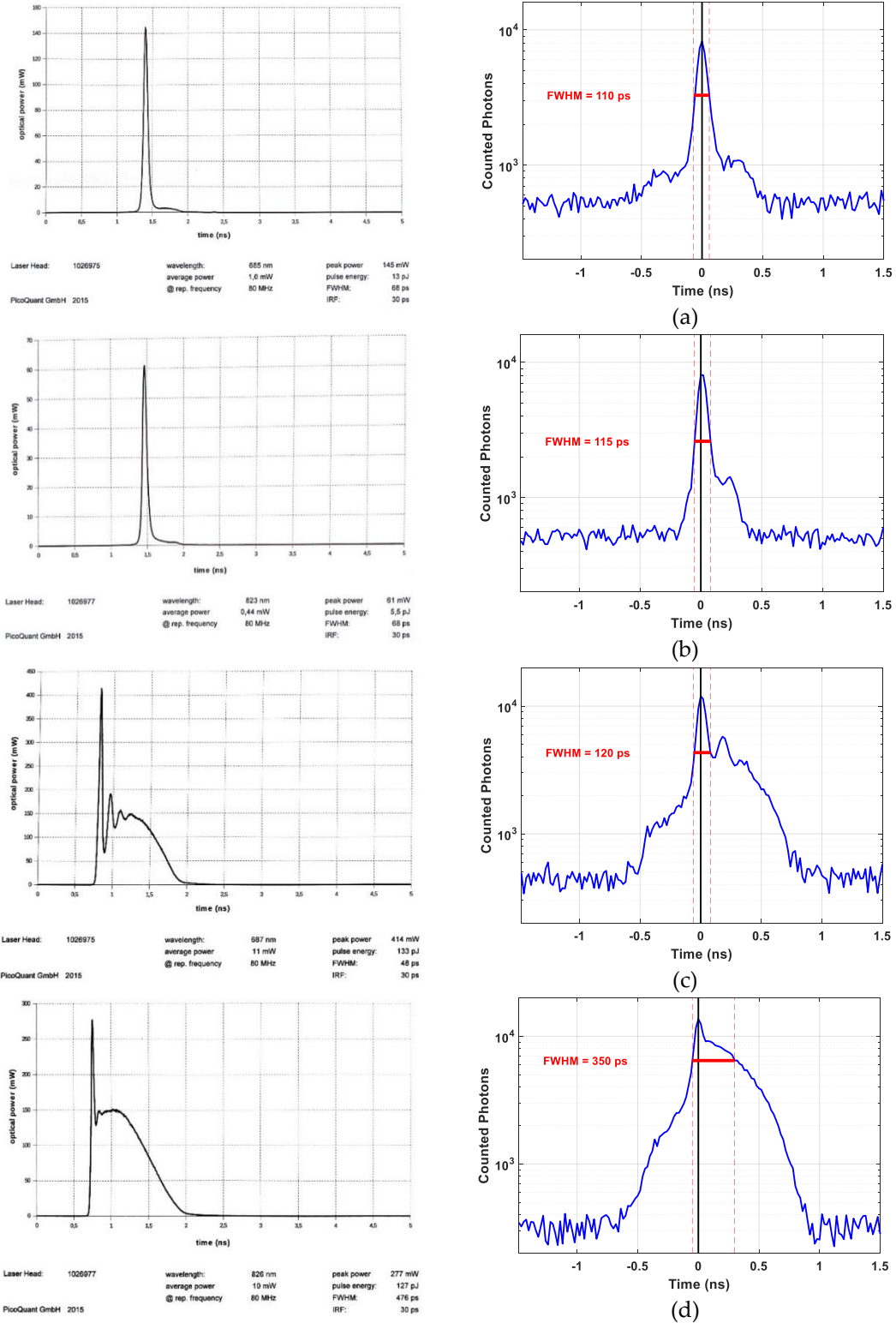


Figure 4-7: FWHM of IRF_{Total} of the TR-DOS prototype at two different wavelengths used in this Chapter: (a) 685 nm at low optical power (0.05 mW); (b) 830 nm at low optical power (0.06 mW); (c) 685 nm at the used optical power (2.2 mW) to illuminate the phantoms; and (d) 830 nm at the used optical power (3.6 mW) to illuminate the phantoms.

4.4.3. The Accuracy of the OP Quantification

In the accuracy assessment, we estimated the percentage of error for the recovered OP against the actual OP for each phantom. Table 4.2 shows the results of accuracy assessments for all nine phantoms at the two wavelengths. The percentage of errors were estimated using Equation (4.3), and the average of errors were 6.5% and 9.5% for μ_s' and μ_a , respectively. These levels of error in OP quantification is a known limitation for DOS techniques [49] [100] [194]. The highest discrepancy for μ_s' appeared in the phantom (A3) at 685 nm and phantom (A2) at 830 nm that reached up to 12% and 19%, respectively. The main reason for these errors comes from the difficulty in discriminating changes in the shapes of the DToF curves for low μ_s' turbid media [100]. Also, the percentage errors for the retrieved μ_s' have increased for low scattering phantoms (A) due to the low values of μ_s' , as shown in Table 4.2. On the other hand, the average discrepancy for retrieved μ_a decreases significantly at 685 nm in high μ_s' phantoms (C). Overall, the estimated accuracy for homogeneous phantoms using this prototype is similar to the reported levels of accuracy of TR-DOS measurements for prototypes that use commercial detectors [62] [106] [173].

Table 4.2. Relative errors in the accuracy assessment of the retrieved μ_s' and μ_a versus the actual μ_s' and μ_a for nine phantoms at two different wavelengths.

		% Errors in the estimate of μ_s'			% Errors in the estimate of μ_a		
685 nm Results		μ_s'					
μ_a		A (0.41)	B (0.81)	C (1.23)	A (0.41)	B (0.81)	C (1.23)
1 (0.0047)		10.5	9.5	1.6	19	17	0
2 (0.0083)		3.5	7.5	5.7	7.2	3.6	8.4
3 (0.0124)		12	-1.2	0	-3.2	-9.7	-3.2
830 nm Results		μ_s'					
μ_a		A (0.4)	B (0.78)	C (1.17)	A (0.4)	B (0.78)	C (1.17)
1 (0.0049)		1.3	5.8	6.8	-12.2	-8.2	-4
2 (0.0088)		18.8	10	4.3	6.8	-4.5	-10.2
3 (0.0131)		6.3	7.7	3	-23.7	-12.2	-16

4.4.4. The Linearity of the OP Quantification

The TR-DOS prototype has presented good linearity for retrieving μ_s' with some overestimation for all nine phantoms at both wavelengths Figures 4-8 (a) and (b). In

addition, the prototype has shown good linearity for retrieving μ_a for phantoms B and C in both wavelengths with some underestimation at 830 nm Figures 4-8 (c) and (d). On the other hand, better linearity was obtained for the retrieved μ_a for low μ_a phantoms (1) versus high μ_a phantoms (2 and 3). This is a result of the reduction in the absorption-to-scattering coupling at both wavelengths Figures 4-8 (e) and (f). Also, the results show good linearity for the retrieved μ_s ' for all phantoms which indicate low scattering-to-absorption coupling as shown in Figures 4-8 (g) and (h). Generally, the linearity of this TR-DOS prototype is very good and comparable to the reported linearity results in the literature [62] [106] [108] [173] [195].

4.4.5. Evaluation of this Prototype and the Potential Applications

The evaluation of this TR-DOS prototype has demonstrated good performance, and it can be used for tissue optics applications for the following reasons. First, the chosen optical power of the illuminated light (much lower than MPE of skin) were useful to overcome the modest PDE and the small active area of the detector by increasing the number of injected photons and accordingly increasing the number of detected photons. Second, the low errors for DNL and the narrow IRF_{Total} verified that raw data (DToF histograms) could be generated with good accuracy (without distortion) for human tissues such as muscle, breast or a newborn's head. However, the long time for data acquisition and the modest dynamic range (one order of magnitude) for DToF curves, as shown in Figure 4-4, are limitations in the use of this prototype for some tissue optics applications such as functional brain imaging. Therefore, it is necessary to develop high temporal resolution TDC and integrate it with this FR CMOS SPAD detector to reduce the data acquisition time to the range of few seconds. This will enable this prototype to observe physiological changes (such as blood oxygen saturation) in tissue which happen within seconds.

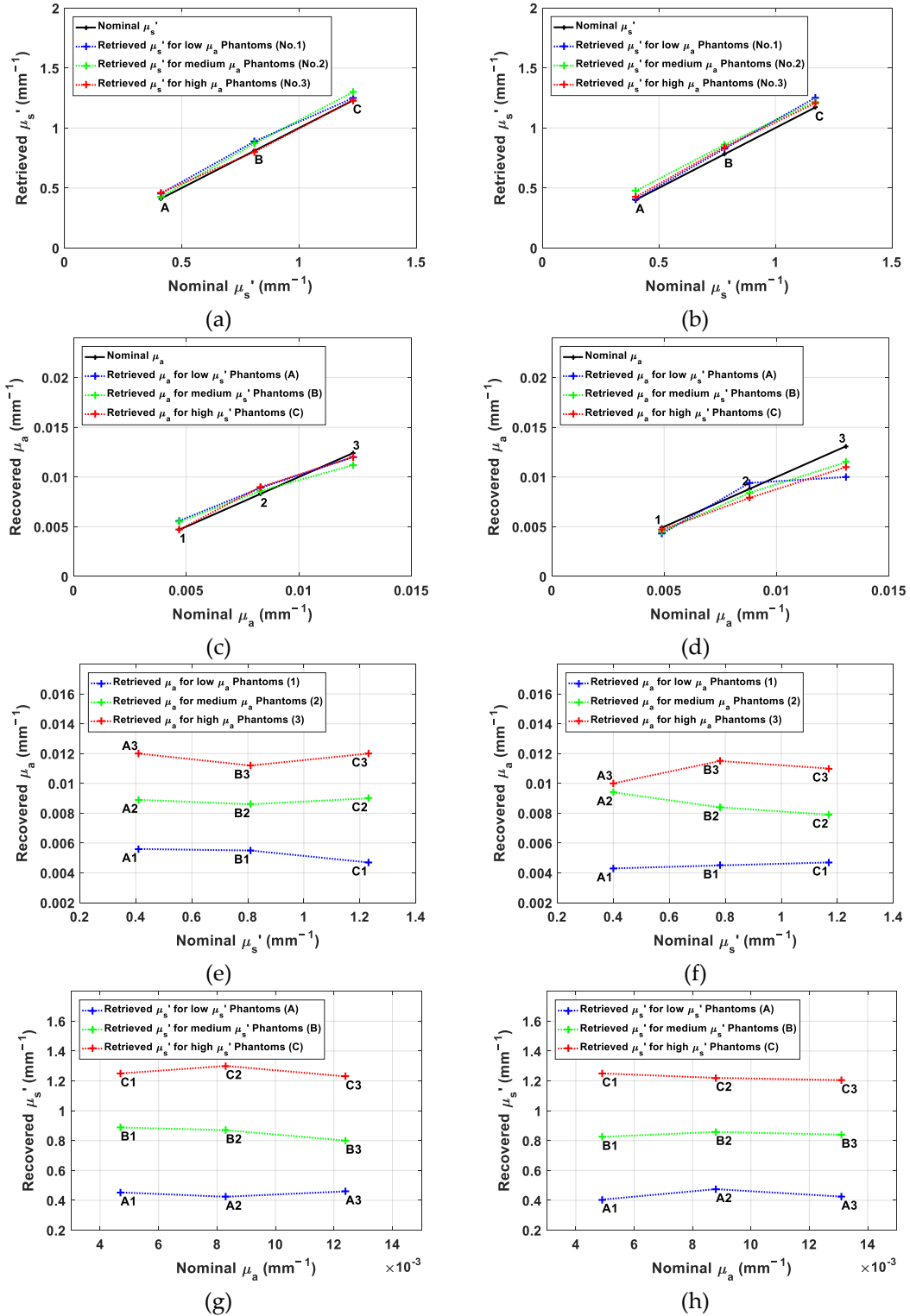


Figure 4-8: The linearity of the retrieved OP versus the actual OP for nine phantoms at two different wavelengths: (a) and (b) represent the retrieved μ_s' against the actual μ_s' at 685 and 830 nm, respectively; (c) and (d) represent the retrieved μ_a against the actual μ_a at 685 and 830 nm, respectively; (e) and (f) represent the retrieved μ_a against the actual μ_s' at 685 and 830 nm, respectively; and (g) and (h) represent the retrieved μ_s' against the actual μ_a at 685 nm and 830 nm, respectively.

Fast data acquisition time is not expected to improve the dynamic range significantly due to the low PDE, and the small active area for the detector used. Therefore, this prototype will probably not be capable of observing the change of the OP in the deep regions in multilayered tissue such as gray matter and white matter in an adult's head. Here, the OP mainly depend on the late photons in DToF curves and require a fast time gating detection capability. Third, the results of accuracy and linearity assessments indicated that this prototype could be used to distinguish between pathological tissue and healthy tissue due to the noticeable OP variations between them. Overall, there are some potential improvements that can be achieved to design better FR SPAD detectors in 130 nm CMOS for TR-DOS applications.

4.4.6. Potential Developments of SPAD Detectors for Tissue Optics Applications

The SPAD detectors used here have demonstrated good performance in TR-DOS measurements. However, there are some issues that should be considered when SPAD detectors are being designed (particularly in 130 nm CMOS) to improve their performance and overcome some limitations for TR-DOS. The important FR-CMOS SPAD features in TR-DOS measurements are as follow.

1. The most important features for each designed pixel are short timing jitter and low noise sources such as the DCR and after-pulsing. Increasing the size of the active area and the thickness of the depletion region increases the PDE of the detector. However, the size of the active area for each pixel and the thickness of the depletion region should not be enlarged too much to avoid increasing the timing jitter and noise. For instance, in this Chapter, short timing jitter of the detector used enables the TR-DOS system to achieve short IRF_{Total} that was sensitive to the width and the shape of the pulses of the laser sources at different optical powers. Also, short IRF_{Total} is important to achieve good accuracy for retrieving the OP in TR-DOS applications.
2. Reducing the dead time is desirable if we want to increase the count rate for each CMOS pixel and avoid saturation of the detector when many photons are impinging on the active area during a relatively long dead time. However, the typical dead time for CMOS SPAD pixels (tens of ns up to few μ s) is enough to count more than 10^5 photons/s. This count rate of photons is compatible with TCSPC modules and

- TDCs units that suffer from pile-up effect if the count rate of photons exceeds 5% of the RR of the reference signal such as the laser repetition rate in TR-DOS systems [137].
3. The impact of a modest PDE of the CMOS SPAD pixels can be eliminated by increasing the optical power of the illuminated light and using a small SDD (1 cm–3 cm).
 4. Using an array of SPAD pixels is vital to enlarge the total active area of the SPAD detectors and increase the number of counted photons in TR-DOS measurements, especially when a larger SDD (> 3.0 cm) is used. However, a large number of an array of SPAD pixels is not necessary to increase the number of the counted photons since each TDC will be shared by several pixels to avoid reducing the fill factor of the pixels. Sharing TDCs by a large number of pixels will ultimately lead to an increase in the data acquisition time and keep a limited number of the array's pixels active during the measurements. Therefore, a CMOS SPAD detector with a reasonable number of pixels (~ 100) such as in a 1 D array or a 2 D array (10×10), where each pixel has an independent TDC, can be useful for TR-DOS measurements using illuminated light with optical power lower than the MPE of the skin. For a TR-DOS, a 1 D line array of pixels is preferable to keep the pixel electronics outside the pixel to increase the fill factor of the SPAD detectors [177].
 5. To maintain a good level of SNR, SDD should be reasonable (≤ 4 cm) in TR-DOS measurements without exceeding the MPE of the light for the skin. Otherwise, the DR of the measured DToF curves will be significantly degraded, and the measured DToF curves will not be valid to recover the OP for the measured object.
 6. Another possible approach to improve the achievable DR of the TR-DOS prototype is to reduce the percentage of DCR versus the maximum count rate. Therefore, from our perspective, we believe that a TR-DOS prototype using FR CMOS SPAD detectors with DCR lower than 0.1% of the maximum count rate can acquire DToF with DR higher than two orders of magnitude. Such a TR-DOS prototype will achieve better depth sensitivity to recover the OP for deeper regions in tissues (e.g. detecting a blood clot in brain, and a cancer tumor in breast).

4.5. Conclusions

In recent years, significant efforts were made to reduce the complexity, cost and size for time-resolved diffuse optical spectroscopy (TR-DOS) systems. Here, we described and characterized a TR-DOS prototype using low cost, compact, custom-designed free-running (FR) single-photon avalanche diode (SPAD) detectors in standard silicon 130 nm CMOS technology. This prototype was used to successfully perform distribution of time of flight (DToF) histograms in reflectance geometry for phantoms that have optical properties (OP) in the range of human tissues. The detector was used to acquire histograms using a low-power pulsed laser light with power levels below the maximum permissible exposure for human skin. The differential non-linearity was acceptable (7.3%) for photon timing with a temporal resolution in the range of tens of picoseconds, which is required for TR-DOS systems. The temporal widths of the total instrument response function of TR-DOS prototype were short enough to ensure that DToF histograms are not distorted and valid to be used to quantify the OP of homogeneous phantoms accurately. The results of the accuracy assessment for quantifications of the OP were very good for the realistic phantoms used, and the levels of error are within the range of results reported in the literature. The results of the linearity assessment demonstrate the potential of the prototype to observe the differences of the OP among several homogeneous phantoms.

However, the long time for the data acquisition is a limitation of this TR-DOS prototype, but it can be shortened significantly by incorporating time-to-digital converters with the SPAD detectors on the same chip to perform the DToF histograms. Then, multichannel TR-DOS can be built using several low-cost photon-timing subsystems with FR silicon SPADs with TDCs in the same chip. Such a system would be very suitable for clinical applications such as functional newborn brain and muscle monitoring and optical mammography, particularly if the possible improvements of the SPAD detectors are used.

Chapter 5

TIME-GATED TIME-RESOLVED DIFFUSE OPTICAL SPECTROSCOPY PROTOTYPE FOR MULTILAYERED TURBID MEDIA

In Chapter four, the low dynamic range (DR) is an important limitation in using the FR-TR-DOS prototype to generate valid raw data for multilayered objects such as adults' heads. Therefore, it is difficult to use this FR-TR-DOS prototype (mentioned in Chapter 4) to quantify the OP for deep regions in multilayered objects. Therefore, in this Chapter, we report on a custom-designed fast-gated CMOS SPAD detector used to build a TG-TR-DOS system with a higher DR than that reported for the FR-TR-DOS system in Chapter four. For this purpose, a novel reconstitution algorithm was implemented to preprocess the DToF curves of gates and preform full DToF. In this Chapter, the TG-TR-DOS system and the reconstitution algorithm will be described and evaluated in the following order. In Section 5.1, a brief explanation of the concepts and benefits of using TG measurements in diffuse optics applications is given. Then, the architecture of the TG-TR-DOS prototype and the equipment used are described in Section 5.2. In Section 5.3, the implemented algorithm to reconstitute full DToF from several measurements of the gates is described and validated with simulation results. In Section 5.4, the reconstituted full TG-DToF curves are compared with FR-DToF curves that are acquired by state-of-art SPAD detectors for a multilayered object, an *ex vivo* animal head.

5.1. Introduction

High dynamic range (DR) of the Measured DToF is an essential requirement in TR-DOS applications to increase the depth sensitivity and recover the OP for deep regions in multilayered turbid media [84]. With a high DR for TR-DOS system, late counted photons reach deep regions in the measured objects such as gray matter and white matter in a human brain [196]. Two approaches can be used to increase the DR of the measured DToF for TR-DOS systems. First, is to use sophisticated, expensive and large photodetectors or cameras such as ICCD cameras, streak cameras, and SPAD detectors (fabricated in custom silicon technology). Second, low-cost and compact ultra-fast time gating capabilities for CMOS SPADs detectors can be used. The first approach is not compatible with the aims to reduce cost, size, and complexity of TR-DOS systems. Therefore, the second approach is attractive due to the flexibility of CMOS technology to implement and fabricate low-cost and compact TG SPAD detectors with varying performance characteristics [84] [196]. However, TG-TR-DOS measurements are more complicated than FR-TR-DOS measurements because of the necessity for accurate synchronization of between the re-emitted photons and the detector's gates (see Figure 2-13) [84] [196] [197]. Also, TG-TR-DOS measurements require intensive data preprocessing to reconstitute a full TG-DToF curve for multiple signals of the gates used [197]. Therefore, in this Chapter, a TG-TR-DOS prototype is integrated to count the re-emitted photons using several synchronized gates. Also, a reconstitution algorithm was developed to acquire the full TG-DToF curves for the measured signals of the gates.

5.2. TG-TR-DOS Prototype

There are two main components of the TG-TR-DOS prototype. First is the TG-TR-DOS setup that consists of a light illumination subsystem, multilayered phantoms, and a photon counting and timing subsystem. Second is software to preprocess the measured curves for all gates used and reconstitute full TG-DToF for the multilayered turbid media. This software also includes a custom-made curve-fitting model to recover the optical properties (OP) for each layer of the turbid media. The curve-fitting model

was implemented using an iterative Monte Carlo program for forward modeling to simulate the light propagation and the $DTof_{Fitted}$ curves.

5.2.1. TG-TR-DOS Setup

In this setup, a picosecond pulsed diode laser source (805 nm) is used to illuminate the turbid media [68]. A custom-designed fast-gated SPAD detector, fabricated in a 130 nm silicon CMOS technology process, counts the re-emitted photons in reflectance geometry [136]. This detector has a fixed maximum width of its gate window (≈ 3.5 ns), low DCR (3 kHz), maximum count rate ≤ 100 MHz, $100 \mu\text{m}^2$ active area, and very short dead time (540 ps) [136]. Table 5.1 compares the performance features for the detectors used in this Chapter: TG-CMOS SPAD detector and SPAD detector (PDM series, MPD Italy) [164] [152].

Table 5.1: Main performance features of SPAD Detectors.

Detector Type	Front-Side Illuminated SPAD	
Fabrication Technology	Custom (planar) silicon	130 nm CMOS
Operation Mode(s)	Free-Running and Time-Gated	Time-Gated
No. of Pixels	1	1
Dimension of Pixel(s)	50 μm diameter	10 $\mu\text{m} \times 10 \mu\text{m}$
Total Active Area	1963 μm^2	100 μm^2
Time-Jitter (ps)	30	60
DCR (cps) @ Room-Temp.	2 k	3 k
Dead Time (ns)	77	4
Max. Count Rate (Mcps)	13	100
PDE at (λ)	50% @ 550nm	3% @ 510nm
P_{AP} (%)	1	3 (with 10 ns adjusted dead time)
FoM _C Counting (m)	11.4	0.53

A precision semiconductor parameter analyzer (Agilent 4156C) supplies power to the PCB of the TG-CMOS-SPAD detector [198]. The distance between the laser's fiber and the detector is fixed at 25 mm. A pulse-generator (Anritsu MP1763B) triggers the laser pulses with the gates of the detector at the same repetition rate [185] [186]. A delay unit (3D9950-0.25A - Data Delay Devices) with a minimum step = 250 ps is used to synchronize the delayed gates with the time of arrival of the re-emitted photons [199]. A $DTof$ curve of each gate is acquired by measuring the PTA which is

determined by the delay between the edge of the gate generated by the detector for each detected photon and the edge of the pulse of the laser driver. PTA is measured using a Teledyne LeCroy oscilloscope (WaveRunner 625Zi) [187]. Figure 5-1 shows the architecture of the TG-TR-DOS setup and its main components.

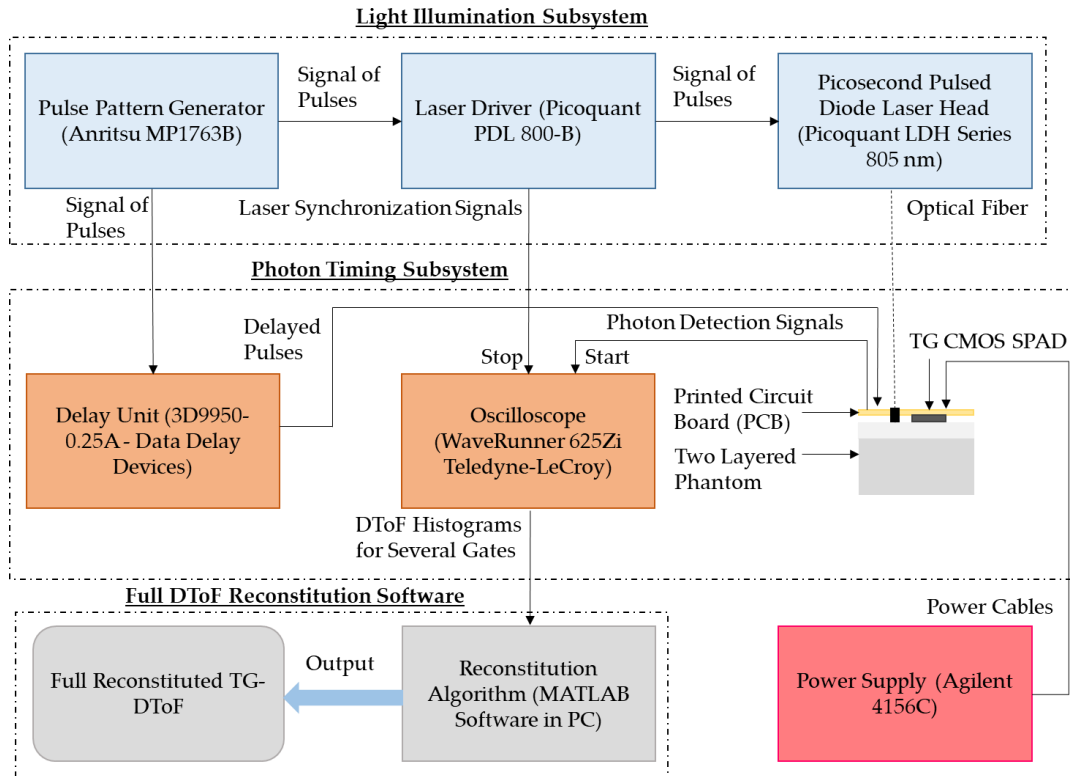


Figure 5-1: The architecture of the TG-TR-DOS prototype and the equipment used and software.

5.2.2. Phantoms

The measurements described in this Chapter are for two types of multilayered turbid objects. The first type of objects is bi-layered cylindrical solid phantoms that were prepared using epoxy-resin [74]. These phantoms were fabricated and calibrated according to the method that was explained in subsection 4.3.2. In these bi-layered phantoms, TiO_2 and India ink act as a scattering agent and an absorption agent, respectively. The values of μ_s' and μ_a were chosen to be in the range of the OP of human tissues. The thickness of the upper layer and the lower layer are 10 mm and 27 mm, respectively. The thickness of the upper layer is similar to the thickness of the superficial layer (i.e., scalp and skull) of an adult head. Also, this thickness is recommended by “nEUROpt” for bi-layered phantoms to test TR-DOS systems for

functional brain monitoring [107]. These bi-layered phantoms have fixed μ_s' for the upper and lower layers and variable μ_a for the upper and lower layers. The second type of objects is an ex vivo sheep head. This object has a thick superficial layer (≈ 20 mm for the scalp and the skull).

5.2.3. Data Acquisition and Preprocessing

A software routine is implemented to acquire the measured signal for each gate-window and reconstitute full TG-DToF for each object [197]. The aim of the reconstitution process is to extract the useful portion from the measured DToF for each gate and use these portions to perform one DToF. In this thesis, the reconstituted DToF is called full TG-DToF. Figure 5-2 illustrates an example (form literature) for extracting the useful portions from rescaled DToF (TPSF) curves for each gate to reconstitute full TG-DToF.

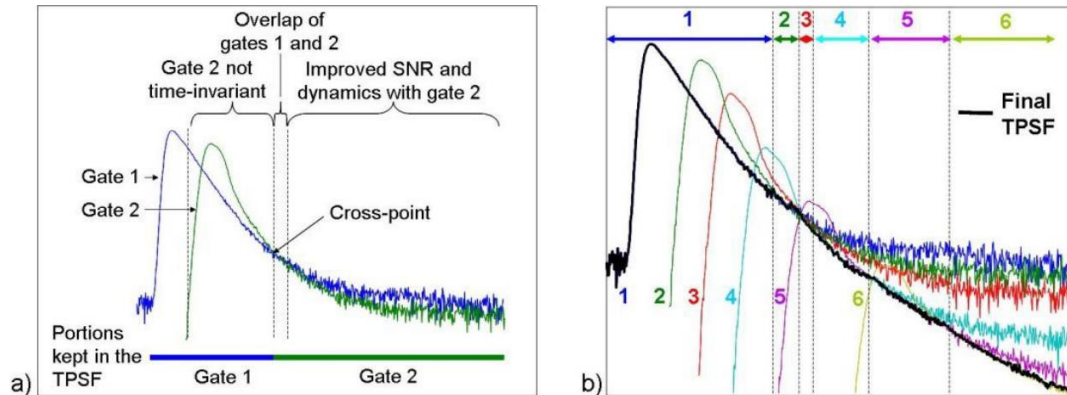


Figure 5-2: (a) Extracting the useful portion from DToF curves for each gate; and (b) example of reconstituting full TG-DToF from rescaled DToF for 6 gates; reprinted with permission from [197].

The reconstitution algorithm in this Chapter acquires the measured/simulated all signals and estimates the scaling factor of the DToF curve for each gate using the Levenberg-Marquardt method. The reconstitution algorithm in literature requires manual scaling process of the curves for the gates used according to the optical power used (for each gate) of the injected light as shown in Figure 5-3 (b). However, the reconstitution algorithm in this work fits the DToF curve for each gate with the DToF curve for the previous gate over the ranges of overlaps between the gates (without the necessity to consider the differences of the optical power used). After rescaling the DToF curves of the gates, the average value is calculated for the overlap ranges of the

DToF curves of the gates up to three overlapped gates to reconstitute the full TG-DToF. For instance, gate two starts at 0.75 ns, so the reconstitution algorithm calculates the average of gates one and two until 1.5 ns (250 ps after the beginning of gate three that starts at 1.25 ns). Then, the average of gate one, gate two and gate three is calculated until the used portion of gate four starts at 2.0 ns, and so on. This average represents the values of the reconstituted TG-DToF. Whereas, the reconstituted TG-DToF equals the first and last gates when there is no overlap between the used portions of the gates (e.g., the reconstituted TG-DToF = gate one at the range from 0.25 ns to 1.0 ns and the reconstituted TG-DToF = gate four at the range from 3.5 ns to 4 ns). Moreover, this algorithm is validated in simulation (Section 5.3) and measurements (Section 5.4) results. Figure 5-3 (a) illustrates the steps of data acquisition and preprocessing from the TG-TR-DOS setup that are used in this Chapter. Figure 5-3 (b) illustrates the steps of preprocessing (rescaling and reconstitution) of the measured DToF using several gate windows (form literature) [197].

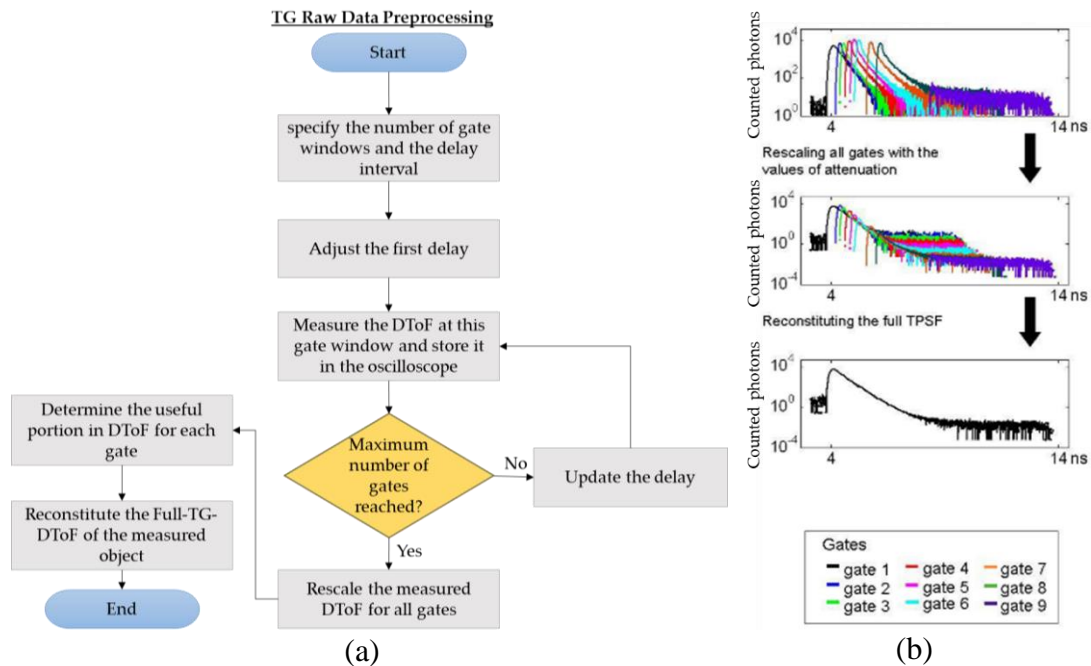


Figure 5-3: (a) Flowchart of data acquisition and preprocessing from the TG-TR-DOS setup; (b) example of rescaling and reconstitution processes; reprinted with permission from [197].

5.2.4. Preliminary Measurements

Several measurements were taken to determine the IRF_{Total} of the TG-TR-DOS setup, and to acquire the DToF curves for multilayered phantoms using the TG-TR-

DOS setup. Also, the accuracy of the delay used must be tested as well to specify the actual delays versus the nominal delays. The results of these preliminary measurements indicate some conditions and limitations that should be considered in the simulations and TG measurements of multilayered phantoms such as the deviation in the delays used and the IRF_{Total} of the TG-TR-DOS setup. Note that, these measurements are essential to determine the useful part in the DToF curve for each gate used since the full TG-DToF curves are reconstituted using a portion of the DToF for each gate [197].

Accuracy and Stability for the Delay Unit

The accuracy of the delay unit is estimated by measuring the delays between two signals (40 MHz) from the same pulse generator [185]. The first signal (start signal) is connected to the input of the delay unit. The output of the delay unit is the input of the first channel in the oscilloscope and is used as the trigger signal. The second signal (stop signal) from the pulse generator is connected to the second channel in the oscilloscope. Figure 5-4 displays the results of the deviations in the delays used.

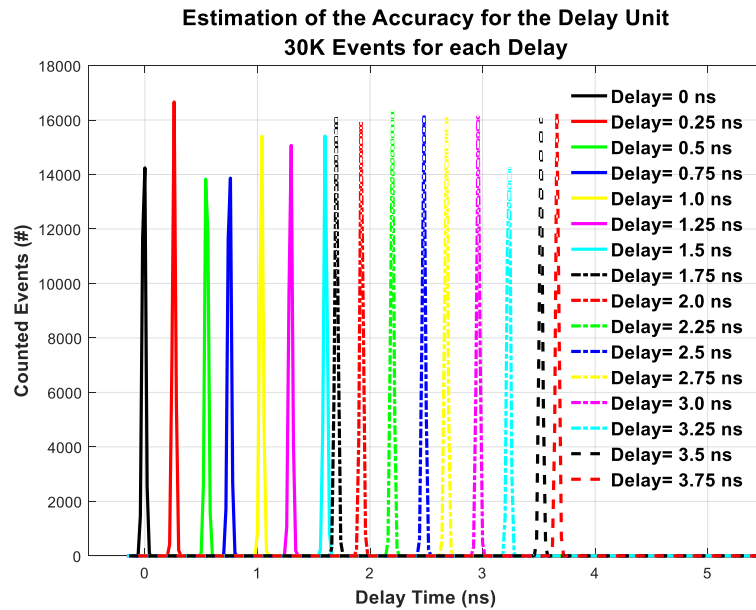


Figure 5-4: Nominal delays of the delay unit versus the measured delays using the oscilloscope.

From Figure 5-4, it is observed that there is no interference between the delayed signals. However, in the experiments, the actual delay should be considered instead of the nominal delays to maintain accurate synchronization of the gates in the TG-TR-DOS measurements. Table 5.2 summarizes the variations between the nominal and the actual measured delays for the delay unit used.

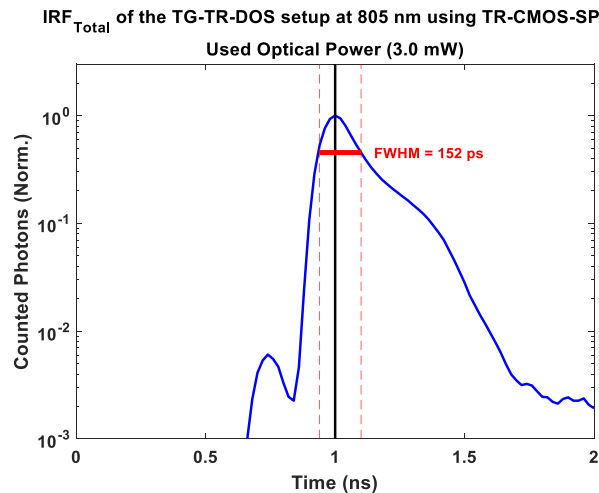
Table 5.2: Deviations between the nominal and the actual delays.

Nominal Delay (ps)	Actual Delay (ps)	Error (ps)	Nominal Delay (ps)	Actual Delay (ps)	Error (ps)
0	0	0	2000	1940	- 60
250	260	10	2250	2220	- 30
500	520	20	2500	2500	0
750	760	10	2750	2700	- 50
1000	1040	40	3000	2960	- 40
1250	1300	50	3250	3240	- 10
1500	1580	80	3500	3480	- 20
1750	1700	- 50	3750	3660	- 90

It is worth noting that the results shown in Table 5.2 are for one time bin width = 20 ps. However, events were counted four or five time bins (80-100 ps) for each delayed signal, but at least 45 % of the events were counted in one time bin in all delayed signals as shown in Figure 5-4. These results indicate for the good accuracy of the delay unit and validate the use of this delay unit because of the small deviations of measured delays relative to the nominal delays.

IRF_{Total} of the TG-TR-DOS Setup

Figure 5-5 shows the narrow IRF_{Total} (≈ 0.15 ns) for this setup for an optical power of 3.0 mW. This narrow IRF_{Total} is due to the very short timing jitter of the TG-CMOS-SPAD (< 70 ps) and the narrow pulses of the picosecond pulsed diode laser. Also, this IRF_{Total} signal was measured at the reference delay (delay = 0 ps) according to the delays mentioned in Figure 5-4 and Table 5.2. The SDD was fixed at 25 mm in transmittance geometry for the FWHM of the IRF_{Total} measurements.

Figure 5-5: IRF_{Total} of TG-TR-DOS setup using an optical power of 3 mW to illuminate the phantoms.

Features of the Gate-Windows

The effective width of gate windows and the useful portion of DToF curve for each gate are important features that should be considered in the reconstitution process. The maximum width the gate window shrinks to around 2.75 ns due to the very low probability for detecting photons in the latest 0.5 to 0.75 ns period of the ideal maximum width (3.5 ns) of the gate window for the detector used. Also, it was found that the probability of detecting photons increases significantly at the beginning of a gate window when it is synchronized with the falling tail of DToF for the re-emitted photons [197]. Therefore, a sharp peak of the counted photons appears in the first 0.25 ns for each synchronized gate window with the falling edge of the DToF. Thus, this peak is usually excluded from the reconstitution process for all gates except if the beginning of the gate window is synchronized to be over the range of the rising edge of the DToF such as in the first gate (see Figure 5-2) [197]. On the other hand, the last 0.25 ns of each gate is contaminated by noise (especially after-pulsing and memory effect) which causes a small peak at the end for each gate [157]. Therefore, the effective width of gates shrinks to be around 2.25 ns that will be used to reconstitute full TG-DToF in the simulation and the measurements in this Chapter. Figure 5-6 shows the measured DToF curves for four gates before and after rescaling and the reconstituted full-TG-DToF.

5.3. Simulation

Simulating the light propagation in two-layered phantoms is the first step to determine the required number of the gates in the measurements for these phantoms using the custom-made TG-CMOS-SPADs. The simulation considers the main features of TG-TR-DOS setup such as the IRF_{Total} and the effective width of the gate windows that were determined in subsection 5.2.4. The second step is to acquire $DToF_{Simulated}$ for each gate used and then to use the reconstitution algorithm to acquire the full-TG-DToF. Also, FR-DToF is simulated and compared with the full-TG-DToF to validate the reconstitution algorithm in the simulation. The third step is to validate this algorithm by comparing the full-TG-DToF versus FR-DToF over the same time range (4 ns) that is used for the $DToF_{Simulated}$ curves.

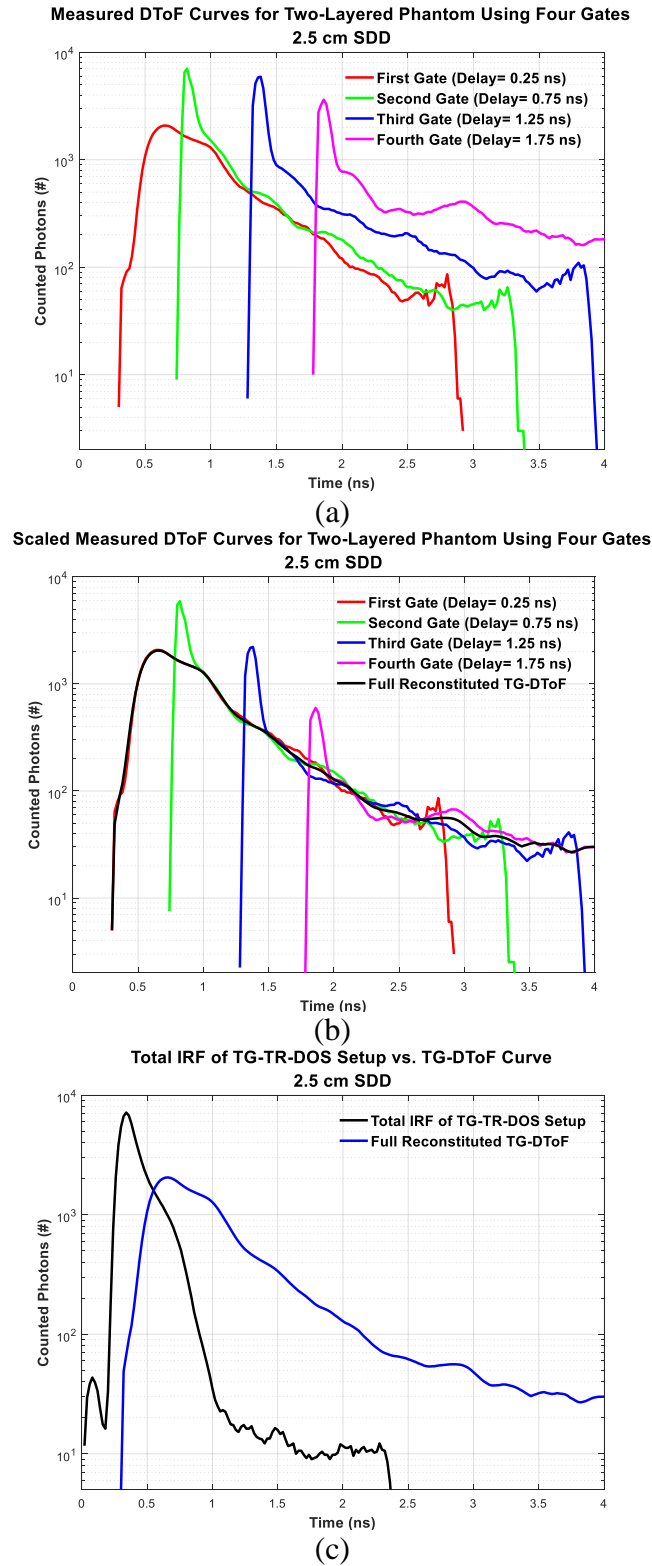


Figure 5-6: Reconstitution process for the measured DToF curves of four gates for two-layered phantoms (thickness of upper layer = 10 mm and lower layer = 27 mm); (a) the measured DToF curves; (b) the scaled measured DToF curves and the full-TG-DToF; and (c) the IRF_{Total} of the TG-TR-DOS setup versus the full-TG-DToF.

5.3.1. Light Propagation in Two-Layered Phantoms

The light propagation is simulated using four gate windows (gate width = 2.5 ns), and the delay between gates is fixed at 0.5 ns. Figure 5-7 illustrates the light propagation during four gate windows for two bi-layered phantoms with identical μ_s' for the upper and lower layers ($\mu_s' = 1.0 \text{ mm}^{-1}$). However, μ_a values are different, $\mu_a = 0.01 \text{ mm}^{-1}$ for the upper layer for both phantoms, and μ_a of the lower layers are 0.005 mm^{-1} and 0.015 mm^{-1} for the first and the second phantoms, respectively.

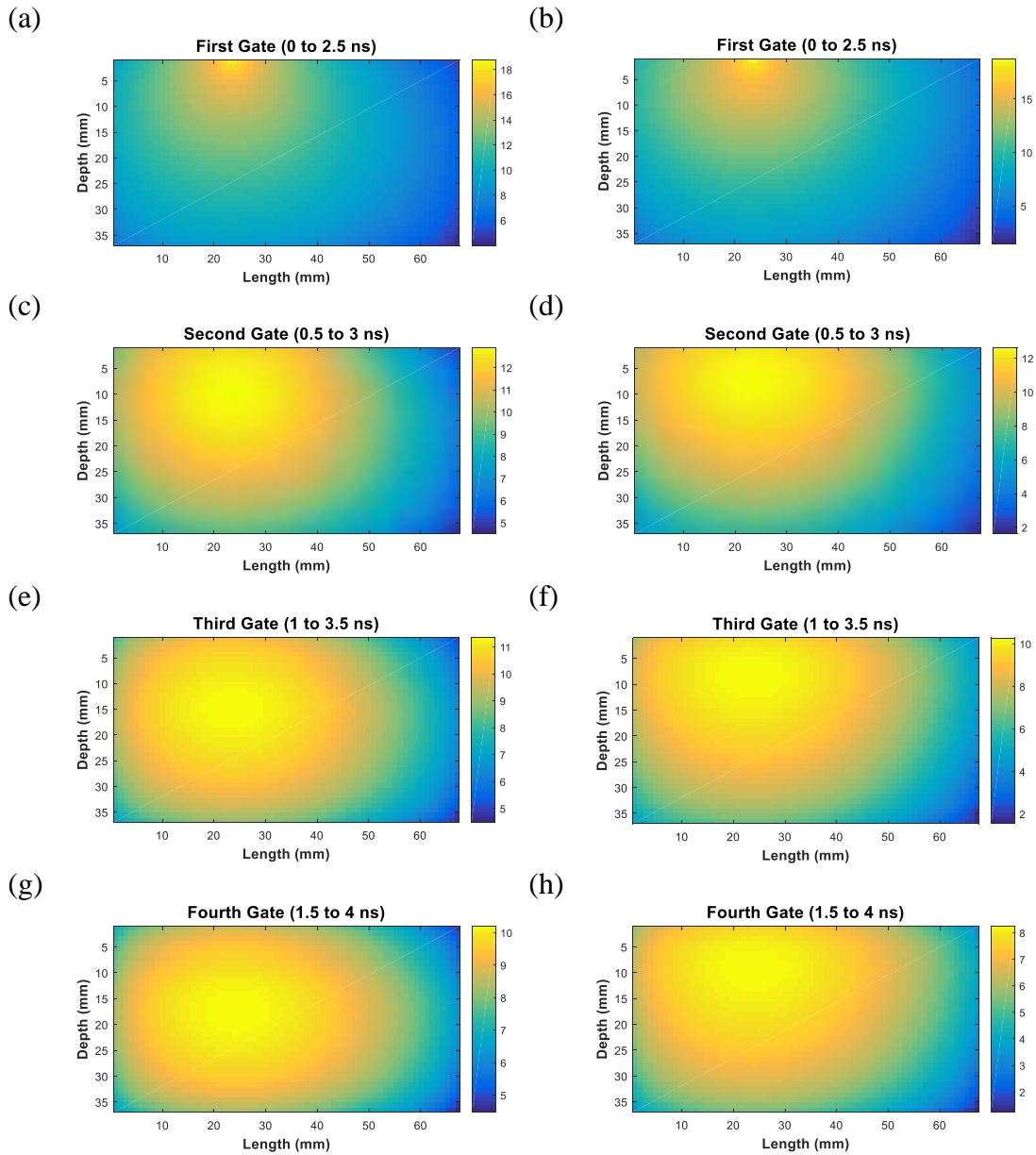


Figure 5-7: Light propagation in two bi-layered phantoms (thickness of upper layer = 10 mm and lower layer = 27 mm) during four gates. Left column: the first phantom; and right column: the second phantom.

Figure 5-7 shows the impact of lower and higher μ_a in the lower layer versus μ_a of the upper layer. Due to the low μ_a of the lower layer in the first phantom, it can be seen that more photons reach deep regions, and the light attenuation is less over the time windows of the four gates. However, in the second phantom, the density of the propagated photons in deep regions is attenuated quicker over time as a result of the high probability for photons to be absorbed in the lower layer due to the high μ_a . Therefore, the counted late photons in the DToF curves will be fewer for the second phantom relative to the first phantom.

5.3.2. FR-DToF vs. TR-DToF

In this subsection, the implemented reconstitution algorithm is tested for two bi-layered phantoms. In the simulation, it is expected to acquire similar curves of the FR-DToF and reconstituted TG-DToF because the limitations of FR detectors in counting late photons are not considered. Figure 5-8 shows the processes of the implemented algorithm toward reconstituting full TG-DToF. First, the $DToF_{Simulated}$ curves for all four gates are acquired by injecting 10^8 photons into each phantom. These DToF gates and FR-DToF are convolved with the measured IRF_{Total} of TG-TR-DOS setup. Second, the scaling factor is estimated using the Levenberg-Marquardt method. The scaling factor is used to fit the DToF for each gate. The full TG-DToF curve is reconstituted and shown in the Second step as well. Third, the full-TG-DToF curves (for both phantoms) are compared with the FR-DToF curves.

From Figure 5-8, good agreement between the outcomes of the reconstitution algorithm versus the FR-DToF curves for both phantoms. However, small differences between the full-TG-DToF curves and the FR-DToF curves when the value of the DToF tails decreased below 3% of the peak values. However, the impact of these small differences is limited on the accuracy the retrieved OP because the fitting processes usually use a large range of points of the DToF curves for fitting (see next subsection).

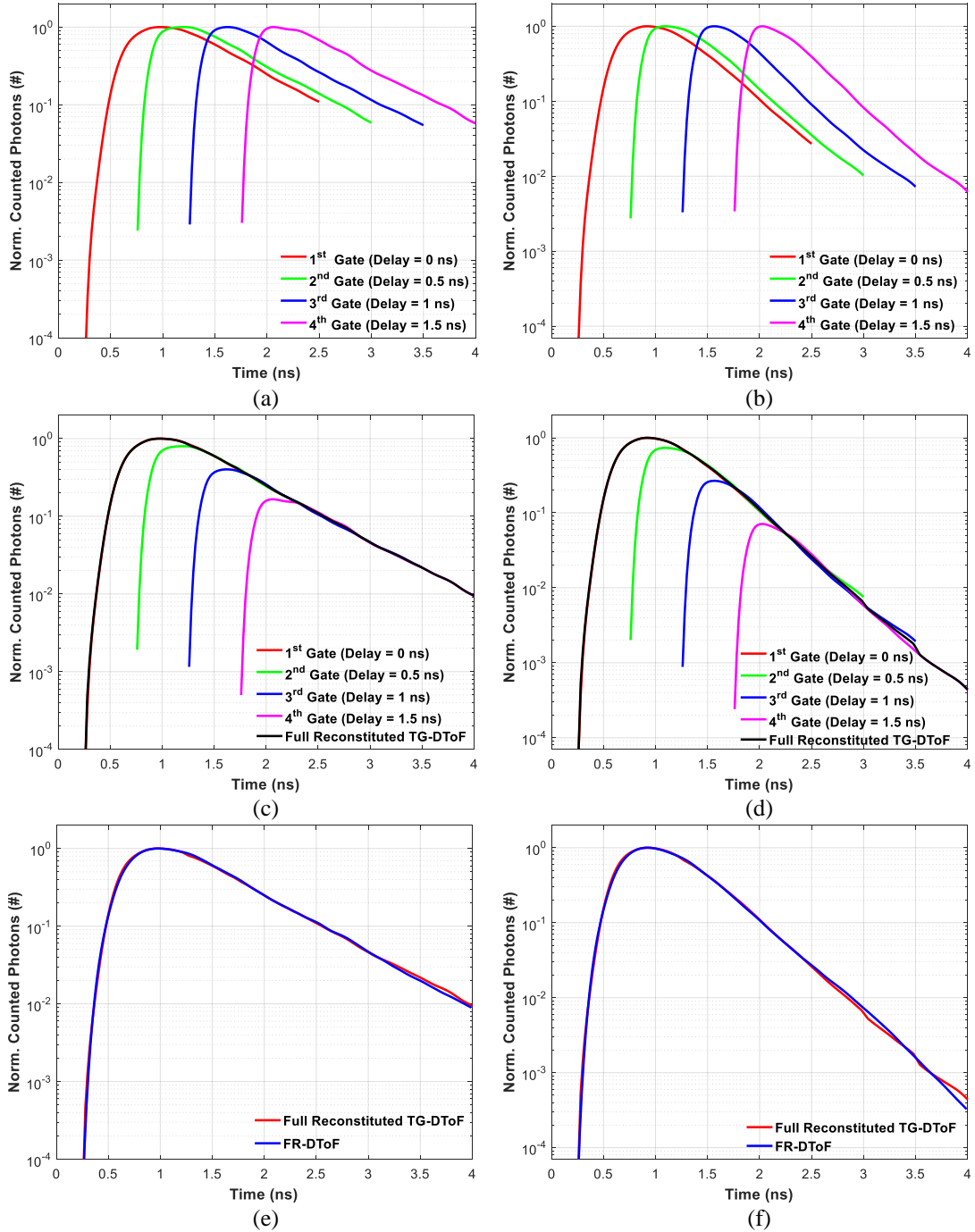


Figure 5-8: Outcomes of the reconstitution algorithm in the simulation for two bi-layered phantoms (thicknesses of upper layer = 10 mm and lower layer = 27 mm), with SDD = 2.5 cm. Left column: The first phantom. Right column: The second phantom. (a) and (b) acquiring normalized DToF curves using four gates; (c) and (d) scaling the DToF curves and reconstituting full TG-DToF curve; (e) and (f) comparing the full-TG-DToF curve versus the FR-DToF curve.

5.3.3. OP Quantification using TR-DToF Curves

Recovering the OP for multilayered turbid media is more complicated than for homogeneous turbid media. Therefore, two issues should be considered in the fitting model used. First, the analytical solution of the **time-dependent diffusion equation** (TD-DE) for homogeneous turbid media that was used in Chapter 4 is not valid for multilayered turbid media. Therefore, Monte Carlo (MC) of the **radiative transfer equation** (RTE) is used instead, and GPU-based computation (based on MCXLAB) is used to speed up the iterative fitting process [86]. Second, the OP can be recovered accurately for homogeneous turbid media using one point measurement, but for bi-layered turbid media, at least two point measurements are required. Thus, MC-based fitting was used to recover the OP for bi-layered turbid media using two detection points (SDD=2.5 cm and 3.5 cm). The fitting process ranges from 30% (of the peak values) in the rising edge until the last point in the falling edge. The used initial guesses of OP are 1.0 mm^{-1} for μ_s' and 0.01 mm^{-1} for μ_a for both layers. Figure 5-9 shows the limited impact of these small differences in the full-TG-DToF curves on the retrieved OP for the first phantom and the second phantoms. The values of OP are shown for the upper and the lower layers, respectively. It can be observed that the percentage error of μ_a is less than 4 % for the first phantom and less than 9 % for the second phantom as shown in Figure 5-9.

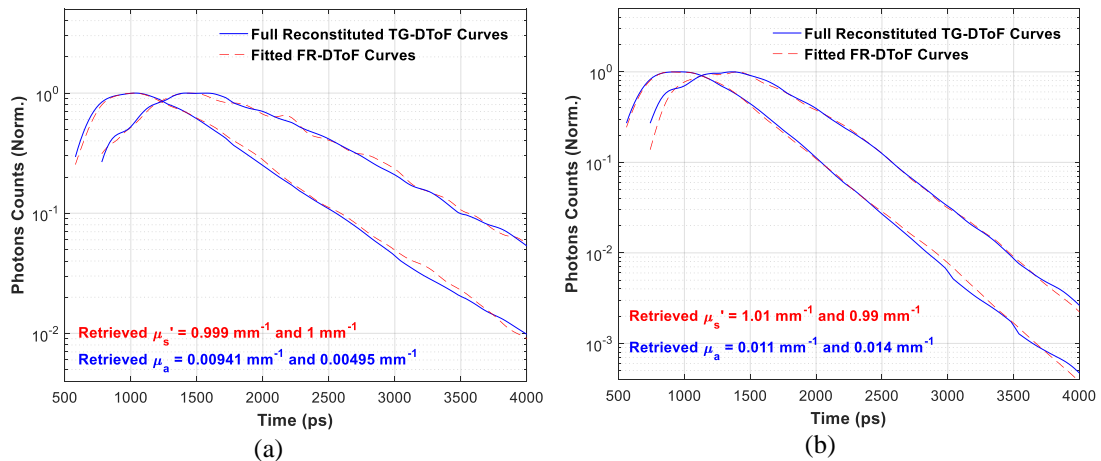


Figure 5-9: Retrieving the OP using two TG-DToF curves with SDD = 2.5 cm and 3.5 cm; for (a) the first phantom; and (b) the second phantom.

5.4. Measurements

In this Section, the implemented reconstitution algorithm is validated for the measured DToF curves for the Second type of the turbid objects (ex vivo sheep head). In contrast to the simulation, all features of both TG-TR-DOS and FR-TR-DOS setups that acquire the DToF curves appear in the measurements. Several features such as the DCR, afterpulsing, and memory effect, in addition to the IRF_{Total} which was already considered in the simulation, affect the measured results. The TG-CMOS-SPADs used had a small active area ($100 \mu\text{m}^2$) and modest PDE (3%). To overcome limitations due to size and PDE, the optical power of light used to illuminate the phantoms is increased (more injected photons). This higher optical power results in an increase in the number of photons that impinge the active area of the detector. Also, the high optical power is particularly essential to enable the detector to count a reasonable number of late photons. However, the optical power used must be kept lower than the MPE for the skin which must take into the account the source illumination area $A_{source} \sim 3 \text{ mm}^2$. On the other hand, slow update rate of the time to digital conversion process using Teledyne LeCroy oscilloscope (WaveRunner 625Zi) is a limitation for this setup. Thus, the limited maximum number of the achievable triggers by the oscilloscope due to its relatively slow update rate in the short time base 25 ns reduces the variations between the counted photons among the gates. For instance, sophisticated TCSPC devices can record more than a million photons per second due to their very short **dead time** ($T_{DEAD} < 1 \mu\text{s}$). However, the oscilloscope used can record less than a thousand events (number of detected photons) per second. Therefore, there are limited variations between the total counted photons in DToF curves that are acquired for each gate using the oscilloscope during the same data acquisition time. These limited variations make it difficult to rescale the DToF for each gate according to the optical power used of the injected light as shown in Figure 5-3 (b) and reported in the literature [157] [197]. Therefore, we used a fitting algorithm to rescale the measured and the simulated DToF for the gates used.

5.4.1. Measurements Conditions

The illumination source for the surface of the sheep's head was an 805 nm pulsed diode laser. The repetition rate of the pulses is fixed at 40 MHz. An optical power of $3.0 \text{ mW}/A_{\text{source}} (3 \text{ mm}^2)$ was used for the TG-TR-DOS measurements and $1.0 \text{ mW}/A_{\text{source}} (3 \text{ mm}^2)$ for FR-TR-DOS measurements. The optical power used for the TG-TR-DOS measurements is much lower than the MPE ($9.72 \text{ mW}/A_{\text{source}} (3 \text{ mm}^2)$) for the skin at the wavelength of the light used (805 nm). On the other hand, the FR-SPAD detector used has a larger active area and higher PDE, which lead to a higher number of counted photons. Therefore, this reduction of the optical power of the illuminated light is necessary for FR-TR-DOS measurements to prevent the pile-up effect that may disrupt the accuracy of acquired DToF histograms using the TCSPC module. DToF curves are acquired using reflectance geometry and a SDD = 25 mm for both FR-SPAD and TG-CMOS-SPAD detectors. The data acquisition time for FR-IRF and FR-DToF curves was adjusted at 30 s using MDP SPADs and TCSPC module (PicoHarp 300) [152] [94]. On the other hand, the data acquisition time for TG-IRF and DToF curves for each one of the four gates used was adjusted at 300 s using TG-CMOS-SPADs and Teledyne LeCroy oscilloscope (WaveRunner 625Zi). Figure 5-10 shows the positions of the light source and TG-CMOS-SPADs detector in the measurements for the ex vivo sheep head.

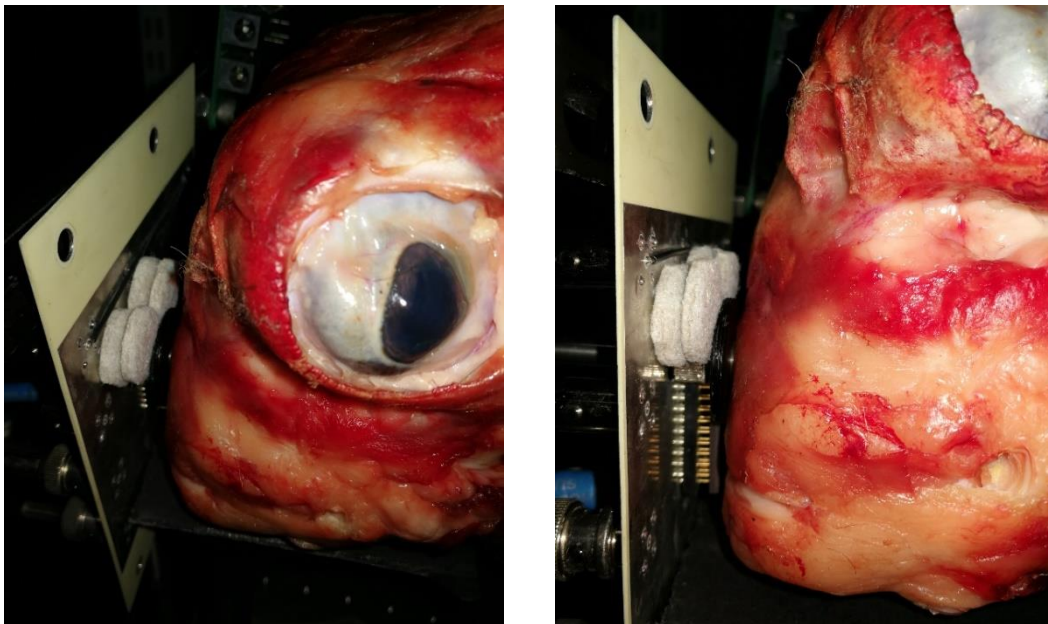


Figure 5-10: Positions of the source and detector attached to the sheep head.

5.4.2. Results and Discussion

In Figure 5-11 (a), the acquired DToF curves for the four gates are shown, and in Figure 5-11 (b), the scaled DToF curves for the four gates are shown. In Figure 5-11 (c), the shape and the DR for the FR-DToF versus the full-TG-DToF for ex vivo sheep head are compared. From Figure 5-11 (c), it is noticed that the TG-TG-DOS had acquired DToF with DR up to 2.4 orders of magnitude. This DR is still lower than the DR using the FR-TR-DOS (2.8 orders of magnitude) that is generated using sophisticated equipment such as FR-SPAD detector and a TCSPC module. This result is expected because of the SDD used is relatively large for TG-TR-DOS and SPADs fabricated in custom silicon technology usually have better performance than SPADs fabricated in standard CMOS technology, as already explained in Chapter 2.

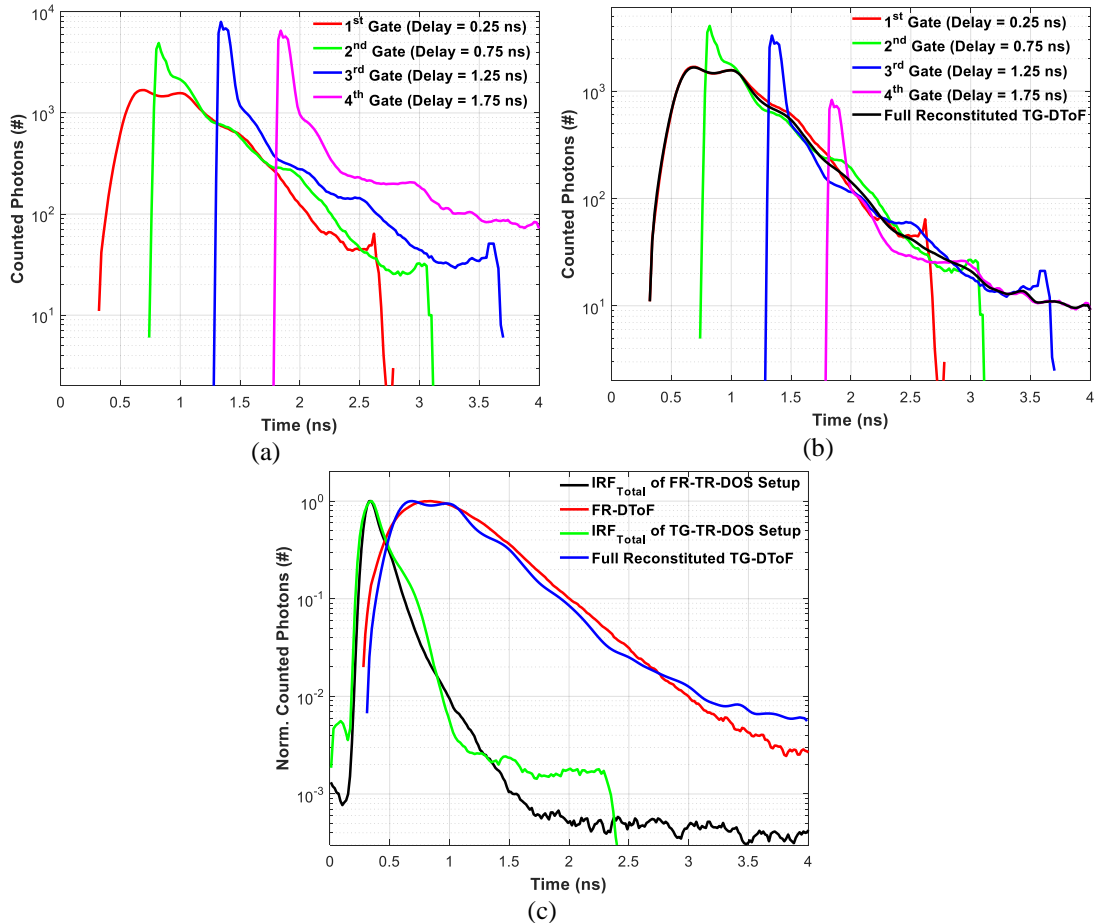


Figure 5-11: Measured raw data for Ex vivo sheep head using FR and TG detectors with SDD = 2.5 cm; (a) acquired DToF curves for four gates; (b) Scaled DToF curves for four gates and the full-TG-DToF curve; (c) Comparison of TG-DToF curve versus FR-DToF curve and the TG-IRF_{Total} versus FR-IRF_{Total}.

Note that the TG-DToF curve and FR-DToF curve have similar slopes of the tail that is correlated with the value of μ_a of the object. Also, the TG-DToF and FR-DToF curves have similar delays between peaks of the IRF_{Total} and the DToF which is correlated with the value of μ_s' of the object. These similarities can be observed in Figure 5-12 when the full-TG-DToF curve in Figure 5-11 (c) is smoothed over ten points of time bins.

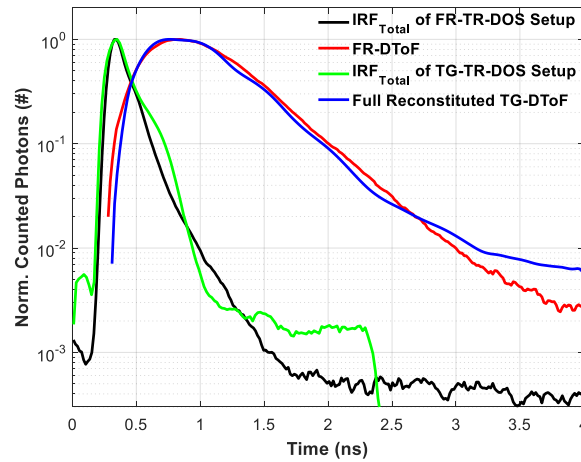


Figure 5-12: Comparison of the smoothed measured DToF curves for ex vivo sheep head using FR and TG detectors and their corresponding TG- IRF_{Total} and FR- IRF_{Total} .

5.5. Conclusions

In this Chapter, the implemented reconstitution algorithm was validated for simulated and measured DToF curves. This algorithm can be used for different number of gate windows, and simplify the preprocessing of the measured DToF curves using TG-TR-DOS systems.

On the other hand, we have successfully acquired higher DR for TG-TR-DOS raw data using fast time gating capabilities. The DR has been increased by more than an order of magnitude of the TG-TR-DOS setup in comparison with the FR-TR-DOS setup described in Chapter 4. This improvement in the DR allows for measuring re-emitted photons that reach the deeper region in turbid objects. However, the DR of the raw data using the TG-CMOS-SPAD detector is slightly lower than the achievable DR using FR-SPAD detector that are based on custom silicon technology. Thus, fabricating this TG-CMOS-SPAD detector with smaller size of the chip will allow to use smaller

SDD (5 mm – 15 mm) which can lead to an increase of the DR of this TG-TR-DOS prototype by more than one order of magnitude up to around four orders of magnitude.

In general, the TG-CMOS-SPAD detector used has good performance features for TG-TR-DOS measurements of multilayered turbid media. Nevertheless, there are several potential developments for the SPAD detectors based on low-cost and compact CMOS technology to increase the DR for TG-TR-DOS systems. First is to use an array of pixels instead of one pixel to enlarge the total active area of the SPADs detector. Second is to integrate TDCs with the array of pixels on the same chip. Each pixel should have a dedicated TDC to increase the number of counted photons because the maximum count rate for one pixel is up to 100 million counts per second. The very low level of DCR and the afterpulsing versus the achievable maximum count rate for this TG-CMOS-SPADs detector will allow for increasing the DR of each measured gate up to three orders of magnitude. This is because the percentage of noise (DCR \approx 3 kHz) will represent less than 0.1 % of the maximum measured photons that is four million per second at 80 MHz repetition rate (RR) of the pulsed laser (\leq 5 % of the RR of the laser to avoid pile-up effect). Therefore, the DR of the full TG-DToF for such TG-TR-DOS system will be up to four orders of magnitude. This high DR is higher than the achievable DR for FR-TR-DOS systems that use expensive, sophisticated FR detectors. Also, such a high DR TG-TR-DOS system will be very suitable for functional brain monitoring not only for newborns, but also for adults.

Chapter 6

CONCLUSIONS AND RECOMMENDATIONS

The following sections provide a summary and some concluding remarks, as well as recommendations for future work.

6.1. Conclusions

In this thesis, we started with specifying the main limitations of TR diffuse optics systems. These limitations are mainly the large size, the high cost of equipment required, and the computation cost of the image reconstruction process. In this work, several techniques have been used and investigated to overcome these limitations and to simplify TR diffuse optics systems.

This research work contributes to simplifying TR diffuse optics systems by investigating several issues towards improving the computation efficiency of the image reconstruction process, reducing cost and size for equipment. First, a computationally efficient TR-DOT prototype for 3D image reconstruction was developed and evaluated (Chapter 3). Second, a FR-TR-DOS system was built using a low-cost and compact custom-designed FR CMOS SPAD detector, and used to quantify the optical properties for several homogeneous turbid media (Chapter 4). This system has been evaluated using parameters from two protocols (BIP and MEDPHOT), and demonstrated comparable performance with the reported FR-TR-DOS that use commercial detectors. Third, TG-TR-DOS system was integrated using a low-cost and compact custom-designed TG CMOS SPAD detector to acquire high dynamic range (DR) for the DToF histograms for multilayered turbid media. This system demonstrated good capabilities for multilayered turbid media measurements such as functional brain monitoring

applications. Fourth, a reconstitution algorithm was implemented to acquire the full TG-DToF based on data fitting of the curves of the gate windows. This algorithm simplifies the preprocessing of the raw data measured by TG-TR-DOS systems.

In Chapter 2, the fundamentals and theory of DOS technology were introduced. Then, the main components of TR-DOS and TR-DOI systems were specified and described. Also, the role of recent technologies for solid state detectors such as SPADs and SiPMs toward reducing the cost and size for photons counting and timing subsystem was clarified. The modes of operations for TR-DOS and TR-DOI systems (FR and TG) were described as well. Lastly, the potential developments for each component in TR-DOS and TR-DOI systems and their performance have been discussed. Therefore, in this thesis, some potential issues have been investigated to improve the computation efficiency for TR-DOT, and to reduce the cost and the size for photodetectors using FR and TG CMOS SPADs.

In Chapter 3, a TR-DOT prototype was built and integrated with accelerated inverse problem solver to reconstruct 3 D images for turbid media. This TR-DOT prototype was evaluated for different conditions such as the number of sources and detectors used in the experiments, the size of the ROI, and the impact of the absence of prior structural information. All these experiments have been evaluated based on the computation time of the image reconstruction process, and the quality of the reconstructed images that represent the accuracy of the retrieved OP in each node with the measured phantoms. Overall, this prototype has demonstrated good performance that validated its usage for some applications that require high quality 3D images. Main suitable medical applications for such a prototype is to follow-up treatments for some diseases such as breast cancer tumor and hemorrhages in the newborn's brain because in these applications the anatomical information will be available from other imaging modalities. This will be helpful to reconstruct high quality 3D images within a short time (a few minutes).

In Chapter 4, a FR-TR-DOS system was built based on a custom-designed FR-CMOS SPAD detector. This prototype has demonstrated comparable performance (less than 10% percentage error for accuracy and linearity for OP quantification for homogeneous phantoms) relative to reported performance for TR-DOS systems that

utilize high-cost commercial detectors. However, this TR-DOS system has some limitations such as the modest DR (~ 1.7 orders of magnitude) and long data acquisition time (up to 20 minutes). Therefore, several potential improvements for the TR-DOS system and the FR-CMOS SPAD detectors have been concluded to eliminate these limitations. These proposed improvements will lead to realizing multichannel TR-DOS system with the low cost of the photon counting and timing equipment. Such a FR-TR-DOS system can be used in reflectance geometry for TR spectroscopic and topographic imaging for functional monitoring of newborn heads, and muscles.

In Chapter 5, a TG-TR-DOS prototype was built utilizing a custom-designed TR-CMOS SPAD detector. A reconstitution algorithm was implemented to preprocess the measured raw data to perform full TG-DToF. The TG-TR-DOS prototype has demonstrated better SNR and DR (~ 2.5 orders of magnitude) relative to the FR-TR-DOS system mentioned in Chapter 4. Also, this TG-TR-DOS prototype has demonstrated comparable DR (of the measured raw data) for the Ex-vivo object (sheep head) relative to FR-TR-DOS system based on state of the art commercial SPAD detector (implemented in custom silicon technology). Therefore, this TR-CMOS SPAD detector can be integrated with TDCs to be used for building multichannel TG-TR-DOS prototypes for functional monitoring for brain and muscles.

6.2. Recommendations for Future Work

The developments for TR-DOS and TR-DOI systems will ongoing within the next few years to reduce their cost, size, complexity and the computation time of the 3D image reconstruction. Toward this target, several issues should be investigated to develop better instruments and image reconstruction tools. The principal issues as follow:

1. Reduction of the cost and the size of equipment is important towards affordable, compact, and portable multichannel TR-DOS systems. Optical components, such as fibers to transmit the injected light or collect the re-emitted photons, should not be used in the new generation of TR-DOS systems. Therefore, these systems must be fiberless and use compact pulsed laser sources and detectors. These improvements will lead to building low-cost, compact and portable multichannel

- TR-DOS systems that used dense source-detector pairs. This new generation of multichannel TR-DOS systems will require very short data acquisition time (in range of a few seconds) to measure large objects such as heads and breasts.
2. Replacement for the traditional pulsed laser sources such as pulsed diode laser, solid-state laser, and supercontinuum fiber laser are needed to follow the trend of building low cost, compact, and portable TR-DOS and TR-DOI systems. An alternative option is VCSELs with custom timing electronics to generate short pulses for light illumination in the new generation of fiberless and portable TR-DOS and TR-DOI systems due to their compactness and low cost. VCSELs can generate pulses with a repetition rate of tens of MHz similar to other bulky and expensive pulsed laser sources. However, VCSEL sources have lower performance features than other reported pulsed laser sources regarding the width of the pulses ($\text{FWHM} \geq 300 \text{ ps}$), and the maximum average power ($P_{\text{AVG}} \leq 1 \text{ mW}$).
 3. Arrays of SPADs with TDCs (integrated into the same chip) should replace single pixel FR and TG CMOS SPAD detectors. The performance features for FR-CMOS SPAD detectors should be considered, as stated earlier in subsections 4.4.5 and 4.4.6. For TG CMOS SPAD detectors, adding timing electronics for each set of pixels to adjust different delays will be very useful to achieve the entire TG measurements using one synchronization delay. For instance, if 10×10 array of TG CMOS pixels can be designed with a fixed width of the gate (2 – 3 ns) for each pixel and associated timing electronics for each row of pixels. Figure 6-1 shows an example of a proposed design of TG-CMOS-SPAD detectors for TR-DOS applications. The width of the gate and the built-in delay for each row of pixels can perform TG-measurements for a range longer than 5.5 ns. This range is enough to acquire DToF curves in which the typical range is from 2 ns up to 5 ns. On the other hand, the size of the chip of the SPAD detector should be reduced from its current size ($28\text{mm} \times 28\text{mm}$). Minimizing the size of chips will allow of using short SDD measurements and dense source-detector pairs.

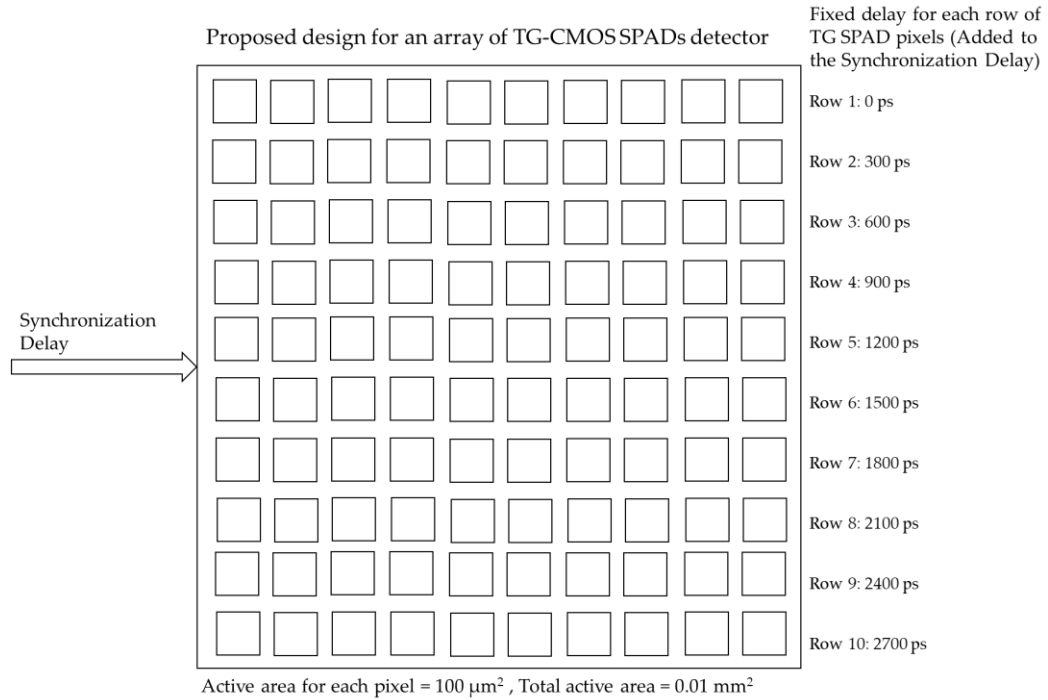


Figure 6-1: Proposed TG CMOS-SPAD detector to harvest the re-emitted photons using up to ten gates with a fixed synchronization delay.

4. The Image reconstruction algorithm can be improved by using forward problem solver based on GPUs to shorten the computation time, particularly for the iterative forward modeling. GPU based computation can simulate the propagation of 100 million photons within a few seconds. Thus, the load of the CPUs of the PC is reduced drastically, and the CPU is dedicated to computing the serial processes only (such as solving the Jacobian matrix). Incorporating GPU based computation with the image reconstruction algorithm used in Chapter 3 can reduce the computation time, particularly when no prior knowledge is used.
5. Achieving the abovementioned improvements of new generation of TR-DOI systems will make them affordable, portable, and easy to use. Therefore, new generation of TR-DOI systems can be used in several applications, especially in medicine. For example, they can be used in paramedic services to quickly diagnose some head injuries such as brain hemorrhage. Early diagnosis and treatment are helpful to reduce the consequences of brain hemorrhage.

Appendix I: MATLAB CODES

FWHM of IRF_{Total} (Results were shown in Figure 4-7)

```

clc;
clear;
close all;
txt1 = {'FontSize',14,'FontWeight','bold'};
txt2 = {'FontSize',16,'FontWeight','bold'};
txt3 = {'FontSize',12,'FontWeight','bold'};
txt4 = {'FontSize',10,'FontWeight','bold'};
sty = {'LineWidth',2,'MarkerSize',4};
pos = {[0.1 0.135 0.385 0.825],[0.56 0.135 0.395 0.825]};
cmap=colormap(lines);
d=load('CMOSIRFLOW.dat'); t = d(:,1)/1000; y11 = d(:,2); % Load the IRF curve with the corresponding time bins
%y11 = smooth(y11,1); % Smooth the IRF curve (optional)
[max11, index11]=max(y11); % Find the peak of the IRF curve
y1 = y11(index11-74:index11+75); % Adjust the position of the peak to be in the middle of the figure
[max1, index1]=max(y1);
t = t(1:150); t=t-0.02*index1; % Adjust the corresponding time bins
tHstep=(t(2)-t(1))/2;
WHM=0.5*max(y1); % Determine the value of the half maximum
for Start=index1:-1:1 % Determine the time bin if the half maximum on the rising edge
    if y1(Start) <=WHM
        break;
    end
end
for Last=index1:1:size(y1) % Determine the time bin if the half maximum on the falling edge
    if y1(Last) <=WHM
        break;
    end
end
if y1(Start)<=WHM*0.8
    tHstep=tHstep*-1;
elseif y1(Start)<=WHM*0.9
    tHstep=tHstep*-0.5;
elseif y1(Start)<=WHM*1.1
    tHstep=tHstep*0;
elseif y1(Start)<=WHM*1.2
    tHstep=tHstep*0.5;
end
FWHM0=(Last-Start)*(t(2)-t(1))+tHstep;
figure(1) % Draw a figure of the IRF curve with FWHM details
set(gcf,'WindowStyle','docked');
plot(t,y1,'-b',sty{:}); hold on;
set(gca,'YScale','log',txt2{:});
title({'IRF_T_o_t_a_1 of the TR-DOS setup at 685 nm using FR CMOS SPAD','Low Optical Power (0.05 mW)'},txt1{:});
ylabel('Counted Photons',txt1{:});
xlabel('Time (ns)',txt1{:});
xlim([t(1),t(150)]);
ylim([100,max(y1)*2]);
grid on;
yL = get(gca,'YLim');
line([t(index1) t(index1)],yL,'Color','k','LineWidth',2);
line([t(Last-1)-FWHM0 t(Last-1)-FWHM0],yL,'Color','r','LineStyle','--');
line([t(Last) t(Last)],yL,'Color','r','LineStyle','--');
line([t(Last-1)-FWHM0 t(Last)],y1(Last) y1(Last)],'Color','r','LineStyle','-','LineWidth',4);
text((t(11)),y1(Last),['FWHM = ',num2str(FWHM0*1000,3),' ps'],txt1{:},'Color','r');

```

Quantification of the Optical Properties of Homogeneous Medium (Main Script).

Results were shown in Figure 4-5 and Table 4.1.

```

clc;
clear;
clear cfg;
close all;
txt1 = {'FontSize',14,'FontWeight','bold'};
txt2 = {'FontSize',16,'FontWeight','bold'};
sty = {'LineWidth',1.5,'MarkerSize',3};
if(exist('tddiffusion','file')~=2 | exist('cwndiffusion','file')~=2)
    error(sprintf('Scripts "tddiffusion.m" and "cwndiffusion.m" were not found'));
end
d1=load('Phantoms685withoutDNL1.dat');
d2=load('CMOSIRF10.dat');
ydata0=d1(:,5);
x1=d2(:,2);
ydata0=smooth(ydata0,7);
ydata0=ydata0/max(ydata0);
[max1, index1]= max(ydata0);
for Start=index1:-1:1
    if ydata0(Start) <=0.612
        break;
    end
end
for Last=index1:1:size(ydata0)
    if ydata0(Last) <=0.16
        break;
    end
end
ydata=ydata0(Start:Last,:);
xdata=10:20:20*size(ydata);
xdata=transpose(xdata);
x1=x1/max(x1);
x0=[0.010,10,1.5];
x=x0;
options = optimoptions(@lsqcurvefit,'Algorithm','trust-region-
reflective','CheckGradients',true,'FiniteDifferenceType','central','FiniteDifferenceStepSize',0.001,'MaxFunction
Evaluations',200,'FunctionTolerance',0.000001,'StepTolerance',0.000001,'Display','iter');
%options = optimoptions(@lsqcurvefit,'Algorithm','levenberg-
marquardt','CheckGradients',true,'FiniteDifferenceType','forward','FiniteDifferenceStepSize',0.001,'MaxFunction
Evaluations',200,'FunctionTolerance',0.00000001,'StepTolerance',0.00000001,'Display','iter');
lb = [0.001,1,1.45];
ub = [0.04,40,1.55];
%lb = [];
%ub = [];
fun = @(x,xdata)ForMod(x1,x,Start,Last);
[x,resnorm,residual,exitflag,output] = lsqcurvefit(fun,x0,xdata,ydata,lb,ub,options);
twin=10+Start*20:20:20*Last+10;
twin=transpose(twin);
figure(1);
plot(twin,ydata,'b-',twin,fun(x,xdata),'r--',sty{:});hold on;
ylim([0,1.2]);
legend({'Measured DToF Curve','Fitted DToF Curve'},txt1{:});
legend boxoff;
set(gca,'yscale');
xlabel('Time (ps)',txt2{:});
ylabel('Norm. Photons Counts (#)',txt2{:});
title({'Measured and Fitted DToF Curves for Sample B2 at 830 nm','2.7 cm SDD'},txt2{:}) %
text(twin(2),0.3,['Retrieved \mu_s=' ,num2str(x(1,2)/10,3),' mm-1'],txt1{:},'Color','r');
text(twin(2),0.2,['Retrieved \mu_a=' ,num2str(x(1,1),3),' mm-1'],txt1{:},'Color','b');

```

```
box on;
grid on;
```

Quantification of the Optical Properties of Homogeneous Medium (Iterative Function)

```
function [fdata] = ForMod(x1,x,Start,Last)
dim=67;
cfg.vol=ones(dim,dim,27);
cfg.vol=uint8(cfg.vol);
for xi=1:dim
    for yi=1:dim
        dist=(xi-34).^2+(yi-34).^2;
        if dist>1156
            cfg.vol(xi,yi,1:27)=0;
        end
    end
end
cfg.srcpos=[22 34 0]; % choose a position of the source
cfg.srkdir=[0 0 1]; % choose a direction of the light
cfg.gpuid=1;
cfg.autopilot=1;
cfg.prop=[0 0 1 1 % medium 0: the environment
          x(1,1) x(1,2) 0.9 x(1,3)]; % medium 1: the homogeneous turbid medium
% running simulation with boundary reflection
cfg.tstart=0;
cfg.tend=5e-9;
cfg.tstep=20e-12;
twin=cfg.tstart+cfg.tstep/2:cfg.tstep:cfg.tend;
twin=transpose(twin);
cfg.isreflect=1; % enable reflection at exterior boundary
cfg.isrefint=1; % enable reflection at interior boundary too
detpos=[49 34 0]; % choose a position of the detector
Reff=-1.44*(cfg.prop(2,4))^2+0.71*(cfg.prop(2,4))^-1+0.668+0.00636*cfg.prop(2,4);
td1=tddiffusion(cfg.prop(2,1), cfg.prop(2,2)*(1-cfg.prop(2,3)), c0/cfg.prop(2,4), Reff, cfg.srcpos, detpos,
twin)/max(tddiffusion(cfg.prop(2,1), cfg.prop(2,2)*(1-cfg.prop(2,3)), c0/1.37, 0.493, cfg.srcpos, detpos, twin));
y1=double(td1);
y1=transpose(y1);
y1=y1/max(y1);
x1=x1(1:50,:);
output=conv(x1,y1);
output=output/max(output);
output=double(output);
output=transpose(output);
fdata=output(Start:Last,:);
end
```

Light Propagation within 4 Gate windows for bi-layered Medium (Results were shown in Figure 5-7).

```
clc
clear;
clear cfg;
close all;
txt1 = {'FontSize',14,'FontWeight','bold'};
txt2 = {'FontSize',12,'FontWeight','bold'};
c0=299792458000;
```

```

smth=3;
cfg.nphoton=1e8;
dim=67;
[xi,yi,zi]=meshgrid(1:dim,1:37,1:dim);
cfg.vol=zeros(size(xi));
cfg.vol=uint8(cfg.vol);
dist=(xi-34).^2+(zi-34).^2;
cfg.vol(dist<1156 & yi<11)=1;
cfg.vol(dist<1156 & yi>10)=2;
cfg.vol(yi>37)=0;
cfg.srcpos='pencil';
cfg.srcpos=[0 24 34];
cfg.srkdir=[1 0 0];
cfg.gpuid=1;
cfg.autopilot=1;
cfg.maxdetphoton=1e7;
x = [0.005,10;0.01,10;0.015,10];
cfg.prop=[0 0 1 1 % medium 0: the environment
          x(2,1) x(2,2) 0.9 1.5
          x(1,1) x(1,2) 0.9 1.5];
% calculate the flux distribution with the given config
% running simulation with boundary reflection
cfg.isreflect=1; % enable reflection at exterior boundary
cfg.tstart=0e-9;
cfg.tend=2.5e-9;
cfg.tstep=2.5e-9;
[f1,det1]=mcxlab(cfg);
fla=f1;
%-----%
cfg.tstart=0.5e-9;
cfg.tend=3e-9;
cfg.tstep=2.5e-9;
[f1,det1]=mcxlab(cfg);
flb=f1;
%-----%
cfg.tstart=1e-9;
cfg.tend=3.5e-9;
cfg.tstep=2.5e-9;
[f1,det1]=mcxlab(cfg);
flc=f1;
%-----%
cfg.tstart=1.5e-9;
cfg.tend=4e-9;
cfg.tstep=2.5e-9;
[f1,det1]=mcxlab(cfg);
fld=f1;
%-----%
figure(1);
imagesc(squeeze(log(fla(1).data(:,:,34,:))));
colorbar;axis equal;%axis off;
ylim([0,67]);ylim([1,37]);
xlabel('Length (mm)',txt2{:}); ylabel('Depth (mm)',txt2{:});
cl=get(gca,'clim');
title({'Light Propagation in Two-Layered Phantom','First Gate (0 to 2.5 ns)'},txt1{:})
figure(2);
imagesc(squeeze(log(flb(1).data(:,:,34,:))));
colorbar;axis equal;
ylim([0,67]);ylim([1,37]);
xlabel('Length (mm)',txt2{:}); ylabel('Depth (mm)',txt2{:});
cl=get(gca,'clim');
title({'Light Propagation in Two-Layered Phantom','Second Gate (0.5 to 3 ns)'},txt1{:})
figure(3);

```

```

imagesc(squeeze(log(f1c(1).data(:,:,34,:))));
colorbar;axis equal;
ylim([0,67]);ylim([1,37]);
xlabel('Length (mm)',txt2{:}); ylabel('Depth (mm)',txt2{:});
cl=get(gca,'clim');
title('Light Propagation in Two-Layered Phantom','Third Gate (1 to 3.5 ns)',txt1{:});
figure(4);
imagesc(squeeze(log(f1d(1).data(:,:,34,:))));
colorbar;axis equal;
ylim([0,67]);ylim([1,37]);
xlabel('Length (mm)',txt2{:}); ylabel('Depth (mm)',txt2{:});
cl=get(gca,'clim');
title('Light Propagation in Two-Layered Phantom','Fourth Gate (1.5 to 4 ns)',txt1{:});

```

Reconstitution Algorithm for Simulated DToF for four Gate windows for bi-layered Medium (Results were shown in Figure 5-8).

```

clc
clear;
clear cfg;
close all;
txt1 = {'FontSize',14,'FontWeight','bold'};
txt2 = {'FontSize',12,'FontWeight','bold'};
c0=299792458000;
smth=3;
d=load('TG-IRF1.dat');
tIRF = d(:,1); IRF = d(:,2);
IRF = smooth(IRF,5);
IRF= IRF/max(IRF);
cfg.nphoton=1e7;
dim=67;
[xi,yi,zi]=meshgrid(1:dim,1:37,1:dim);
cfg.vol=zeros(size(xi));
cfg.vol=uint8(cfg.vol);
dist=(xi-34).^2+(zi-34).^2;
cfg.vol(dist<1156 & yi<11)=1;
cfg.vol(dist<1156 & yi>10)=2;
cfg.vol(yi>37)=0;
cfg.srctype='pencil';
cfg.srcpos=[0 22 34];
cfg.srkdir=[1 0 0];
cfg.gpuid=1;
cfg.autopilot=1;
cfg.maxdetphoton=1e7;
x = [0.005,10;0.01,10;0.015,10;0.02,10];
cfg.prop=[0 0 1 1 % medium 0: the environment
          x(2,1) x(2,2) 0.9 1.5 % medium 1: the upper layer
          x(3,1) x(3,2) 0.9 1.5]; % medium 2: the lower layer
% calculate the flux distribution with the given config
% running simulation with boundary reflection
cfg.isreflect=1; % enable reflection at exterior boundary
cfg.tstart=0e-9;
cfg.tend=2.5e-9;
cfg.tstep=2.5e-9;
[f1,det1]=mcxlab(cfg);
f1a=f1;
%-----%
cfg.tstart=0.5e-9;
cfg.tend=3e-9;
cfg.tstep=2.5e-9;

```



```

[f1,det1]=mcxlab(cfg);
f1b=f1;
%-----%
cfg.tstart=1e-9;
cfg.tend=3.5e-9;
cfg.tstep=2.5e-9;
[f1,det1]=mcxlab(cfg);
f1c=f1;
%-----%
cfg.tstart=1.5e-9;
cfg.tend=4e-9;
cfg.tstep=2.5e-9;
[f1,det1]=mcxlab(cfg);
f1d=f1;
%-----%
figure(1);
imagesc(squeeze(log(f1a(1).data(:,:,34,:))));
colorbar;axis equal;%axis off;
ylim([0,67]);ylim([1,37]);
xlabel('Length (mm)',txt2{:}); ylabel('Depth (mm)',txt2{:});
cl=get(gca,'clim');
title({'Light Propagation in Two-Layered Phantom','First Gate (0 to 2.5 ns)'},txt1{:})
figure(2);
imagesc(squeeze(log(f1b(1).data(:,:,34,:))));
colorbar;axis equal;
ylim([0,67]);ylim([1,37]);
xlabel('Length (mm)',txt2{:}); ylabel('Depth (mm)',txt2{:});
cl=get(gca,'clim');
title({'Light Propagation in Two-Layered Phantom','Second Gate (0.5 to 3 ns)'},txt1{:})
figure(3);
imagesc(squeeze(log(f1c(1).data(:,:,34,:))));
colorbar;axis equal;
ylim([0,67]);ylim([1,37]);
xlabel('Length (mm)',txt2{:}); ylabel('Depth (mm)',txt2{:});
cl=get(gca,'clim');
title({'Light Propagation in Two-Layered Phantom','Third Gate (1 to 3.5 ns)'},txt1{:})
figure(4);
imagesc(squeeze(log(f1d(1).data(:,:,34,:))));
colorbar;axis equal;
ylim([0,67]);ylim([1,37]);
xlabel('Length (mm)',txt2{:}); ylabel('Depth (mm)',txt2{:});
cl=get(gca,'clim');
title({'Light Propagation in Two-Layered Phantom','Fourth Gate (1.5 to 4 ns)'},txt1{:})
%-----%
% 1st Gate delay=0
cfg.tstart=0.25e-9;
cfg.tend=2.5e-9;
cfg.tstep=20e-12;
twin1=cfg.tstart+cfg.tstep/2:cfg.tstep:cfg.tend;
detpos=[1 47 34]; % choose a point inside the domain
fprintf('running simulation ... this takes about 11 seconds on a GTX 470\n');
tic;
f2=mcxlab(cfg);
toc;
f2=f2.data;
f21=f2(detpos(1),detpos(2),detpos(3),:)/max(f2(detpos(1),detpos(2),detpos(3),:));
PhotonsMax=max(f2(detpos(1),detpos(2),detpos(3),:));
f21s=smooth(f21,smth);
f21s=f21s/max(f21s);
f21s=conv(IRF,f21s);
f21s=f21s(1:113);
f21s=f21s/max(f21s);

```

```

f21s=double(f21s);
f21sa=f21s*(1/max(f21s));
twin1=transpose(twin1);
%-----%
%2nd Gate delay=1ns
cfg.tstart=0.75e-9;
cfg.tend=3.01e-9;
cfg.tstep=20e-12;
twin2=cfg.tstart+cfg.tstep/2:cfg.tstep:cfg.tend;
tic;
f2=mcxlab(cfg);
toc;
f2=f2.data;
f22=f2(detpos(1),detpos(2),detpos(3,:))/max(f2(detpos(1),detpos(2),detpos(3,:)));
f22s=smooth(f22,smth);
f22s=conv(IRF,f22s);
f22s=f22s(1:113);
f22s=f22s/max(f22s);
f22s=double(f22s);
f22sa=f22s*(1/max(f22s));
twin2=transpose(twin2);
%-----%
%3rd Gate delay=1ns
cfg.tstart=1.25e-9;
cfg.tend=3.51e-9;
cfg.tstep=20e-12;
twin3=cfg.tstart+cfg.tstep/2:cfg.tstep:cfg.tend;
tic;
f2=mcxlab(cfg);
toc;
f2=f2.data;
f23=f2(detpos(1),detpos(2),detpos(3,:))/max(f2(detpos(1),detpos(2),detpos(3,:)));
f23s=smooth(f23,smth);
f23s=conv(IRF,f23s);
f23s=f23s(1:113);
f23s=f23s/max(f23s);
f23s=double(f23s);
f23sa=f23s*(1/max(f23s));
twin3=transpose(twin3);
%-----%
%4rd Gate delay=1.5ns
cfg.tstart=1.75e-9;
cfg.tend=4.01e-9;
cfg.tstep=20e-12;
twin4=cfg.tstart+cfg.tstep/2:cfg.tstep:cfg.tend;
tic;
f2=mcxlab(cfg);
toc;
f2=f2.data;
f24=f2(detpos(1),detpos(2),detpos(3,:))/max(f2(detpos(1),detpos(2),detpos(3,:)));
f24s=smooth(f24,smth);
f24s=conv(IRF,f24s);
f24s=f24s(1:113);
f24s=f24s/max(f24s);
f24s=double(f24s);
f24sa=f24s*(1/max(f24s));
twin4=transpose(twin4);
%-----%
shift1=6; shift2=55;
[max1, index1]= max(f21s);[max2, index2]= max(f22s);[max3, index3]= max(f23s);[max4, index4]=
max(f24s);
xdata1=twin2(index2+shift1:index2+shift2);

```

```

ydata1=f21s(index2+25+shift1:index2+25+shift2);
x0=[1];
options = optimoptions(@lsqcurvefit,'Algorithm','levenberg-
marquardt','CheckGradients',true,'FiniteDifferenceType','central','FiniteDifferenceStepSize',0.000001,'MaxFunc-
tionEvaluations',200,'FunctionTolerance',0.00000001,'StepTolerance',0.0000001,'Display','iter');
lb = [];
ub = [];
fun = @(x1,xdata1)f22s(index2+shift1:index2+shift2)*x1;
[x1,resnorm1,residual1,exitflag1,output1] = lsqcurvefit(fun,x0,xdata1,ydata1,lb,ub,options);
f22s= f22s*x1;
xdata2=twin3(index3+25+shift1:index3+25+shift2);
ydata2=f22s(index3+25+shift1:index3+25+shift2);
fun = @(x2,xdata2)f23s(index3+shift1:index3+shift2)*x2;
[x2,resnorm2,residual2,exitflag2,output2] = lsqcurvefit(fun,x0,xdata2,ydata2,lb,ub,options);
f23s= f23s*x2;
xdata3=twin4(index4+shift1:index4+shift2);
ydata3=f23s(index4+25+shift1:index4+25+shift2);
fun = @(x3,xdata3)f24s(index4+shift1:index4+shift2)*x3;
[x3,resnorm3,residual3,exitflag3,output3] = lsqcurvefit(fun,x0,xdata3,ydata3,lb,ub,options);
f24s= f24s*x3;
%-----
DToF(1:50)=f21s(1:50); DToF(51:75)=(f21s(51:75)+f22s(26:50))/2;
DToF(76:100)=(f21s(76:100)+f22s(51:75)+f23s(26:50))/3;
DToF(101:125)=(f22s(76:100)+f23s(51:75)+f24s(26:50))/3;DToF(126:150)=(f23s(76:100)+f24s(51:75))/2;DT
oF(151:188)=f24s(76:size(f24s));
DToF=smooth(DToF,smth);
cfg.tstart=0.25e-9;
cfg.tend=4.01e-9;
cfg.tstep=20e-12;
twin5=cfg.tstart+cfg.tstep/2:cfg.tstep:cfg.tend;
twin5=transpose(twin5);
%-----%
%FR_DToF
cfg.tstart=0e-9;
cfg.tend=4e-9;
cfg.tstep=20e-12;
twin=cfg.tstart+cfg.tstep/2:cfg.tstep:cfg.tend;
tic;
f2=mcxlab(cfg);
toc;
f2=f2.data;
FR_DToF=f2(detpos(1),detpos(2),detpos(3,:)/max(f2(detpos(1),detpos(2),detpos(3,:)));
PhotonsMax1=max(f2(detpos(1),detpos(2),detpos(3,:)));
FR_DToF=smooth(FR_DToF,smth);
FR_DToF=conv(IRF,FR_DToF);
FR_DToF=FR_DToF(1:200);
FR_DToF=FR_DToF/max(FR_DToF);
FR_DToF=double(FR_DToF);
twin=transpose(twin);
twin1=twin1*1e9;twin2=twin2*1e9;twin3=twin3*1e9;twin4=twin4*1e9;twin5=twin5*1e9;twin=twin*1e9;
figure(5);
plot(twin1,f21sa,'r-', 'LineWidth', 2); hold on;
plot(twin2,f22sa,'g-', 'LineWidth', 2); hold on;
plot(twin3,f23sa,'b-', 'LineWidth', 2); hold on;
plot(twin4,f24sa,'m-', 'LineWidth', 2); hold on;
set(gca,'ylim',[10^-4 5*10^0]);
legend({'First Gate (Delay= 0 ns)','Second Gate (Delay= 0.5 ns)','Third Gate (Delay= 1 ns)','Fourth Gate
(Delay= 1.5 ns)'};txt2{:});
legend boxoff;
set(gca,'yscale','log');
xlabel('Time (ns)',txt2{:})
ylabel('Norm. Counted Photons (#)',txt2{:})

```

```

title({'Normalized DToF Curves for Four Gates','2.5 cm SDD'},txt1{:}) %
box on;
grid on;
figure(6);
plot(twin1,f21s, 'r-', 'LineWidth', 2); hold on;
plot(twin2,f22s, 'g-', 'LineWidth', 2); hold on;
plot(twin3,f23s, 'b-', 'LineWidth', 2); hold on;
plot(twin4,f24s, 'm-', 'LineWidth', 2); hold on;
plot(twin5,DToF, 'k-', 'LineWidth', 2); hold on;
set(gca,'ylim',[10^-4 5*10^0]);
legend({'First Gate (Delay= 0 ns)', 'Second Gate (Delay= 0.5 ns)', 'Third Gate (Delay= 1 ns)', 'Fourth Gate
(Delay= 1.5 ns)', 'Full Reconstituted TG-DToF'},txt2{:});
legend boxoff;
set(gca,'yscale','log');
xlabel('Time (ns)',txt2{:})
ylabel('Norm. Counted Photons (#)',txt2{:})
title({'DToF Curves for Four Gates and TG-DToF Curve','2.5 cm SDD'},txt1{:}) %
box on;
grid on;
figure(7);
plot(twin5,DToF, 'r-', 'LineWidth', 2); hold on;
plot(twin,FR_DToF, 'b-', 'LineWidth', 2); hold on;
set(gca,'ylim',[10^-4 2*10^0]);
legend({'Full Reconstituted TG-DToF', 'FR-DToF'},txt2{:});
legend boxoff;
set(gca,'yscale','log');
xlabel('Time (ns)',txt2{:})
ylabel('Norm. Counted Photons (#)',txt2{:})
title({'TG-DToF Curve vs. FR-DToF Curve','2.5 cm SDD'},txt1{:}) %
box on;
grid on;

```

Appendix II: COPYRIGHT PERMISSIONS

ELSEVIER LICENSE TERMS AND CONDITIONS

Nov 16, 2018

This Agreement between Mr. Mrwan Alayed ("You") and Elsevier ("Elsevier") consists of your license details and the terms and conditions provided by Elsevier and Copyright Clearance Center.

License Number	4430930950512
License date	Sep 16, 2018
Licensed Content Publisher	Elsevier
Licensed Content Publication	Seminars in Fetal and Neonatal Medicine
Licensed Content Title	Near-infrared spectroscopy: A methodology-focused review
Licensed Content Author	Adelina Pellicer, María del Carmen Bravo
Licensed Content Date	Feb 1, 2011
Licensed Content Volume	16
Licensed Content Issue	1
Licensed Content Pages	8
Start Page	42
End Page	49
Type of Use	reuse in a thesis/dissertation
Portion	figures/tables/illustrations
Number of figures/tables/illustrations	1
Format	both print and electronic
Are you the author of this Elsevier article?	No
Will you be translating?	No
Original figure numbers	Figure 1
Title of your thesis/dissertation	IMPROVING THE COMPUTATIONAL EFFICIENCY AND REDUCING THE COST AND THE SIZE FOR TIME-RESOLVED DIFFUSE OPTICAL SYSTEMS

Expected completion date	Dec 2018
Estimated size (number of pages)	120
Requestor Location	Mr. Mrwan Alayed 168 Plains Rd W Apartment: 504 Burlington, ON L7T 4M3 Canada Attn: Mr. Mrwan Alayed
Publisher Tax ID	GB 494 6272 12
Total	0.00 USD
Terms and Conditions	

INTRODUCTION

1. The publisher for this copyrighted material is Elsevier. By clicking "accept" in connection with completing this licensing transaction, you agree that the following terms and conditions apply to this transaction (along with the Billing and Payment terms and conditions established by Copyright Clearance Center, Inc. ("CCC"), at the time that you opened your Rightslink account and that are available at any time at <http://myaccount.copyright.com>).

GENERAL TERMS

2. Elsevier hereby grants you permission to reproduce the aforementioned material subject to the terms and conditions indicated.

3. Acknowledgement: If any part of the material to be used (for example, figures) has appeared in our publication with credit or acknowledgement to another source, permission must also be sought from that source. If such permission is not obtained then that material may not be included in your publication/copies. Suitable acknowledgement to the source must be made, either as a footnote or in a reference list at the end of your publication, as follows:

"Reprinted from Publication title, Vol /edition number, Author(s), Title of article / title of chapter, Pages No., Copyright (Year), with permission from Elsevier [OR APPLICABLE SOCIETY COPYRIGHT OWNER]." Also Lancet special credit - "Reprinted from The Lancet, Vol. number, Author(s), Title of article, Pages No., Copyright (Year), with permission from Elsevier."

4. Reproduction of this material is confined to the purpose and/or media for which permission is hereby given.

5. Altering/Modifying Material: Not Permitted. However figures and illustrations may be altered/adapted minimally to serve your work. Any other abbreviations, additions, deletions and/or any other alterations shall be made only with prior written authorization of Elsevier Ltd. (Please contact Elsevier at permissions@elsevier.com). No modifications can be made to any Lancet figures/tables and they must be reproduced in full.

6. If the permission fee for the requested use of our material is waived in this instance, please be advised that your future requests for Elsevier materials may attract a fee.

7. Reservation of Rights: Publisher reserves all rights not specifically granted in the combination of (i) the license details provided by you and accepted in the course of this licensing transaction, (ii) these terms and conditions and (iii) CCC's Billing and Payment terms and conditions.

8. License Contingent Upon Payment: While you may exercise the rights licensed immediately upon issuance of the license at the end of the licensing process for the transaction, provided that you have disclosed complete and accurate details of your proposed use, no license is finally effective unless and until full payment is received from you (either by publisher or by CCC) as provided in CCC's Billing and Payment terms and conditions. If full payment is not received on a timely basis, then any license preliminarily granted shall be deemed automatically revoked and shall be void as if never granted. Further, in the event that you breach any of these terms and conditions or any of CCC's Billing and Payment terms and conditions, the license is automatically revoked and shall be void as if never granted. Use of materials as described in a revoked license, as well as any use of the materials beyond the scope of an unrevoked license, may constitute copyright infringement and publisher reserves the right to take any and all action to protect its copyright in the materials.

9. Warranties: Publisher makes no representations or warranties with respect to the licensed material.

10. Indemnity: You hereby indemnify and agree to hold harmless publisher and CCC, and their respective officers, directors, employees and agents, from and against any and all claims arising out of your use of the licensed material other than as specifically authorized pursuant to this license.

11. No Transfer of License: This license is personal to you and may not be sublicensed, assigned, or transferred by you to any other person without publisher's written permission.

12. No Amendment Except in Writing: This license may not be amended except in a writing signed by both parties (or, in the case of publisher, by CCC on publisher's behalf).

13. Objection to Contrary Terms: Publisher hereby objects to any terms contained in any purchase order, acknowledgment, check endorsement or other writing prepared by you, which terms are inconsistent with these terms and conditions or CCC's Billing and Payment terms and conditions. These terms and conditions, together with CCC's Billing and Payment terms and conditions (which are incorporated herein), comprise the entire agreement between you and publisher (and CCC) concerning this licensing transaction. In the event of any conflict between your obligations established by these terms and conditions and those established by CCC's Billing and Payment terms and conditions, these terms and conditions shall control.

14. Revocation: Elsevier or Copyright Clearance Center may deny the permissions described in this License at their sole discretion, for any reason or no reason, with a full refund payable to you. Notice of such denial will be made using the contact information provided by you. Failure to receive such notice will not alter or invalidate the denial. In no event will Elsevier or Copyright Clearance Center be responsible or liable for any costs, expenses or damage incurred by you as a result of a denial of your permission request, other than a refund of the amount(s) paid by you to Elsevier and/or Copyright Clearance Center for denied permissions.

LIMITED LICENSE

The following terms and conditions apply only to specific license types:

15. **Translation:** This permission is granted for non-exclusive world **English** rights only unless your license was granted for translation rights. If you licensed translation rights you may only translate this content into the languages you requested. A professional

translator must perform all translations and reproduce the content word for word preserving the integrity of the article.

16. Posting licensed content on any Website: The following terms and conditions apply as follows: Licensing material from an Elsevier journal: All content posted to the web site must maintain the copyright information line on the bottom of each image; A hyper-text must be included to the Homepage of the journal from which you are licensing at <http://www.sciencedirect.com/science/journal/xxxxx> or the Elsevier homepage for books at <http://www.elsevier.com>; Central Storage: This license does not include permission for a scanned version of the material to be stored in a central repository such as that provided by Heron/XanEdu.

Licensing material from an Elsevier book: A hyper-text link must be included to the Elsevier homepage at <http://www.elsevier.com> . All content posted to the web site must maintain the copyright information line on the bottom of each image.

Posting licensed content on Electronic reserve: In addition to the above the following clauses are applicable: The web site must be password-protected and made available only to bona fide students registered on a relevant course. This permission is granted for 1 year only. You may obtain a new license for future website posting.

17. For journal authors: the following clauses are applicable in addition to the above:

Preprints:

A preprint is an author's own write-up of research results and analysis, it has not been peer-reviewed, nor has it had any other value added to it by a publisher (such as formatting, copyright, technical enhancement etc.).

Authors can share their preprints anywhere at any time. Preprints should not be added to or enhanced in any way in order to appear more like, or to substitute for, the final versions of articles however authors can update their preprints on arXiv or RePEc with their Accepted Author Manuscript (see below).

If accepted for publication, we encourage authors to link from the preprint to their formal publication via its DOI. Millions of researchers have access to the formal publications on ScienceDirect, and so links will help users to find, access, cite and use the best available version. Please note that Cell Press, The Lancet and some society-owned have different preprint policies. Information on these policies is available on the journal homepage.

Accepted Author Manuscripts: An accepted author manuscript is the manuscript of an article that has been accepted for publication and which typically includes author-incorporated changes suggested during submission, peer review and editor-author communications.

Authors can share their accepted author manuscript:

- immediately
 - via their non-commercial person homepage or blog
 - by updating a preprint in arXiv or RePEc with the accepted manuscript
 - via their research institute or institutional repository for internal institutional uses or as part of an invitation-only research collaboration work-group
 - directly by providing copies to their students or to research collaborators for their personal use

- for private scholarly sharing as part of an invitation-only work group on commercial sites with which Elsevier has an agreement
- After the embargo period
 - via non-commercial hosting platforms such as their institutional repository
 - via commercial sites with which Elsevier has an agreement

In all cases accepted manuscripts should:

- link to the formal publication via its DOI
- bear a CC-BY-NC-ND license - this is easy to do
- if aggregated with other manuscripts, for example in a repository or other site, be shared in alignment with our hosting policy not be added to or enhanced in any way to appear more like, or to substitute for, the published journal article.

Published journal article (JPA): A published journal article (PJA) is the definitive final record of published research that appears or will appear in the journal and embodies all value-adding publishing activities including peer review co-ordination, copy-editing, formatting, (if relevant) pagination and online enrichment.

Policies for sharing publishing journal articles differ for subscription and gold open access articles:

Subscription Articles: If you are an author, please share a link to your article rather than the full-text. Millions of researchers have access to the formal publications on ScienceDirect, and so links will help your users to find, access, cite, and use the best available version.

Theses and dissertations which contain embedded PJAs as part of the formal submission can be posted publicly by the awarding institution with DOI links back to the formal publications on ScienceDirect.

If you are affiliated with a library that subscribes to ScienceDirect you have additional private sharing rights for others' research accessed under that agreement. This includes use for classroom teaching and internal training at the institution (including use in course packs and courseware programs), and inclusion of the article for grant funding purposes.

Gold Open Access Articles: May be shared according to the author-selected end-user license and should contain a [CrossMark logo](#), the end user license, and a DOI link to the formal publication on ScienceDirect.

Please refer to Elsevier's [posting policy](#) for further information.

18. **For book authors** the following clauses are applicable in addition to the above: Authors are permitted to place a brief summary of their work online only. You are not allowed to download and post the published electronic version of your chapter, nor may you scan the printed edition to create an electronic version. **Posting to a repository:** Authors are permitted to post a summary of their chapter only in their institution's repository.

19. **Thesis/Dissertation:** If your license is for use in a thesis/dissertation your thesis may be submitted to your institution in either print or electronic form. Should your thesis be published commercially, please reapply for permission. These requirements include permission for the Library and Archives of Canada to supply single copies, on demand, of the complete thesis and include permission for Proquest/UMI to supply single copies, on

demand, of the complete thesis. Should your thesis be published commercially, please reapply for permission. Theses and dissertations which contain embedded PJAs as part of the formal submission can be posted publicly by the awarding institution with DOI links back to the formal publications on ScienceDirect.

Elsevier Open Access Terms and Conditions

You can publish open access with Elsevier in hundreds of open access journals or in nearly 2000 established subscription journals that support open access publishing. Permitted third party re-use of these open access articles is defined by the author's choice of Creative Commons user license. See our [open access license policy](#) for more information.

Terms & Conditions applicable to all Open Access articles published with Elsevier:

Any reuse of the article must not represent the author as endorsing the adaptation of the article nor should the article be modified in such a way as to damage the author's honour or reputation. If any changes have been made, such changes must be clearly indicated. The author(s) must be appropriately credited and we ask that you include the end user license and a DOI link to the formal publication on ScienceDirect.

If any part of the material to be used (for example, figures) has appeared in our publication with credit or acknowledgement to another source it is the responsibility of the user to ensure their reuse complies with the terms and conditions determined by the rights holder.

Additional Terms & Conditions applicable to each Creative Commons user license:

CC BY: The CC-BY license allows users to copy, to create extracts, abstracts and new works from the Article, to alter and revise the Article and to make commercial use of the Article (including reuse and/or resale of the Article by commercial entities), provided the user gives appropriate credit (with a link to the formal publication through the relevant DOI), provides a link to the license, indicates if changes were made and the licensor is not represented as endorsing the use made of the work. The full details of the license are available at <http://creativecommons.org/licenses/by/4.0>.

CC BY NC SA: The CC BY-NC-SA license allows users to copy, to create extracts, abstracts and new works from the Article, to alter and revise the Article, provided this is not done for commercial purposes, and that the user gives appropriate credit (with a link to the formal publication through the relevant DOI), provides a link to the license, indicates if changes were made and the licensor is not represented as endorsing the use made of the work. Further, any new works must be made available on the same conditions. The full details of the license are available at <http://creativecommons.org/licenses/by-nc-sa/4.0>.

CC BY NC ND: The CC BY-NC-ND license allows users to copy and distribute the Article, provided this is not done for commercial purposes and further does not permit distribution of the Article if it is changed or edited in any way, and provided the user gives appropriate credit (with a link to the formal publication through the relevant DOI), provides a link to the license, and that the licensor is not represented as endorsing the use made of the work. The full details of the license are available at <http://creativecommons.org/licenses/by-nc-nd/4.0>. Any commercial reuse of Open Access articles published with a CC BY NC SA or CC BY NC ND license requires permission from Elsevier and will be subject to a fee.

Commercial reuse includes:

- Associating advertising with the full text of the Article
- Charging fees for document delivery or access
- Article aggregation
- Systematic distribution via e-mail lists or share buttons

Posting or linking by commercial companies for use by customers of those companies.

20. Other Conditions:

v1.9

Questions? customercare@copyright.com or +1-855-239-3415 (toll free in the US) or +1-978-646-2777.

Dear Mrwan,

Thanks for your message. Sensors is an OA journal, authors hold the copyright of their publication. You could use freely the files if all co-authors agree.

If any other questions, let me know freely.

Kind regards,

Ms. Fanny Fang

Managing Editor

sensors@mdpi.com

Dear Mrwan Alayed,

Thank you for contacting The Optical Society.

For the use of material from Mrwan Alayed, Mohamed A. Naser, Ishaq Aden-Ali, and M. Jamal Deen, "Time-resolved diffuse optical tomography system using an accelerated inverse problem solver," Opt. Express 26, 963-979 (2018):

Because you are the author of the source paper from which you wish to reproduce material, OSA considers your requested use of its copyrighted materials to be permissible within the author rights granted in the Copyright Transfer Agreement submitted by the requester on acceptance for publication of his/her manuscript. It is requested that a complete citation of the original material be included in any publication. This permission assumes that the material was not reproduced from another source when published in the original publication.

While your publisher should be able to provide additional guidance, OSA prefers the below citation formats:

For citations in figure captions:

[Reprinted/Adapted] with permission from ref [x], [Publisher]. (with full citation in reference list)

For images without captions:

Journal Vol. #, first page (year published) An example: Opt. Express 26, 963 (2018)

As this article is published under the terms of the OSA Open Access Publishing Agreement, if the entire article is being included, the following message should be displayed at some prominent place near the article and include a working hyperlink to the online abstract in the OSA Journal:

© XXXX [year] Optical Society of America]. Users may use, reuse, and build upon the article, or use the article for text or data mining, so long as such uses are for non-commercial purposes and appropriate attribution is maintained. All other rights are reserved.

When adapting or otherwise creating a derivative version of an article published under OSAs OAPA, users must maintain attribution to the author(s) and the published article's title, journal citation, and DOI. Users should also indicate if changes were made and avoid any implication that the author or OSA endorses the use.

Please let me know if you have any questions.

Kind Regards,

Rebecca Robinson

August 13, 2018

Authorized Agent, The Optical Society

The Optical Society (OSA)

2010 Massachusetts Ave., NW

Washington, DC 20036 USA

www.osa.org

Dear Mrwan Alayed,

Thank you for contacting The Optical Society.

For the use of figures 2 and 3 from Agathe Puszka, Laura Di Sieno, Alberto Dalla Mora, Antonio Pifferi, Davide Contini, Gianluca Boso, Alberto Tosi, Lionel Hervé, Anne Planat-Chrétien, Anne Koenig, and Jean-Marc Dinten, "Time-resolved diffuse optical tomography using fast-gated single-photon avalanche diodes," Biomed. Opt. Express 4, 1351-1365 (2013):

OSA considers your requested use of its copyrighted material to be Fair Use under United States Copyright Law. It is requested that a complete citation of the original material be included in any publication.

While your publisher should be able to provide additional guidance, OSA prefers the below citation formats:

For citations in figure captions:

[Reprinted/Adapted] with permission from ref [x], [Publisher]. (with full citation in reference list)

For images without captions:

Journal Vol. #, first page (year published) An example: Biomed. Opt. Express 4, 1351 (2013)

Please let me know if you have any questions.

Kind Regards,

Rebecca Robinson

November 9, 2018

Authorized Agent, The Optical Society

The Optical Society (OSA)

2010 Massachusetts Ave., NW

Washington, DC 20036 USA

www.osa.org

REFERENCES

1. G. Gauglitz, D. Moore and eds., Handbook of spectroscopy, John Wiley & Sons, 2014.
2. C. Grupen, I. Buvat and eds., Handbook of particle detection and imaging, Springer Science & Business Media, 2011.
3. B. Stuart, Infrared Spectroscopy: Fundamentals and Applications, John Wiley & Sons: Analytical Techniques in the Sciences, 2004.
4. C. Hildebrandt, C. Raschner and K. Ammer, "An overview of recent application of medical infrared thermography in sports medicine in Austria," *Sensors*, vol. 10, no. 5, pp. 4700-4715, 2010.
5. "Radiation Dose in X-Ray and CT Exams," [Online]. Available: <https://www.radiologyinfo.org/en/info.cfm?pg=safety-xray>. [Accessed 22 09 2018].
6. G. Yu, T. Durduran, C. Zhou, R. Cheng and A. Yodh, "Near-infrared diffuse correlation spectroscopy for assessment of tissue blood flow," in *Handbook of Biomedical Optics*, CRC Press, 2011, pp. 195-216.
7. L. Pavesi, P. Fauchet and eds., Biophotonics, Springer Science & Business Media, 2008.
8. T. Jue and K. Masuda, Application of Near Infrared Spectroscopy in Biomedicine, Berlin: Springer, 2013.
9. T. Durduran, R. Choe, W. Baker and A. Yodh, "Diffuse optics for tissue monitoring and tomography," *Reports on Progress in Physics*, vol. 73, no. 7, p. 076701, 2010.
10. Y. Yamada and S. Okawa, "Diffuse optical tomography: present status and its future," *Optical Review*, vol. 21, no. 3, pp. 185-205, 2014.
11. H. Dehghani, S. Srinivasan, B. Pogue and A. Gibson, "Numerical modelling and image reconstruction in diffuse optical tomography," *Philosophical Transactions. Series A, Mathematical, Physical, and Engineering Sciences*, vol. 367, no. 1900, p. 3073–3093, 2009.
12. A. Gibson, J. Hebden and S. Arridge, "Recent advances in diffuse optical imaging," *Physics in medicine and biology*, vol. 50, no. 4, p. R1, 2005.
13. M. Ferrari and V. Quaresima, "A brief review on the history of human functional near-infrared spectroscopy (fNIRS) development and fields of application," *Neuroimage*, vol. 63, no. 2, pp. 921-935, 2012.
14. D. Davies, Z. Su, M. Clancy, S. Lucas, H. Dehghani, A. Logan and A. Belli, "Near-infrared spectroscopy in the monitoring of adult traumatic brain injury: a review," *Journal of neurotrauma*, vol. 32, no. 13, pp. 933-941, 2015.
15. A. Eggebrecht, S. Ferradal, A. Robichaux-Viehoever, M. Hassanpour, H. Dehghani, A. Snyder, T. Hershey and J. Culver, "Mapping distributed brain function and networks with diffuse optical tomography," *Nature photonics*, vol. 8, no. 6, pp. 448-454, 2014.
16. A. Torricelli, D. Contini, A. Pifferi, M. Caffini, R. Re, L. Zucchelli and L. Spinelli, "Time domain functional NIRS imaging for human brain mapping," *NeuroImage*, vol. 85, p. 28–50, 2014.
17. X. Zhou, L. Chen, C. Tse, T. Penney and N. Chen, "Theoretical investigation of near-infrared light path in multi-layer brain models for three DOT systems," in *Photonics Global Conference (PGC)*, 2012.
18. T. Svensson, E. Alerstam, D. Khoptyar, J. Johansson, S. Folestad and S. Andersson-Engels, "Near-infrared photon time-of-flight spectroscopy of turbid materials up to 1400 nm," *Review of scientific instruments*, vol. 80, no. 6, p. 063105, 2009.

19. S. Jacques, "Optical properties of biological tissues: a review," *Physics in Medicine & Biology*, vol. 58, no. 11, pp. R37-R61, 2013.
20. A. Gibson and H. Dehghani, "Diffuse optical imaging," *Philosophical Transactions of the Royal Society of London A: Mathematical, Physical and Engineering Sciences*, vol. 367, no. 1900, pp. 3055-3072, 2009.
21. A. Pifferi, D. Contini, A. Dalla Mora, A. Farina, L. Spinelli and A. Torricelli, "New frontiers in time-domain diffuse optics, a review," *Journal of Biomedical Optics*, vol. 21, no. 9, p. 091310, 2016.
22. J. Hebden, "Diffuse Optical Imaging," in *Handbook of Biophotonics*, Wiley-VCH Verlag GmbH and Co. KGaA, 2013.
23. M. Schweiger and S. Arridge, "The Toast++ software suite for forward and inverse modeling in optical tomography," *Journal of biomedical optics*, vol. 19, no. 4, p. 040801, 2014.
24. M. Naser and M. Deen, "Time-domain diffuse optical tomography using recursive direct method of calculating Jacobian at selected temporal points," *Biomedical Physics & Engineering Express*, vol. 1, no. 4, p. 045207, 2015.
25. M. Alayed and M. J. Deen, "Time-resolved diffuse optical spectroscopy and imaging using solid-state detectors: characteristics, present status, and research challenges," *Sensors*, vol. 17, no. 9, p. 2115, 2017.
26. S. Lloyd Fox, A. Blasi and C. E. Elwell, "Illuminating the developing brain: The past, present and future of functional near infrared spectroscopy," *Neuroscience and Biobehavioral Reviews*, vol. 34, no. 3, p. 269–284, 2010.
27. A. Pellicer and M. del Carmen Bravo, "Near-infrared spectroscopy: a methodology-focused review," *Seminars in fetal and neonatal medicine*, vol. 16, no. 1, pp. 42-49, February 2011.
28. F. Abdelnour, B. Schmidt and T. Huppert, "Topographic localization of brain activation in diffuse optical imaging using spherical wavelets," *Physics in medicine and biology*, vol. 54, no. 20, pp. 6383-6413, 2009.
29. G. Zaccanti, A. Taddeucci, M. Barilli, P. Brusciaglioni and F. Martelli, "Optical properties of biological tissues," in *Photonics West'95*, 1995.
30. P. Sawosz, M. Kacprzak, N. Zolek, W. Weigl, S. Wojtkiewicz, R. Maniewski and A. Liebert, "Optical system based on time-gated, intensified charge-coupled device camera for brain imaging studies," *Journal of biomedical optics*, vol. 15, no. 6, p. 066025, 2010.
31. R. Cooper, E. Magee, N. Everdell, S. Magazov, M. Varela, D. Airantzis, A. Gibson and J. Hebden, "MONSTIR II: A 32-channel, multispectral, time-resolved optical tomography system for neonatal brain imaging," *Review of Scientific Instruments*, vol. 85, no. 5, p. 053105, 2014.
32. H. Dehghani, B. Pogue, J. Shudong, B. Brooksby and K. Paulsen, "Three-dimensional optical tomography: resolution in small-object imaging," *Applied Optics*, vol. 42, no. 16, pp. 3117-3128, 2003.
33. E. Okada, "Photon Migration in NIRS Brain Imaging," in *Application of Near Infrared Spectroscopy in Biomedicine*, Springer US, 2013, pp. 37-58.
34. S. Arridge, "Optical tomography in medical imaging," *Inverse problems*, vol. 15, no. 2, p. R41, 1999.
35. E. Sultan, L. Najafizadeh, A. Gandjbakhche, K. Pourrezaei and A. Daryoush, "Accurate optical parameter extraction procedure for broadband near-infrared spectroscopy of brain matter," *Journal of biomedical optics*, vol. 18, no. 1, p. 017008, 2013.
36. A. Dalla Mora, D. Contini, S. Arridge, F. Martelli, A. Tosi, G. Boso, A. Farina, T. Durduran, E. Martinenghi, A. Torricelli and A. Pifferi, "Towards next generation time-domain diffuse optics devices," in *SPIE BiOS*, 2015.

37. D. Boas, . M. Anders and M. Franceschini, "Diffuse optical imaging of brain activation: Approaches to optimizing image sensitivity, resolution, and accuracy," *NeuroImage*, vol. 23, no. SUPPL. 1, pp. S275-S288, 2004.
38. J. Bouchard, I. Veilleux, R. Jedidi, I. Noiseux, M. Fortin and O. Mermut, "Reference optical phantoms for diffuse optical spectroscopy. Part 1--Error analysis of a time resolved transmittance characterization method," *Optics Express*, vol. 18, no. 11, p. 11495–11507, 2010.
39. H. Koizumi, T. Yamamoto, A. Maki, Y. Yamashita, H. Sato, H. Kawaguchi and N. Ichikawa, "Optical topography: practical problems and new applications," *Applied optics*, vol. 42, no. 16, pp. 3054-3062, 2003.
40. J. Chen, V. Venugopal, F. Lesage and X. Intes, "Time-resolved diffuse optical tomography with patterned-light illumination and detection," *Optics Letters*, vol. 35, no. 13, p. 2121–2123, 2010.
41. D. Goff, E. Buckley, T. Durduran, J. Wang and D. Licht, "Noninvasive cerebral perfusion imaging in high-risk neonates," *Seminars in perinatology*, vol. 34, no. 1, pp. 46-56, 2010.
42. T. Durduran, R. Choe, W. Baker and A. Yodh, "Diffuse optics for tissue monitoring and tomography," *Reports on Progress in Physics*, vol. 73, no. 7, p. 076701, 2010.
43. D. Boas, D. Brooks, E. Miller, C. DiMarzio, M. Kilmer, R. Gaudette and Q. Zhang, "Imaging the body with diffuse optical tomography," *IEEE signal processing magazine*, vol. 18, no. 6, pp. 57-75, 2001.
44. J. Wang, X. Liang, Q. Zhang, L. Fajardo and H. Jiang, "Automated breast cancer classification using near-infrared optical tomographic images," *Journal of biomedical optics*, vol. 13, no. 4, p. 044001, 2008.
45. J. Kwong, F. Nouizi, J. Cho, J. Zheng, Y. Li, J. Chen, M. Su and G. Gulsen, "Diffuse optical imaging of the breast using structured-light," in *SPIE BiOS. International Society for Optics and Photonics*, 2015.
46. O. Falou, H. Soliman, A. Sadeghi-Naini, S. Iradji, S. Lemon-Wong, J. Zubovits, J. Spayne, R. Dent, M. Trudeau, J. Boileau and F. Wright, "Diffuse optical spectroscopy evaluation of treatment response in women with locally advanced breast cancer receiving neoadjuvant chemotherapy," *Translational oncology*, vol. 5, no. 4, pp. 238-246, 2012.
47. D. Boas, C. Elwell, M. Ferrari and G. Taga, "Twenty years of functional near-infrared spectroscopy: Introduction for the special issue," *NeuroImage*, vol. 85, p. 1–5, 2014.
48. F. Martelli, S. Del Bianco, A. Ismaelli and G. Zaccanti, *Light propagation through biological tissue and other diffusive media: Theory, Solutions, and Software*, SPIE press, 2009.
49. L. Spinelli, F. Martelli, A. Farina, A. Pifferi, A. Torricelli, R. Cubeddu and G. Zaccanti, "Calibration of scattering and absorption properties of a liquid diffusive medium at NIR wavelengths. Time-resolved method," *Optics Express*, vol. 15, no. 11, pp. 6589-6604, 2007.
50. D. Boas, T. Gaudette, G. Strangman, X. Cheng, J. Marota and J. Mandeville, "The accuracy of near infrared spectroscopy and imaging during focal changes in cerebral hemodynamics," *Neuroimage*, vol. 13, no. 1, pp. 76-90, 2001.
51. A. Welch and M. e. Van Gemert, *Optical-thermal response of laser-irradiated tissue*, vol. 2, New York: Springer, 2011.
52. R. Cubeddu, A. Pifferi, P. Taroni, A. Torricelli and G. Valentini, "A solid tissue phantom for photon migration studies," *Physics in Medicine & Biology*, vol. 42, no. 10, p. 1971, 1997.
53. F. Gao, H. Zhao and Y. Yamada, "Improvement of image quality in diffuse optical tomography by use of full time-resolved data," *Applied Optics*, vol. 41, no. 4, p. 778–791, 2002.

54. J. Selb, D. Joseph and D. Boas, "Time-gated optical system for depth-resolved functional brain imaging," *Journal of Biomedical Optics*, vol. 11, no. 4, p. 044008, 2006.
55. P. Sawosz, N. Zolek, M. Kacprzak, R. Maniewski and A. Liebert, "Application of time-gated CCD camera with image intensifier in contactless detection of absorbing inclusions buried in optically turbid medium which mimics local changes in oxygenation of the brain tissue," *Opto-Electronics Review*, vol. 20, no. 4, pp. 309-314, 2012.
56. P. Taroni, A. Pifferi, E. Salvagnini, L. Spinelli, A. Torricelli and R. Cubeddu, "Seven-wavelength time-resolved optical mammography extending beyond 1000 nm for breast collagen quantification," *Optics express*, vol. 17, no. 18, pp. 15932-15946, 2009.
57. R. Re, D. Contini, M. Turola, L. Spinelli, L. Zucchelli, M. Caffini, R. Cubeddu and A. Torricelli, "Multi-channel medical device for time domain functional near infrared spectroscopy based on wavelength space multiplexing," *Biomedical optics express*, vol. 4, no. 10, pp. 2231-2246, 2013.
58. A. Puszka, L. Hervé, A. Planat-Chrétien, A. Koenig, J. Derouard and J. Dinten, "Time-domain reflectance diffuse optical tomography with Mellin-Laplace transform for experimental detection and depth localization of a single absorbing inclusion," *Biomedical Optics Express*, vol. 4, no. 4, p. 569–583, 2013.
59. J. Selb, B. Zimmermann, M. Martino, T. Ogden and D. Boas, "Functional brain imaging with a supercontinuum time-domain NIRS system," in *Proc. SPIE*, 2013.
60. A. Tosi, A. Dalla Mora, F. Zappa, A. Gulinatti, D. Contini, A. Pifferi, L. Spinelli, A. Torricelli and R. Cubeddu, "Fast-gated single-photon counting technique widens dynamic range and speeds up acquisition time in time- resolved measurements," *Optics express*, vol. 19, no. 11, pp. 10735-10746, 2011.
61. A. Dalla Mora, D. Contini, S. Arridge, F. Martelli, A. Tosi, G. Boso, A. Farina, T. Durduran, E. Martinenghi, A. Torricelli and A. Pifferi, "Towards next-generation time-domain diffuse optics for extreme depth penetration and sensitivity," *Biomedical optics express*, vol. 6, no. 5, pp. 1749-1760, 2015.
62. D. Contini, A. Torricelli, A. Pifferi, L. Spinelli, F. Paglia and R. Cubeddu, "Multi-channel time-resolved system for functional near infrared spectroscopy," *Optics Express*, vol. 14, no. 12, pp. 5418-5432, 2006.
63. R. Hunter, M. Patterson, T. Farrell and J. Hayward, "Haemoglobin oxygenation of a two-layer tissue-simulating phantom from time-resolved reflectance: effect of top layer thickness," *Physics in medicine and biology*, vol. 47, no. 2, p. 193, 2002.
64. Q. Zhao, L. Spinelli, A. Bassi, G. Valentini, D. Contini, A. Torricelli, R. Cubeddu, G. Zaccanti, F. Martelli and A. Pifferi, "Functional tomography using a time-gated ICCD camera," *Biomedical Optics Express*, vol. 2, no. 3, p. 705–716, 2011.
65. "Advanced Laser Diode Systems A.L.S. GmbH," [Online]. Available: <http://www.alsgmbh.com/pilas.html>. [Accessed 15 12 2016].
66. "ALPHALAS GmbH," [Online]. Available: <http://www.alphalas.com/products/lasers/picosecond-pulse-diode-lasers-with-driver-picopower-ld-series.html>. [Accessed 11 09 2016].
67. "Becker & Hickl GmbH," [Online]. Available: <http://www.becker-hickl.de/lasers.htm#BHLP-700>. [Accessed 11 12 2016].
68. "Picosecond Pulsed Sources," PicoQuant, [Online]. Available: <https://www.picoquant.com/products/category/picosecond-pulsed-sources/ldh-series-picosecond-pulsed-diode-laser-heads>. [Accessed 17 04 2018].
69. I. E. Commission, Safety of laser products Part 1: Equipment classification and requirements, Vols. BS EN 60825-1:2014, The British Standards Institution, 2014.
70. Y. Garini and E. Tauber, "Spectral Imaging: Methods, Design, and Applications," Berlin Heidelberg, Springer, 2013, pp. 111-161.

71. "Measuring Laser Power and Energy Output," [Online]. Available: <https://www.coherent.com/>.
72. F. Martelli, S. Del Bianco, L. Spinelli, S. Cavalieri, P. Di Ninni, T. Binzoni, A. Jelzow, R. Macdonald and H. Wabnitz, "Optimal estimation reconstruction of the optical properties of a two-layered tissue phantom from time-resolved single-distance measurements," *Journal of biomedical optics*, vol. 20, no. 11, p. 115001, 2015.
73. Y. Fukui, Y. Ajichi and E. Okada, "Monte Carlo prediction of near-infrared light propagation in realistic adult and neonatal head models," *Applied optics*, vol. 42, no. 16, pp. 2881-2887, 2003.
74. B. Pogue and M. Patterson, "Review of tissue simulating phantoms for optical spectroscopy, imaging and dosimetry," *Journal of biomedical optics*, vol. 11, no. 4, p. 041102, 2006.
75. Y. Bérubé-Lauzière, M. Crotti, S. Boucher, S. Ettehad, J. Pichette and I. Rech, "Prospects on time-domain diffuse optical tomography based on time-correlated single photon counting for small animal imaging," *Journal of Spectroscopy*, vol. 2016, 2016.
76. B. Das, K. Yoo and R. Alfano, "Ultrafast time-gated imaging in thick tissues: a step toward optical mammography," *Optics Letters*, vol. 18, no. 13, pp. 1092-1094, 1993.
77. S. Mottin, B. Montcel, H. De Chatellus and S. Ramstein, "Functional white-laser imaging to study brain oxygen uncoupling/recoupling in songbirds," *Journal of Cerebral Blood Flow & Metabolism*, vol. 31, no. 2, pp. 393-400, 2011.
78. J. Hebden, M. Varela, S. Magazov, N. Everdell, A. Gibson, J. Meek and T. Austin, "Diffuse optical imaging of the newborn infant brain," in *Biomedical Imaging (ISBI), 9th IEEE International Symposium*, 2012.
79. B. Montcel, R. Chabrier and P. Poulet, "Detection of cortical activation with time-resolved diffuse optical methods," *Applied Optics*, vol. 44, no. 10, pp. 1942-1947, 2005.
80. L. Di Sieno, D. Contini, A. Dalla Mora, A. Torricelli, L. Spinelli, R. Cubeddu, A. Tosi, G. Boso and A. Pifferi, "Functional near-infrared spectroscopy at small source-detector distance by means of high dynamic-range fast-gated SPAD acquisitions: First in-vivo measurements," in *European Conference on Biomedical Optics*, 2013.
81. A. Cuccato, S. Antonioli, M. Crotti, I. Labanca, A. Gulinatti, I. Rech and M. Ghioni, "Complete and compact 32-channel system for time-correlated single-photon counting measurements," *IEEE Photonics Journal*, vol. 5, no. 5, p. 6801514, 2013.
82. L. Di Sieno, J. Zouaoui, L. Hervé, A. Pifferi, A. Farina, E. Martinenghi, J. Derouard, J. Dinten and A. Dalla Mora, "Time-domain diffuse optical tomography using silicon photomultipliers: feasibility study," *Journal of Biomedical Optics*, vol. 21, no. 11, p. 116002, 2016.
83. M. Buttafava, E. Martinenghi, D. Tamborini, D. Contini, A. Dalla Mora, M. Renna, A. Torricelli, A. Pifferi, F. Zappa and A. Tosi, "A compact two-wavelength time-domain NIRS system based on SiPM and pulsed diode lasers," *IEEE Photonics Journal*, vol. 9, no. 1, pp. 1-14, 2017.
84. A. Dalla Mora, A. Tosi, F. Zappa, S. Cova, D. Contini, A. Pifferi, L. Spinelli, A. Torricelli and R. Cubeddu, "Fast-gated single-photon avalanche diode for wide dynamic range near infrared spectroscopy," *IEEE Journal of Selected Topics in Quantum Electronics*, vol. 16, no. 4, pp. 1023-1030, 2010.
85. L. Spinelli, F. Martelli, S. Del Bianco, A. Pifferi, A. Torricelli, R. Cubeddu and G. Zaccanti, "Absorption and scattering perturbations in homogeneous and layered diffusive media probed by time-resolved reflectance at null source-detector separation," *Physical Review E*, vol. 74, no. 2, p. 021919, 2006.
86. Q. Fang and D. Boas, "Monte Carlo simulation of photon migration in 3D turbid media accelerated by graphics processing units," *Optics express*, vol. 17, no. 22, pp. 20178-20190, 2009.

87. P. Poulet, W. Uhring, W. Hanselmann, R. Glazenborg, F. Nouizi, V. Zint and W. Hirschi, "A time-gated near-infrared spectroscopic imaging device for clinical applications," in *Proc. SPIE*, 2013.
88. G. Mitic, J. Kölzer, J. Otto, E. Plies, G. Sölkner and W. Zinth, "Time-gated transillumination of biological tissues and tissuelike phantoms," *Applied optics*, vol. 33, no. 28, pp. 6699-6710, 1994.
89. S. Del Bianco, F. Martelli and G. Zaccanti, "Penetration depth of light re-emitted by a diffusive medium: theoretical and experimental investigation," *Physics in medicine and biology*, vol. 47, no. 23, p. 4131-4144, 2002.
90. W. Becker, *Advanced time-correlated single photon counting applications*, Springer International Publishing, 2015.
91. H. Wabnitz, A. Pifferi, A. Torricelli, D. Taubert, M. Mazurenka, O. Steinkellner, A. Jelzow, A. Farina, I. Bargigia, D. Contini and M. Caffini, "Assessment of basic instrumental performance of time-domain optical brain imagers," in *Proc. SPIE*, 2011.
92. J. Arlt, D. Tyndall, B. Rae, D. Li, J. Richardson and R. Henderson, "A study of pile-up in integrated time-correlated single photon counting systems," *Review of Scientific Instruments*, vol. 84, no. 10, p. 103105, 2013.
93. W. Becker, A. Bergmann, A. Gibson, N. Everdell, D. Jennions, M. Schweiger, S. Arridge and J. Hebden, "Multi-dimensional time-correlated single photon counting applied to diffuse optical tomography," in *Proc. SPIE*, 2005.
94. "TCSPC and Time Tagging Electronics," [Online]. Available: <http://www.picoquant.com/products/category/tcspc-and-time-tagging-modules>. [Accessed 13 09 2016].
95. "TCSPC Modules," [Online]. Available: <http://www.becker-hickl.de/tcspc.htm>. [Accessed 13 09 2016].
96. J. Richardson, R. Walker, L. Grant, D. Stoppa, F. Borghetti, E. Charbon, M. Gersbach and R. Henderson, "A 32x32 50ps resolution 10 bit time to digital converter array in 130nm CMOS for time correlated imaging," in *Proceedings of the Custom Integrated Circuits Conference*, 2009.
97. M. Gersbach, Y. Maruyama, R. Trimananda, M. Fishburn, D. Stoppa, J. Richardson, R. Walker, R. Henderson and E. Charbon, "A time-resolved, low-noise single-photon image sensor fabricated in deep-submicron CMOS technology," *IEEE Journal of Solid-State Circuits*, vol. 47, no. 6, p. 1394-1407, 2012.
98. M. Patterson, B. Chance and B. Wilson, "Time resolved reflectance and transmittance for the noninvasive measurement of tissue optical properties," *Applied optics*, vol. 28, no. 12, pp. 2331-2336, 1989.
99. B. Chance, S. Nioka, J. Kent, K. McCully, M. Fountain, R. Greenfeld and G. Holtom, "Time-resolved spectroscopy of hemoglobin and myoglobin in resting and ischemic muscle," *Analytical biochemistry*, vol. 174, no. 2, pp. 698-707, 1988.
100. V. Ntziachristos and B. Chance, "Accuracy limits in the determination of absolute optical properties using time-resolved NIR spectroscopy," *Medical physics*, vol. 28, no. 6, pp. 1115-1124, 2001.
101. B. Khan, C. Wildey, R. Francis, F. Tian, M. Romero, M. Delgado, N. Clegg, L. Smith, H. Liu, D. MacFarlane and G. Alexandrakis, "Functional near infrared brain imaging with a brush-fiber optode to improve optical contact on subjects with dense hair," in *Photonic Therapeutics and Diagnostics VII*, vol. 7883, International Society for Optics and Photonics, 2011, p. 78834V.
102. F. Nouizi, M. Torregrossa, R. Chabrier and P. Poulet, "Improvement of absorption and scattering discrimination by selection of sensitive points on temporal profile in diffuse optical tomography," *Optics Express*, vol. 19, no. 13, p. 12843-12854, 2011.

103. S. Jacques and B. Pogue, "Tutorial on diffuse light transport ," *Journal of biomedical optics*, vol. 13, no. 4, pp. 041302 (1-19), 2008.
104. S. Arridge and J. Schotland, "Optical tomography: forward and inverse problems," *Inverse Problems*, vol. 25, no. 12, p. 123010, 2009.
105. H. Wabnitz, D. Taubert, M. Mazurenka, O. Steinkellner, A. Jelzow, R. Macdonald, D. Milej, P. Sawosz, M. Kacprzak, A. Liebert and R. Cooper, "Performance assessment of time-domain optical brain imagers, part 1: basic instrumental performance protocol," *Journal of biomedical optics*, vol. 19, no. 8, p. 086010, 2014.
106. A. Pifferi, A. Torricelli, A. Bassi, P. Taroni, R. Cubeddu, H. Wabnitz, D. Grosenick, M. Möller, R. Macdonald, J. Swartling and T. Svensson, "Performance assessment of photon migration instruments: the MEDPHOT protocol," *Applied Optics*, vol. 44, no. 11, p. 2104–2114, 2005.
107. H. Wabnitz, A. Jelzow, M. Mazurenka, O. Steinkellner, R. Macdonald, D. Milej, N. Żołek, M. Kacprzak, P. Sawosz, R. Maniewski and A. Liebert, "Performance assessment of time-domain optical brain imagers, part 2: nEUROpt protocol," *Journal of biomedical optics*, vol. 19, no. 8, p. 086012, 2014.
108. R. Re, E. Martinenghi, A. Dalla Mora, D. Contini, A. Pifferi and A. Torricelli, "Probe-hosted silicon photomultipliers for time-domain functional near-infrared spectroscopy: Phantom and in vivo tests," *Neurophotonics*, vol. 3, no. 4, p. 045004, 2016.
109. D. Bronzi, F. Villa, S. Tisa, A. Tosi and F. Zappa, "SPAD Figures of merit for photon-counting, photon-timing, and imaging applications: A review," *Sensors Journal*, vol. 16, no. 1, pp. 3-12, 2016.
110. E. Charbon, "Single Photon Imaging in CMOS," in *Lasers and Electro-Optics Society, 2006. LEOS 2006. 19th Annual Meeting of the IEEE*, 2006.
111. D. Bronzi, F. Villa, S. Bellisai, S. Tisa, G. Ripamonti and A. Tosi, "Figures of merit for CMOS SPADs and arrays," in *Proc. SPIE*, 2013.
112. D. P. Palubiak and M. J. Deen, "CMOS SPADs: Design Issues and Research Challenges for Detectors, Circuits, and Arrays," *IEEE Journal on Selected Topics in Quantum Electronics*, vol. 20, no. 6, pp. 409-426, 2014.
113. F. Villa, D. Bronzi, Y. Zou, C. Scarcella, G. Boso, S. Tisa, A. Tosi, F. Zappa, D. Durini, S. Weyers and U. Paschen, "CMOS SPADs with up to 500 μm diameter and 55% detection efficiency at 420 nm," *Journal of Modern Optics*, vol. 61, no. 2, pp. 102-115, 2014.
114. C. Niclass, M. Sergio and E. Charbon, "A single photon avalanche diode array fabricated in 0.35- μm CMOS and based on an event-driven readout for TCSPC experiments," in *Optics East*, 2006.
115. E. Martinenghi, L. Di Sieno, D. Contini, M. Sanzaro, A. Pifferi and A. Dalla Mora, "Time-resolved single-photon detection module based on silicon photomultiplier: A novel building block for time-correlated measurement systems," *Review of Scientific Instruments*, vol. 87, no. 7, p. 073101, 2016.
116. W. Becker, *The bh TCSPC handbook*, Becker and Hickl, 2014.
117. H. Wabnitz, M. Moeller, A. Liebert, A. Walter, R. Macdonald, H. Obrig, J. Steinbrink, R. Erdmann and O. Raitza, "A time-domain NIR brain imager applied in functional stimulation experiments," in *European Conference on Biomedical Optics*, 2005.
118. M. Wahl, "Time-correlated single photon counting. Technical Note.," PicoQuant GmbH, Berlin, Germany, 2009.
119. E. Hillman, J. Hebden, M. Schweiger, H. Dehghani, F. Schmidt, D. Delpy and S. Arridge, "Time resolved optical tomography of the human forearm," *Physics in medicine and biology*, vol. 46, no. 4, pp. 1117-1130, 2001.

120. A. Liebert, H. Wabnitz, D. Grosenick and R. Macdonald, "Fiber dispersion in time domain measurements compromising the accuracy of determination of optical properties of strongly scattering media," *Journal of Biomedical Optics*, vol. 8, no. 3, p. 512–516, 2003.
121. A. Dalla Mora, E. Martinenghi, D. Contini, A. Tosi, G. Boso, T. Durduran, S. Arridge, F. Martelli, A. Farina, A. Torricelli and A. Pifferi, "Fast silicon photomultiplier improves signal harvesting and reduces complexity in time-domain diffuse optics," *Optics express*, vol. 23, no. 11, pp. 13937-13946, 2015.
122. H. Wabnitz, A. Jelzow, M. Mazurenka, O. Steinkellner, R. Macdonald, A. Pifferi, A. Torricelli, D. Contini, L. Zucchelli, L. Spinelli and R. Cubeddu, "Performance assessment of time-domain optical brain imagers: a multi-laboratory study," in *SPIE BiOS*, 2013.
123. M. Eisaman, J. Fan, A. Migdall and S. Polyakov, "Invited review article: Single-photon sources and detectors," *Review of scientific instruments*, vol. 82, no. 7, p. 071101, 2011.
124. A. Sultana, E. Kamrani and M. Sawan, "CMOS silicon avalanche photodiodes for NIR light detection: a survey," *Analog Integrated Circuits and Signal Processing*, vol. 70, no. 1, pp. 1-13, 2012.
125. D. Palubiak, M. El-Desouki, O. Marinov, M. Deen and Q. Fang, "High-speed, single-photon avalanche-photodiode imager for biomedical applications," *IEEE Sensors Journal*, vol. 11, no. 10, pp. 2401-2412, 2011.
126. R. Liang, *Biomedical optical imaging technologies: design and applications*, Springer Science & Business Media, 2012.
127. R. Maniewski, A. Liebert and M. Kacprzak, "Time resolved optical spectroscopy system for cerebral oxygenation imaging," in *Engineering in Medicine and Biology 27th Annual Conference*, 2005.
128. A. Liebert, H. Wabnitz, D. Grosenick, M. Möller, R. Macdonald and H. Rinneberg, "Evaluation of optical properties of highly scattering media by moments of distributions of times of flight of photons," *Applied optics*, vol. 42, no. 28, pp. 5785-5792, 2003.
129. G. Boso, A. Dalla Mora, A. Della Frera and A. Tosi, "Fast-gating of single-photon avalanche diodes with 200 ps transitions and 30 ps timing jitter," *Sensors and Actuators, A: Physical*, vol. 191, p. 61–67, 2013.
130. J. Pavia, M. Scandini, S. Lindner, M. Wolf and E. Charbon, "A 1×400 Backside-Illuminated SPAD Sensor with 49.7 ps Resolution, 30 pJ/Sample TDCs Fabricated in 3D CMOS Technology for Near-Infrared Optical Tomography," *IEEE Journal of Solid-State Circuits*, vol. 50, no. 10, p. 2406–2418, 2015.
131. M. Deen and P. Basu, *Silicon Photonics: Fundamentals and Devices*, Chichester, UK: Wiley, 2012.
132. [Online]. Available: <https://www.pveducation.org/pvcdrom/absorption-coefficient>. [Accessed 16 08 2018].
133. M. Ghioni, G. Armellini, P. Maccagnani, I. Rech, M. Emsley and M. Ünlü, "Resonant-cavity-enhanced single photon avalanche diodes on double silicon-on-insulator substrates," *Journal of Modern Optics*, vol. 56, no. 2-3, pp. 309-316, 2009.
134. F. Zappa, S. Tisa, A. Tosi and S. Cova, "Principles and features of single-photon avalanche diode arrays," *Sensors and Actuators A: Physical*, vol. 140, no. 1, pp. 103-112, 2007.
135. C. Veerappan, J. Richardson, R. Walker, D. Li, M. Fishburn, Y. Maruyama, D. Stoppa, F. Borghetti, M. Gersbach, R. Henderson and E. Charbon, "A 160x128 single- photon image sensor with on-pixel 55ps 10b time-to-digital converter," in *Solid-State Circuits Conference Digest of Technical Papers (ISSCC)*, San Francisco, Calif, USA, February 2011.
136. Z. Li and M. Deen, "Towards a portable Raman spectrometer using a concave grating and a time-gated CMOS SPAD," *Optics express*, vol. 22, no. 15, pp. 18736-18747, 2014.

137. D. Tyndall, B. Rae, D. Li, J. Arlt, A. Johnston, J. Richardson and R. Henderson, "A high-throughput time- resolved mini-silicon photomultiplier with embedded fluorescence lifetime estimation in 0.13 micro-m CMOS," *IEEE Transactions on Biomedical Circuits and Systems*, vol. 6, no. 6, p. 562–570, 2012.
138. F. Villa, B. Markovic, S. Bellisai, D. Bronzi, A. Tosi, F. Zappa, S. Tisa, D. Durini, S. Weyers, U. Paschen and W. Brockherde, "SPAD smart pixel for time-of-flight and time-correlated single-photon counting measurements," *IEEE Photonics Journal*, vol. 4, no. 3, p. 795– 804, 2012.
139. D. Stoppa, F. Borghetti, J. Richardson, R. Walker, L. Grant, R. Henderson, M. Gersbach and E. Charbon, "A 32×32-pixel array with in-pixel photon counting and arrival time measurement in the analog domain," in *35th European Solid State Circuits Conference*, Athens, Greece, September 2009.
140. C. Niclass, C. Favi, T. Kluter, M. Gersbach and E. Charbon, "A 128 × 128 single-photon image sensor with column-level 10-bit time-to-digital converter array," *IEEE Journal of Solid-State Circuits*, vol. 43, no. 12, p. 2977–2989, 2008.
141. M. Ghioni, A. Gulinatti, P. Maccagnani, I. Rech and S. Cova, "Planar silicon SPADs with 200- μm diameter and 35-ps photon timing resolution," in *Optics East*, 2006.
142. A. Rochas, M. Gani, B. Furrer, P. Besse, R. Popovic, G. Ribordy and N. Gisin, "Single photon detector fabricated in a complementary metal–oxide–semiconductor high-voltage technology," *Rev. Science Instrument*, vol. 74, no. 7, pp. 3263-3270, 2003.
143. "Single Photon Counting Modules (SPCM)," Excelitas Technologies, [Online]. Available: <http://www.excelitas.com/Pages/Product/Single-Photon-Counting-Modules-SPCM.aspx>. [Accessed 20 03 2017].
144. A. Giudice, M. Ghioni, R. Biasi, F. Zappa, S. Cova, P. Maccagnani and A. Gulinatti, "High-rate photon counting and picosecond timing with silicon-SPAD based compact detector modules," *Journal of Modern Optics*, vol. 54, no. 2-3, pp. 225-237, 2007.
145. E. Martinenghi, A. Dalla Mora, D. Contini, A. Farina, F. Villa, A. Torricelli and A. Pifferi, "Spectrally resolved single-photon timing of silicon photomultipliers for time-domain diffuse spectroscopy," *IEEE Photonics Journal*, vol. 7, no. 4, pp. 1-12, 2015.
146. T. Frach, G. Prescher, C. Degenhardt, R. de Gruyter, A. Schmitz and R. Ballizany, "The digital silicon photomultiplier—Principle of operation and intrinsic detector performance," in *IEEE Nuclear Science Symposium Conference Record (NSS/MIC)*, 2009.
147. S. Mandai and E. Charbon, "Multi-channel digital SiPMs: Concept, analysis and implementation," in *Nuclear Science Symposium and Medical Imaging Conference (NSS/MIC)*, 2012.
148. M. Mazurenka, L. Di Sieno, G. Boso, D. Contini, A. Pifferi, A. Dalla Mora, A. Tosi, H. Wabnitz and R. Macdonald, "Non-contact in vivo diffuse optical imaging using a time-gated scanning system," *Biomedical optics express*, vol. 4, no. 10, pp. 2257-2268, 2013.
149. C. Scarcella, A. Tosi, F. Villa, S. Tisa and F. Zappa, "Low-noise low-jitter 32-pixels CMOS single-photon avalanche diodes array for single-photon counting from 300 nm to 900 nm," *Review of Scientific Instruments*, vol. 84, no. 12, pp. 123112 (1-5), 2013.
150. D. Palubiak, Z. Li and M. Deen, "Afterpulsing characteristics of free-running and time-gated single-photon avalanche diodes in 130-nm CMOS," *IEEE Transactions on Electron Devices*, vol. 62, no. 11, pp. 3727-3733, 2015.
151. D. Contini, A. Dalla Mora, L. Spinelli, A. Farina, A. Torricelli, R. Cubeddu, F. Martelli, G. Zaccanti, A. Tosi, G. Boso and F. Zappa, "Effects of time-gated detection in diffuse optical imaging at short source-detector separation," *Journal of Physics D: Applied Physics*, vol. 48, no. 4, p. 045401, 2015.
152. "PDM," [Online]. Available: <http://www.micro-photon-devices.com/Products/Photon-Counters/PDM>. [Accessed 01 12 2016].

153. A. Gulinatti, P. Maccagnani, I. Rech, M. Ghioni and S. Cova, "35 ps time resolution at room temperature with large area single photon avalanche diodes," *Electronics Letters*, vol. 41, no. 5, pp. 272-274, 2005.
154. J. Pavia, M. Wolf and E. Charbon, "Single-photon avalanche diode imagers applied to near-infrared imaging," *IEEE Journal on Selected Topics in Quantum Electronics*, vol. 20, no. 6, pp. 291-298, 2014.
155. "Silicon Photomultipliers with 1x1 mm² active area," [Online]. Available: http://www.excelitas.com/Downloads/DTS_C30742-11-050_Series_SiPM.pdf. [Accessed 2017].
156. "MPPC (multi-pixel photon counter) - S10362-11series," [Online]. Available: <https://www.hamamatsu.com/us/en/product/category/3100/4004/index.html>.
157. A. Dalla Mora, A. Tosi, D. Contini, L. Di Sieno, G. Boso, F. Villa and A. Pifferi, "Memory effect in silicon time-gated single-photon avalanche diodes," *Journal of Applied Physics*, vol. 117, no. 11, p. 114501, 2015.
158. Z. Cheng, X. Zheng, M. Deen and H. Peng, "Recent developments and design challenges of high-performance ring oscillator CMOS time-to-digital converters," *IEEE Transactions on Electron Devices*, vol. 63, no. 1, pp. 235-251, 2016.
159. L. Di Sieno, A. B. G. T. A. Dalla Mora, A. Pifferi, R. Cubeddu and D. Contini, "Diffuse optics using a dual window fast-gated counter," *Applied optics*, vol. 53, no. 31, pp. 7394-7401, 2014.
160. A. Jha, M. Kupinski, T. Masumura, E. Clarkson, A. Maslov and H. Barrett, "Simulating photon-transport in uniform media using the radiative transport equation: a study using the Neumann-series approach," *JOSA A*, vol. 29, no. 8, pp. 1741-1757, 2012.
161. M. Guven, B. Yazici, X. Intes and B. Chance, "Diffuse optical tomography with a priori anatomical information," *Physics in Medicine and Biology*, vol. 50, no. 12, p. 2837, 2005.
162. P. Yalavarthy, B. Pogue, H. Dehghani and K. Paulsen, "Weight-matrix structured regularization provides optimal generalized least-squares estimate in diffuse optical tomography," *Medical physics*, vol. 34, no. 6, pp. 2085-2098, 2007.
163. "Fiber Coupling," picoquant, [Online]. Available: <https://www.picoquant.com/products/category/picosecond-pulsed-sources/ldh-series-picosecond-pulsed-diode-laser-heads#custom2>. [Accessed 14 11 2017].
164. "0.22NA VIS/NIR Patchcord 1000 Micron Fiber w/ FC Connector," Edmund Optics Inc., [Online]. Available: <https://www.edmundoptics.com/optics/fiber-optics/0.22na-visnir-patchcord-1000-micron-fiber-w-fc-connector/#description>. [Accessed 20 08 2017].
165. "Stepper Motor with Cable," [Online]. Available: <https://www.sparkfun.com/products/9238>. [Accessed 11 07 2017].
166. M. Naser, "Improving the reconstruction image contrast of time-domain diffuse optical tomography using high accuracy Jacobian matrix," *Biomedical Physics & Engineering Express*, vol. 2, no. 1, p. 015015, 2016.
167. "Huntsman," [Online]. Available: http://www.huntsman.com/advanced_materials/a/Home. [Accessed 15 6 2017].
168. "Sigma-Aldrich Co. LLC," [Online]. Available: <http://www.sigmaaldrich.com/united-states.html>.
169. M. Diop and K. Lawrence, "Deconvolution method for recovering the photon time-of-flight distribution from time-resolved measurements," *Optics letters*, vol. 37, no. 12, pp. 2358-2360, 2012.
170. E. Hillman, J. Hebden, F. Schmidt, S. Arridge, M. Schweiger, H. Dehghani and D. Delpy, "Calibration techniques and datatype extraction for time-resolved optical tomography," *Review of Scientific Instruments*, vol. 71, no. 9, pp. 3415-3427, 2000.
171. Q. Fang and D. Boas, "Tetrahedral mesh generation from volumetric binary and grayscale images," in *International Symposium on Biomedical Imaging (ISBI'09)*, 2009.

172. M. Brambilla, L. Spinelli, A. Pifferi, T. A. and R. Cubeddu, "Time-resolved scanning system for double reflectance and transmittance fluorescence imaging of diffusive media," *Review of Scientific Instruments*, vol. 79, no. 1, p. 013103, 2008.
173. A. Pifferi, A. Torricelli, P. Taroni, D. Comelli, A. Bassi and R. Cubeddu, "Fully automated time domain spectrometer for the absorption and scattering characterization of diffusive media," *Review of scientific instruments*, vol. 78, no. 5, p. 053103, 2007.
174. J. Selb, J. Stott, M. Franceschini, A. Sorensen and D. Boas, "Improved sensitivity to cerebral hemodynamics during brain activation with a time-gated optical system: analytical model and experimental validation," *Journal of biomedical optics*, vol. 10, no. 1, p. 011013, 2005.
175. M. Alayed, M. Naser, I. Aden-Ali and M. Deen, "Time-resolved diffuse optical tomography system using an accelerated inverse problem solver," *Optics Express*, vol. 26, no. 2, pp. 963-979, 2018.
176. E. Hillman, "Optical brain imaging in vivo: techniques and applications from animal to man," *Journal of biomedical optics*, vol. 12, no. 5, p. 051402, 2007.
177. C. Bruschini, H. Homulle and E. Charbon, "Ten years of biophotonics single-photon SPAD imager applications: retrospective and outlook," *Multiphoton Microscopy in the Biomedical Sciences*, vol. 10069, p. 100691S, 2017.
178. M. Ghioni, A. Gulinatti, I. Rech, F. Zappa and S. Cova, "Progress in silicon single-photon avalanche diodes," *IEEE Journal of selected topics in quantum electronics*, vol. 13, no. 4, pp. 852-862, 2007.
179. M. Lee, A. Ximenes, P. Padmanabhan, T. Wang, K. Huang, Y. Yamashita, D. Yaung and E. Charbon, "High-Performance Back-Illuminated Three-Dimensional Stacked Single-Photon Avalanche Diode Implemented in 45-nm CMOS Technology," *IEEE Journal of Selected Topics in Quantum Electronics*, vol. 24, no. 6, pp. 1-9, 2018.
180. Z. Cheng, D. Palubiak, X. Zheng, M. Deen and H. Peng, "Impact of silicide layer on single photon avalanche diodes in a 130 nm CMOS process," *Journal of Physics D: Applied Physics*, vol. 49, no. 34, p. 345105, 2016.
181. N. Faramarzpour, M. Deen, S. Shirani and Q. Fang, "Fully Integrated Single Photon Avalanche Diode Detector in Standard CMOS 0.18- μ m Technology," *IEEE Transactions on electron devices*, vol. 55, no. 3, pp. 760-767, 2008.
182. M. El-Desouki, M. Jamal Deen, Q. Fang, L. Liu, F. Tse and D. Armstrong, "CMOS image sensors for high speed applications," *Sensors*, vol. 9, no. 1, pp. 430-444, 2009.
183. M. El-Desouki, O. Marinov, M. Deen and Q. Fang, "CMOS active-pixel sensor with in-situ memory for ultrahigh-speed imaging," *IEEE Sensors Journal*, vol. 11, no. 6, pp. 1375-1379, 2011.
184. "Picosecond Pulsed Sources - Fiber Coupling," PicoQuant, [Online]. Available: <https://www.picoquant.com/products/category/picosecond-pulsed-sources/ldh-series-picosecond-pulsed-diode-laser-heads#custom2>. [Accessed 17 04 2018].
185. A. CORPORATION, "Anritsu," [Online]. Available: <https://www.anritsu.com/en-us/test-measurement/support/downloads/manuals/dwl008621>. [Accessed 19 04 2018].
186. "Picosecond Pulsed Drivers - PDL 800-B," PicoQuant, [Online]. Available: <https://www.picoquant.com/products/category/picosecond-pulsed-driver/pdl-800-b-picosecond-pulsed-diode-laser-driver>. [Accessed 18 04 2018].
187. "WaveRunner 625Zi," Teledyne LeCroy, [Online]. Available: <http://teledynelecroy.com/oscilloscope/waverunner-6zi-oscilloscopes/waverunner-625zi>. [Accessed 18 04 2018].
188. A. Liemert and A. Kienle, "Exact and efficient solution of the radiative transport equation for the semi-infinite medium," *Scientific reports*, vol. 3, no. 1, p. 2018, 2013.

189. A. Pifferi, P. Taroni, G. Valentini and S. Andersson-Engels, "Real-time method for fitting time-resolved reflectance and transmittance measurements with a Monte Carlo model," *Applied optics*, vol. 37, no. 13, pp. 2774-2780, 1998.
190. "Newport Corporation," [Online]. Available: <https://www.newport.com/>. [Accessed 16 5 2018].
191. "1830-C Optical Power Meter - Instruction Manual," [Online]. Available: https://www.equipland.com/objects/catalog/product/extras/1030_1830-c.pdf. [Accessed 16 05 2018].
192. D. Milej, A. Gerega, M. Kacprzak, P. Sawosz, W. Weigl, R. Maniewski and A. Liebert, "Time-resolved multi-channel optical system for assessment of brain oxygenation and perfusion by monitoring of diffuse reflectance and fluorescence," *Opto-Electronics Review*, vol. 22, no. 1, pp. 55-67, 2014.
193. W. Cheong, S. Prahl and A. Welch, "A review of the optical properties of biological," *IEEE j. Quantum Electron*, vol. 26, no. 12, pp. 2166-2185, 1990.
194. L. Spinelli, M. Botwicz, N. Zolek, M. Kacprzak, D. Milej, P. Sawosz, A. Liebert, U. Weigel, T. Durduran, F. Foschum and A. Kienle, "Determination of reference values for optical properties of liquid phantoms based on Intralipid and India ink," *Biomedical optics express*, vol. 5, no. 7, pp. 2037-2053, 2014.
195. R. Re, D. Contini, M. Caffini, R. Cubeddu, L. Spinelli and A. Torricelli, "A compact time-resolved system for near infrared spectroscopy based on wavelength space multiplexing," *Review of Scientific Instruments*, vol. 81, no. 11, p. 113101, 2010.
196. A. Pifferi, A. Torricelli, L. Spinelli, D. Contini, R. Cubeddu, F. Martelli, G. Zaccanti, A. Tosi, A. Dalla Mora, F. Zappa and S. Cova, "Time-resolved diffuse reflectance using small source-detector separation and fast single-photon gating," *Physical review letters*, vol. 100, no. 13, p. 138101, 2008.
197. A. Puszka, L. Di Sieno, A. Dalla Mora, A. Pifferi, D. Contini, G. Boso, A. Tosi, L. Hervé, A. Planat-Chrétien, A. Koenig and J. Dinten, "Time-resolved diffuse optical tomography using fast-gated single-photon avalanche diodes," *Biomedical optics express*, vol. 4, no. 8, pp. 1351-1365, 2013.
198. "4156C Precision Semiconductor Parameter Analyzer," Keysight, [Online]. Available: <https://www.keysight.com/en/pd-153517-pn-4156C/precision-semiconductor-parameter-analyzer?&cc=CA&lc=eng>. [Accessed 14 09 2018].
199. "DATA DELAY DEVICES, INC," [Online]. Available: <http://www.datadelay.com/datasheets/3d9950.pdf>. [Accessed 14 09 2018].